NASA
Technical
Paper
2580

April 1986

Aerodynamic Characteristics of a Supersonic Fighter Aircraft Model at Mach 0.40 to 2.47

Francis J. Capone,
E. Ann Bare,
and Dorothy Arbiter

NASA

NASA Technical Paper 2580

1986

Aerodynamic Characteristics of a Supersonic Fighter Aircraft Model at Mach 0.40 to 2.47

Francis J. Capone
and E. Ann Bare
Langley Research Center
Hampton, Virginia

Dorothy Arbiter
The George Washington University
Joint Institute for Advancement of Flight Sciences
Langley Research Center
Hampton, Virginia

National Aeronautics
and Space Administration

Scientific and Technical Information Branch

SUMMARY

The aerodynamic characteristics of an advanced twin-engine fighter aircraft designed for supersonic cruise have been studied in the Langley 16-Foot Transonic Tunnel and the Lewis 10- by 10-Foot Supersonic Tunnel. The objective of this investigation was to establish an aerodynamic data base for the configuration with flow-through nacelles and representative inlets. The use of a canard for trim and the effects of fairing over the inlets were assessed. Comparisons between experimental and theoretical results were also made. The theoretical results were determined by using a potential plus vortex lift code for subsonic speeds and a linear aerodynamic code for supersonic speeds. This investigation was conducted at Mach numbers from 0.40 to 2.47, at angles of attack of 0° to about 20°, and at inlet capture ratios of about 0.5 to 1.4.

Wing-body-canard aerodynamics were typical for configurations having close-coupled canards. Canard angles between -5° and 0° were found to be near optimum for minimum trim drag. Addition of the podded engine nacelles doubled zero-lift pitching moment at all Mach numbers. A 13- to 16-percent decrease in trimmed maximum lift-drag ratio was found for the configuration at subsonic speeds because canard angles of about -12° were required to trim the large positive zero-lift pitching moment of the configuration. At supersonic speeds, small reductions of 0.5 to 4 percent in trimmed maximum lift-drag ratio occurred because canard angles of 0.8° to 5.7° were required to trim the configuration. Excellent agreement between experimental and theoretical lift was found for the wing-body-canard configuration at subsonic speeds and for the wing-body configuration at supersonic speeds.

INTRODUCTION

The mission requirements for the next generation of fighter aircraft may dictate a highly versatile vehicle capable of operating over a wide range of flight conditions. This range of conditions may include efficient supersonic cruise, at least current levels of maneuverability, and short take-off and landing characteristics required to operate from bomb-damaged airfields. These multimission capabilities require the designer to employ emerging technological concepts such as multifunction nozzles with thrust vectoring and reversing, close-coupled canards, relaxed static stability, active controls, and vortex control.

The impacts of some of these technological concepts on aircraft design have been investigated in a cooperative effort between the NASA Langley Research Center and the Boeing Military Airplane Company. This extensive program focused on an advanced tactical fighter designed for supersonic cruise (ref. 1). This aircraft was a Mach 2.0, 49,000-pound vehicle with a close-coupled canard and underwing propulsion units that utilized multifunction two-dimensional exhaust nozzles. As part of this program, a wind-tunnel model was constructed and tested to determine the various interactive effects of aerodynamic and propulsive forces for a highly integrated aircraft.

An objective of the overall program (see ref. 1) was to establish an aerodynamic data base for the fighter configuration with flow-through nacelles and representative inlets. Previous high-speed investigations of this model in the powered mode (operating jet exhausts) were conducted with the inlets faired over and were reported in

references 2, 3, and 4. In addition, low-speed aerodynamic characteristics of the model in the powered mode were reported in references 5 and 6. Experimental flow-field studies were conducted in reference 7, and these results were used to verify various analytical flow-field codes.

This report presents the aerodynamic characteristics of this tactical fighter model with flow-through nacelles at Mach numbers from 0.40 to 2.47, at angles of attack from 0° to about 20°, and at inlet capture ratios of about 0.5 to 1.4. These investigations were conducted in the Langley 16-Foot Transonic Tunnel and the Lewis 10- by 10-Foot Supersonic Tunnel. Mass flow through the nacelles was varied by using combinations of inlet spikes and exit inserts based upon the test Mach number. The use of a canard for trim and the effects of fairing over the inlets for the powered-mode tests were assessed. Comparisons between experimental and theoretical results were also made. The theoretical results were determined by using a potential plus vortex lift code for subsonic speeds and a linear aerodynamic code for supersonic speeds.

SYMBOLS

Model forces and moments are referred to the stability-axis system with the moment reference center located at FS 68.83 in., which corresponds to $0.28\bar{c}$.

A_c inlet capture area, in^2

A_e nozzle exit area, in^2

A_∞ cross-sectional area of stream tube at free-stream conditions, in^2

A_∞/A_c inlet capture ratio (mass flow ratio)

C_D drag coefficient, $\text{Drag}/q_\infty S$

$C_{D,i}$ internal drag coefficient

$C_{D,o}$ C_D at $C_L = 0$

C_L lift coefficient, $\text{Lift}/q_\infty S$

C_{L_α} lift-curve slope, per degree

C_m pitching-moment coefficient, $\text{Pitching moment}/q_\infty S\bar{c}$

$C_{m,o}$ C_m at $C_L = 0$

$C_{m_{C_L}}$ longitudinal stability parameter, dC_m/dC_L

$\bar{c}$ wing mean geometric chord, in.

d_e height at nozzle exit, in.

L/D lift-drag ratio

M free-stream Mach number

M_e nozzle exit Mach number

M_{in} local inlet Mach number

M(L/D) range parameter

NPR nozzle pressure ratio, $p_{t,j}/p_\infty$

$p_{t,e}$ average exit total pressure, psi

$p_{t,j}$ average jet total pressure, psi

$p_{t,\infty}$ free-stream total pressure, psi

p_∞ free-stream static pressure, psi

q_∞ free-stream dynamic pressure, psi

S wing reference area, 936.68 in^2

α angle of attack, deg

Δ increment

δ_c canard incidence angle, positive for leading edge up, deg

θ_1, θ_2 inlet spike initial ramp and secondary ramp angles, respectively, deg

Subscripts:

c canard

camber camber drag

max maximum

p potential

prof profile

trim trimmed

vle vortex effect at leading edge

vse vortex effect at side edge

w wing

wave wave drag

Abbreviations:

DWS downwash shift, in.

FS fuselage station, in.

WB wing-body

WBC wing-body-canard

WBCN wing-body-canard-nacelle

WBL wing butt line, in.

WL water line, in.

16 FTT Langley 16-Foot Transonic Tunnel

10 × 10 T Lewis 10- by 10-Foot Supersonic Tunnel

MODEL

This investigation was conducted with a 10.5-percent scale model of a twin-engine fighter aircraft designed to cruise at supersonic speeds. A sketch showing the general arrangement of the model and support system is presented in figure 1. Photographs of the model are shown in figure 2. The model featured a high-performance cambered and twisted wing and canard and had two single-engine podded nacelles mounted under the wing.

Wing-Canard-Fuselage Design

The configuration was designed for self-trimming at a cruise speed of Mach 2 and a design lift coefficient of 0.10. The trim condition for the vehicle was established from the criterion that the vehicle be 5 percent unstable subsonically, which resulted in the vehicle being 4 percent stable for the supersonic design case.

The aerodynamic design of the lifting surfaces was accomplished by the use of the FLEXSTAB code (ref. 8). This code uses the aerodynamic influence coefficient method and includes the effects of nonplanar surfaces such as a canard above the wing plane. The method is based on a linearized potential-flow theory with constant-pressure panels. The twist and the camber of both the canard and the wing surfaces are determined simultaneously such that the induced drag is minimized. Figure 3 illustrates the modeling of the vehicle for the FLEXSTAB code and the resulting wing and canard design.

The planform geometry of the wing is shown in figure 4. The wing had a leading-edge sweep of 68°, an aspect ratio of 1.53, a reference area of 936.68 in^2, and a wing mean geometric chord of 31.68 in. The planform geometry of the canard is shown in figure 5. The canard incidence angle was remotely controlled about the canard hinge axis located at FS 46.18 in. The canard also had a dihedral of 10° (fig. 5).

Conventional supersonic aerodynamic area-ruling design techniques were used to establish the fuselage cross-sectional area distribution. A complete description of the model wing and body geometry is given in reference 7.

Nacelle Design

The flow-through nacelles are shown in figure 6. Installation details are found in figure 6(a). The nacelle had a representative inlet and an aerodynamic reference nozzle. The model simulated an external compression, half-axisymmetric inlet with a semiconical spike (centerbody). Four interchangeable inlet spikes were provided to vary mass flow through the inlet (fig. 6(b)). One inlet spike with a half angle of 12° was used at $M \leq 1.20$. The other three spikes were tested at $M > 1.20$ and were designed for local inlet Mach numbers of 1.75, 2.00, and 2.20. The upper photograph of figure 6(c) shows the inlet with the spike designed for $M_{in} = 2.00$. Because of the size of the model, only limited inlet performance such as first-order spillage effects can be determined for use in airplane performance predictions as described in reference 1.

The flow-through nacelle terminated with a low-aspect-ratio two-dimensional convergent aerodynamic reference nozzle. The exit of the nozzle was at approximately the same fuselage station as that of the two-dimensional convergent-divergent nozzle in the mid (baseline) position of reference 4. The nozzle boattail angles (fig. 6(b)) were kept as small as possible to minimize jet effects. The nozzle exit area was varied by use of nozzle inserts (fig. 6(b)). The exit with the insert having $A_e/A_c = 0.636$ is shown in the bottom photograph of figure 6(c). Exit rakes attached directly to one of the reference nozzles were used to determine inlet recovery, mass flow, and internal drag characteristics. These results are presented in appendix A.

APPARATUS AND PROCEDURE

Wind Tunnel and Support System

This investigation was conducted in the Langley 16-Foot Transonic Tunnel (16 FTT) and the Lewis 10- by 10-Foot Supersonic Tunnel (10 × 10 T). The 16 FTT is a single-return, atmospheric tunnel with a slotted, octagonal test section and continuous air exchange. The wind tunnel has a variable airspeed up to a Mach number of 1.30. A complete description of this facility and its operating characteristics can be found in reference 9.

The 10 × 10 T is a single-return, variable-pressure tunnel with a square test section. The contour of the nozzle sidewalls is remotely adjustable and can provide a Mach number range from 2.0 to 3.5. A description of this facility can be found in reference 10.

The model was supported in both wind tunnels by the same sting-strut (fig. 1) support system in which the strut replaced the vertical tail. The strut had an NACA 0006 airfoil section with a sweep of 60° and a maximum thickness of 1.75 in.

Instrumentation and Data Reduction

External aerodynamic forces and moments on the entire model were measured by a six-component force balance which was attached directly to the bottom of the strut (simulated vertical tail). A gap between the metric model body and nonmetric support strut prevented grounding of the force balance. It should be noted that the flexible air lines (air line and bellows) used for propulsion testing of this model were in

place for this investigation. (See ref. 4 for details.) Nacelle internal flow characteristics were determined from static- and total-pressure measurements with four rakes located at the nozzle exit as shown in figure 7. These external rakes were rigidly attached to the right nacelle when the measurements were made (fig. 7(b)). The position of the lower right rake varied as the nozzle insert varied; two typical rake positions are shown in figure 7(b). Pressures were also measured at the nozzle exit base, at the insert base, and in the model cavity. Electronically scanning pressure modules located in the model nose were used to measure all pressures in both facilities.

For each data point, multiple frames of data were averaged in each facility. Average values of the recorded data were used to compute standard force and moment coefficients based on wing area and mean geometric chord for reference area and length, respectively. A complete description of the data reduction procedures for the 16 FTT is found in reference 11. Engineering units data were transmitted by telephone from the Lewis to the Langley computer complex. Final reduction of the Lewis data was accomplished at Langley with the Langley code (ref. 11).

Axial force was adjusted to the condition of free-stream pressure acting in the model cavity and at the nozzle exit base and insert base. The axial-force pressure-area correction for the model cavity is usually equal to zero because of the type of support system used. In addition, nacelle duct internal drag and lift have been subtracted from the measured balance forces. Internal drag and duct flow parameters are presented in appendix A. No corrections were made to pitching moment.

The adjusted forces and moments measured by the balance were transformed from the body-axis system (WL 11.53 in.) to the stability-axis system. Angle of attack α was obtained by applying deflection terms, caused by model support and balance bending under aerodynamic loads, and a flow angularity term to the angle of the model support system. A flow angularity adjustment of 0.1°, which is the average tunnel upflow angle measured in the Langley 16-Foot Transonic Tunnel, was applied. No flow angularity adjustments were made to the data from the Lewis 10- by 10-Foot Supersonic Tunnel.

TESTS

Data were obtained in the 16 FTT at Mach numbers from 0.40 to 1.20 at angles of attack from 0° to about 19.5°. Reynolds number per foot varied from 3.0×10^6 to 4.1×10^6. Data were obtained in the 10 × 10 T at Mach numbers from 2.00 to 2.47 at angles of attack from 0° to about 19°. Reynolds number per foot varied from 1.4×10^6 to 1.8×10^6. Combinations of inlet spikes and nozzle inserts were used to vary mass flow through the nacelles. A separate series of runs was made to determine internal flow parameters because the exit rakes were rigidly attached to the model and invalidated the force and moment data. Canard incidence was varied from -15° to 15° for the wing-body-canard configuration to determine trim characteristics; canard incidence was held at 0° for all other configurations. The effect of fairing over the inlets was determined, and the results are presented in appendix B.

All tests were conducted with 0.10-in-wide boundary-layer transition strips consisting of silicon carbide grit sparsely distributed in a thin film of lacquer. These strips were located 2.00 in. from the tip of the forebody nose and nacelle and on both the upper and lower surfaces of the wings and canard at 0.20 in. normal to the leading edges. Number 100 and number 60 silicon carbide grit were used in the 16 FTT and the 10 × 10 T, respectively.

RESULTS AND DISCUSSION

Basic Aerodynamics

Wing-body-canard.- Basic wing-body-canard (nacelles off) longitudinal aerodynamic characteristics at $M = 0.40$ to 2.47 are presented in figure 8. The results at $M = 0.40$ to 1.20 were previously published in reference 4 and are included for completeness. At angles of attack up to about 4°, addition of the canard at $\delta_c = 0°$ had only a small effect on lift at most Mach numbers. This effect indicates, as do earlier studies, that the additional lift associated with a close-coupled canard mounted on or above the wing plane is counteracted by a comparable loss in wing lift due to the canard downwash flow field. At angles of attack above 4°, the model with the canard on produced more lift at all Mach numbers. At subsonic speeds, the lift curve remained nearly linear with increasing angle of attack at $\alpha > 7°$.

The effect of canard deflection on drag coefficient (shown in fig. 8) is also typical for close-coupled canard configurations and indicates that trimming this vehicle at canard deflections between -5° and 0° will result in minimum trim drag. At lift coefficients greater than 0.35 at $M = 0.60$, the configuration with canard deflections between -10° and 0° had less drag than the configuration without the canard.

Complete configuration.- The basic longitudinal aerodynamic characteristics for the complete configuration WBCN at $M = 0.60$ to 2.47 are presented in figures 9 to 12. These data are for the various combinations of inlet spikes and nozzle exit inserts tested at each Mach number and thus illustrate the effect of varying inlet capture ratio (mass flow). The correlation between A_e/A_c and A_∞/A_c is found in appendix A. As can be seen, there is no effect on lift coefficient from varying capture ratio. Up to $M = 1.2$, there was a small decrease in $C_{m,o}$ as capture ratio was increased.

As expected, there was generally a decrease in drag coefficient at all Mach numbers as capture ratio was increased as a result of the decrease in inlet spillage drag. (For example, see fig. 9(b) or fig. 11(c).) The results of figures 9 to 12 have been summarized in figure 13, where the effect of capture ratio variation on drag coefficient at $C_L = 0$ is shown. By extrapolating $C_{D,o}$ (fig. 13) and similarly drag coefficients at other constant lift coefficients (not shown) to $A_\infty/A_c = 1.0$, one can obtain drag polars with no spillage drag. For the remainder of this paper, aerodynamic coefficients will be presented at $A_\infty/A_c = 1.0$. No adjustments were made to either lift or pitching-moment coefficient because there was essentially no effect of varying capture ratio on these coefficients.

There are several reasons for presenting the aerodynamic characteristics of the configuration at $A_\infty/A_c = 1.0$. First, as shown in appendix A, there is a large variation of capture ratio with angle of attack at $M \geq 2.00$. Therefore, analyses at constant lift coefficient are difficult to make because of the large variation in spillage drag over the angle-of-attack range (when data are not corrected to $A_\infty/A_c = 1.0$). Second, analytic results to be presented were determined for $A_\infty/A_c = 1.0$. In addition, the inlet spillage drag is usually treated as part of the net propulsive force when determining overall performance (ref. 1) because engine airflow requirements vary over the flight envelope.

Lift-Curve Slope

The variation of lift-curve slope with Mach number is presented in figure 14 for the WB, WBC, and WBCN configurations. Addition of the canards only increased C_{L_α} 6 to 8 percent at Mach numbers from 0.60 to 1.20 and about 11 percent at Mach numbers from 2.00 to 2.47. As mentioned previously, addition of the canard at $\delta_c = 0°$ had only a small effect on lift, since the canards increased the planform area by 13 percent. Addition of the nacelles reduced lift-curve slope up to $M = 1.20$ and had a small effect at Mach numbers from 2.00 to 2.47. The results presented in figure 14 are typical for configurations with this type of wing planform.

Stability Characteristics

The longitudinal stability characteristics for the WB, WBC, and WBCN configurations are presented in figure 15. The longitudinal stability parameter $C_{m_{C_L}}$ for the WB configuration exhibits the expected trend with Mach number, as it becomes more negative (stable) up to $M = 1.20$ as a result of the rearward shift of the center of pressure. Addition of the canards was destabilizing. The wing-body-canard configuration is about 1 percent unstable at $M = 0.60$ and 6 to 7.5 percent stable at $M > 2.00$. The design goal was a vehicle 5 percent unstable at subsonic speeds and 4 percent stable at supersonic speeds. Addition of the nacelles had only a small effect on stability.

Zero-lift pitching-moment coefficient $C_{m,o}$ is also presented in figure 15. As can be seen, both the WB and WBC configurations have positive values of $C_{m,o}$ (except at $M = 2.47$). Addition of the nacelles more than doubled $C_{m,o}$ over the entire Mach number range. This large positive increase in $C_{m,o}$ may be characteristic for vehicles with podded nacelles because a similar increase in $C_{m,o}$ was obtained on the B-1 airplane (ref. 12). The effect of this large positive value of $C_{m,o}$ on trimming the configuration is addressed in a later section.

Drag and Trim Characteristics

Zero-lift drag.- The zero-lift drag characteristics for the WB, WBC, and WBCN configurations are presented in figure 16. The drag coefficients for the WBCN configuration have been adjusted to an inlet capture ratio of 1.0. The effects on zero-lift drag coefficient of increasing Mach number or adding either the canards or nacelle show the expected trends except at $M \geq 2.00$, where the addition of the canard to the wing-body reduced $C_{D,o}$. This result may be caused by some beneficial interference of canard downwash on the wing rather than a reduction in wave drag, since the analytical methods did not predict these trends.

Trim characteristics.- The ability of a supercruiser to perform its mission is very dependent upon the aircraft maintaining high levels of aerodynamic efficiency at supersonic speeds. Historically, fighters have been primarily subsonic/transonic designs with supersonic dash capability. Generally, these vehicles have also been statically stable at subsonic speeds. As a result, static margins as high as 30 percent can occur at supersonic speeds and can result in trim drag penalties of up to 35 percent of the total drag.

As previously mentioned, the drag data of figures 9 to 12 were adjusted to the condition of $A_\infty/A_c = 1.0$ at the inlets. These adjusted polars, both untrimmed and

trimmed, are shown in figure 17. The wing-body-canard data of figure 8 were used to trim the configuration by using only the canard. For the powered case, thrust vectoring could also be used for trim (refs. 1 and 3).

The aerodynamic efficiency of the current supercruiser configuration in terms of maximum lift-drag ratio as a function of Mach number is presented in figure 18. Untrimmed $(L/D)_{max}$ values for the WB, WBC, and WBCN configurations are presented for reference. Note that the canard is at 0° (untrimmed), the inlet is operating at $A_\infty/A_c = 1.0$, and ram nozzle pressure ratio exists at the exit of the reference nozzle. The ram NPR is caused by flow through the nacelle and is a function of the average total pressure at the exit divided by the free-stream static pressure. Addition of the nacelles reduced untrimmed $(L/D)_{max}$ 25 to 33 percent over the Mach number range.

Trimmed maximum lift-drag ratio and the range parameter $M(L/D)_{max}$ for the WBCN configuration are also shown in figure 18. There were 16.5- and 12.8-percent decreases in $(L/D)_{max}$ due to trimming the configuration at $M = 0.60$ and 0.87, respectively. At supersonic speeds, the percent reductions varied from 0.5 at $M = 2.00$ to 4 at $M = 2.47$. The percent reductions in $(L/D)_{max}$ are relative to the untrimmed $(L/D)_{max}$ value for the WBCN configuration. It is obvious from these data that trim drag penalties are much more severe at subsonic speeds than at supersonic speeds for this vehicle. The reason for the high subsonic trim drag penalties is associated with the zero-lift pitching-moment characteristics (fig. 15). Ideally, canard angles of -5° to 0° are desirable to trim the configuration from a minimum drag standpoint (fig. 8). However, because of the high positive subsonic $C_{m,o}$ (0.05 to 0.07), large nose-down moments are required from the canard, and canard angles of about -12° are required to trim at $(L/D)_{max}$. Canard angles of this magnitude result in large trim drag penalties. (See fig. 19.) There is also a 40- to 50-percent increase in C_L for $(L/D)_{max}$ from trimming the configuration (not shown).

At supersonic speeds ($M \geq 2.0$), however, canard angles required for trim at $(L/D)_{max}$ varied from 0.8° at $M = 2.00$ to 5.7° at $M = 2.47$. As a result, trim drag is very small, and consequently the reductions in $(L/D)_{max}$ are also very small. These results indicate that the design goal of a self-trimming vehicle at $M = 2.00$ was nearly achieved. At $M = 1.20$, the canard angle required for trim at $(L/D)_{max}$ is about -8.5°. However, trimmed $(L/D)_{max}$ at $M = 1.20$ occurs at $C_L = 0.28$ ($\alpha \approx 8.3°$), and at these angles of attack, canard angles between -10° and -5° are more nearly optimum for minimum trim drag. Thus, the trim drag penalty at $M = 1.20$ is also small. A discussion of the effects of power and thrust vectoring on trimmed $(L/D)_{max}$ is found in references 1 and 4.

Aerodynamic Predictions

Component drag characteristics.- Comparisons between experimental and predicted zero-lift drag characteristics for the WB, WBC, and WBCN configurations are presented in figure 20. The predicted drag coefficient is composed of profile drag (skin friction adjusted by form factors) at subsonic speeds and profile, wave (ref. 13), and camber (ref. 14) drag at supersonic speeds. Wave drag was computed by a far field procedure in which the actual geometry of the vehicle is used.

The differences between measured and predicted zero-lift drag are probably caused by wing-body camber effects (not considered in prediction) at subsonic speeds and nacelle interference at supersonic speeds. At $M = 2.00$, the measured increment

in drag coefficient from adding the nacelle was 64 percent larger than the predicted value. For this reason, a significant interference effect from the nacelles is probably indicated.

Subsonic lift and drag predictions.- A comparison of experimental and theoretical lift at $M = 0.60$ and 0.87 at $\delta_c = 0°$ is presented in figure 21. The lift curve for the potential-flow case ($C_{L,p,w} + C_{L,p,c}$) was predicted by the method of reference 15 and for the vortex lift case by the method of reference 16. Only potential lift for the canard was used because no characteristic length used in the calculation of the canard vortex lift was determined (ref. 16). As shown in figure 21, the agreement between lift determined by theory (potential plus vortex) and experiment is excellent at both $M = 0.60$ and 0.87.

The experimental drag data are also compared with drag estimates for both zero and full leading-edge suction in figure 21. Since the wing for this configuration was designed for supersonic speeds, it has a small leading-edge radius, and the experimental drag should compare with the curve for zero leading-edge suction. However, as shown, the agreement between theory and experiment is not good, probably because wing camber effects produced some distributed suction, which tends to reduce the drag.

Supersonic aerodynamic predictions.- The supersonic aerodynamic characteristics of the WB, WBC, and WBCN configurations were predicted by the method of reference 14. Canard angle was varied for the WBC configuration and fixed at 0° for the WBCN configuration.

This method uses an integrated system of computer programs that has been developed for the design and analysis of supersonic configurations. The system uses linearized theory methods for the calculation of surface pressures and supersonic area-ruling concepts in combination with linearized theory for calculation of aerodynamic force coefficients. The term DWS (see, for example, fig. 22) is a downwash shift feature of the theoretical program. The basic solution assumes the downwash from the canard propagates directly aft. Since the downwash in the real flow case will follow the fuselage contour, the shift feature in the program translates the downwash field laterally to account for changes in the radius of the fuselage between the generating canard and the affected wing lifting surface. In addition, solutions can be obtained in which the downwash can be shifted laterally a specified amount. Solutions were obtained with the downwash following the fuselage contour and at values of the downwash shift DWS of 2 and 3. The latter two conditions were calculated to determine the effect of these specified shifts on the predicted aerodynamic characteristics.

A comparison between experimental and theoretical lift characteristics for the WB, WBC, and WBCN configurations is presented in figure 22. Excellent agreement (depending on the DWS) was found for all the configurations shown at $M = 2.00$ and 2.17. At $M = 1.20$, excellent agreement between the experimental and predicted lift for the WB configuration was found up to $\alpha \approx 6°$. Lift predictions at $M = 1.20$ were poor with the addition of the canard. As can be seen from the experimental data, there is still a significant lift increment being generated on the wing because of favorable interference between the wing and the canard at this Mach number. This interference lift is not predicted by the linear method used. At $M = 2.47$, lift predictions are fair, depending on the canard angle. Adding the nacelles did not change the correlations.

The experimental and predicted pitching-moment characteristics for the WB, WBC, and WBCN configurations are compared in figure 23. As can be seen, good agreement

was found for the WB configuration at all Mach numbers. However, poor agreement was found between the experimental and predicted pitching-moment characteristics with the addition of the canard. The analytic values of $C_{m_{C_L}}$ and $C_{m,o}$ (canard effectiveness) were overpredicted.

A comparison between the experimental and theoretical drag-due-to-lift characteristics for the WB, WBC, and WBCN configurations is shown in figure 24. At $M = 2.00$ and 2.17, good to excellent agreement was generally found up to about $C_L = 0.30$. Drag-due-to-lift was overpredicted at $M = 1.20$ and underpredicted at $M = 2.47$. The increment in drag coefficient due to canard deflection at $C_L = 0$ can also be predicted by the method of reference 14, and this result is compared with the experimental increment in figure 25. This comparison indicates that $\Delta C_{D,o}$ was overpredicted for $\delta_c > 0°$ and generally underpredicted for $\delta_c < 0°$. It should be noted that although minimum $C_{D,o}$ was measured at $\delta_c = 0°$, this canard angle may not be optimum to trim at $(L/D)_{max}$.

CONCLUSIONS

The aerodynamic characteristics of an advanced tactical fighter designed for supersonic cruise are summarized over a Mach number range from 0.40 to 2.47. These results, from investigations conducted in the Langley 16-Foot Transonic Tunnel and the Lewis 10- by 10-Foot Supersonic Tunnel, indicate the following:

1. Wing-body-canard aerodynamics were typical for configurations having close-coupled canards. Canard angles between -5° and 0° were found to be near optimum for minimum trim drag.

2. Addition of the podded engine nacelles doubled zero-lift pitching moment at all Mach numbers.

3. A 13- to 16-percent decrease in trimmed maximum lift-drag ratio was found for the unpowered configuration at subsonic speeds. This decrease was caused by large canard angles of about -12° which were required to trim the large positive zero-lift pitching moment (aggravated by nacelle installation) of the configuration.

4. At supersonic speeds, small reductions of 0.5 to 4 percent in trimmed maximum lift-drag ratio occurred as a result of trimming for the unpowered configuration.

5. Excellent agreement between experimental and theoretical lift was found for the wing-body-canard configuration at subsonic speeds and for the wing-body configuration at supersonic speeds.

NASA Langley Research Center
Hampton, VA 23665-5225
January 15, 1986

APPENDIX A

Nacelle Internal Flow Characteristics

This appendix presents the nacelle internal flow characteristics and the inlet spillage effects on the complete configuration. The spillage characteristics obtained from this investigation can be very helpful in establishing first-order inlet effects even though no attempt was made to minimize inlet installation drag by such things as varying inlet geometry. Various combinations of inlet centerbody spikes and nozzle exit inserts were used to vary mass flow through the inlet (fig. 6). These combinations have to be carefully selected to avoid an unstarted inlet or an inlet duct with supersonic flow conditions, which usually affect inlet performance for $M > 1.6$. In the 10 × 10 T, inlet flow conditions were constantly monitored by using a schlieren system to assure that the inlets did not reach an unstart condition.

Basic nacelle internal flow characteristics are presented in figures 26 to 29. Shown are the variations with angle of attack of inlet capture ratio A_∞/A_c, internal drag coefficient $C_{D,i}$, exit Mach number M_e, and inlet total-pressure recovery characteristics $p_{t,e}/p_{t,\infty}$. These parameters were computed from the static and total pressures measured at the nozzle exit. (See ref. 11.)

Typical inlet performance in terms of inlet capture ratio (mass flow ratio) and total-pressure recovery is summarized as a function of A_e/A_c, the ratio of the duct exit area to the inlet capture area, in figures 30 and 31, respectively. The increase in capture ratio or pressure recovery at $M = 2.00$ with increasing angle of attack is probably caused by some precompression of the inlet flow along the underside of the wing. The effect of varying inlet capture ratio on drag coefficient at $C_L = 0$ was presented in figure 13.

APPENDIX B

Effect of Faired Inlet

A major concern with testing of powered models has always been the effects of modifications to aircraft geometry that are unique to the wind-tunnel model. These include interference effects from such items as model support, metric breaks for partially metric models, and faired-over inlets. For the present study, only the effect of the faired inlets need be evaluated, since the entire model was metric and interference from the support strut should be representative of the configuration vertical tail.

The effect of faired inlets was determined from data obtained on the configuration with the flow-through nacelles (fig. 6) and with powered nacelles with faired inlets (fig. 32). For both configurations, the nacelles were attached to the wing in the same locations. The same reference nozzle was then tested with each of these nacelles. Except for the inlet fairing, the external lines of these nacelles were the same. Thus, a common set of nacelle/nozzle geometry was provided for aeropropulsion force and moment bookkeeping (ref. 1). Details of the test procedures used for the configuration with the powered nacelles can be found in reference 4.

The reference nozzles with $A_e/A_c = 0.636$ were used for both configurations. Since the flow-through nacelles will operate at some ram nozzle pressure ratios, it is desirable to obtain data with the powered nacelles at these same nozzle pressure ratios in order to have the same jet effects. A comparison between the ram (flow-through) and powered nozzle pressure ratios is presented in figure 33. The ram nozzle pressure ratios, indicated by the plotted data, show an effect of angle of attack at $M > 1.20$. The powered nozzle pressure ratio for each Mach number is indicated by the tick marks located on the left portion of the figure. The powered NPR is held constant as angle of attack is varied for the powered case. No corrections due to jet effects are made to account for the small differences between the ram and powered nozzle pressure ratios that exist over the angle-of-attack range at supersonic speeds.

The effect of the faired inlets on the longitudinal aerodynamic characteristics is presented in figure 34. At $M \geq 2.00$, the flow-through nacelle with the inlet centerbody spike designed for $M_{in} = 2.00$ was chosen because it is a representative configuration of those tested at these Mach numbers. Ram nozzle pressure ratios at $M \geq 2.00$ are indicated by solid symbols in figure 33. Thrust-removed aerodynamic force and moment coefficients for the configuration with the faired inlet are presented. (See refs. 4 and 11 for procedures.) From these data, the incremental aerodynamic effect of the faired inlet can be determined, and this result is presented in figure 35.

For lift and pitching-moment data, the increment due to the faired-over inlet shown in figure 35 is simply the difference in coefficients for the powered and flow-through nacelles evaluated at constant angles of attack at the ram NPR for each particular Mach number. Comparisons of lift and pitching-moment coefficients obtained with the flow-through nacelles with different nozzle inserts showed no effect of inlet capture ratio on these parameters at either subsonic or supersonic speeds. However, since the drag of the configuration with the flow-through nacelles varies with inlet capture ratio, an additional correction should be made to adjust the drag coefficients to the condition of $A_\infty/A_c = 1.0$ at the inlets. This adjustment is

particularly necessary at $M \geq 2.00$ because of the large variation of capture ratio with angle of attack. (See, for example, fig. 27(a).)

The largest effect of the faired inlets was on drag coefficient; for example, ΔC_D at subsonic speeds was about 24 percent of the total drag for the configuration with the faired inlet. At supersonic speeds, this increment ranged from about 8 to 15 percent, depending upon Mach number.

The magnitudes of both incremental lift and pitching moment are considered to be small. As can be seen, ΔC_L is nearly constant at Mach numbers from 0.60 to 2.00 at $\alpha = 0°$. An assumed value of ΔC_m equal to 0.02 was subtracted from the untrimmed pitching-moment data of reference 4 to account for the faired-over inlet prior to trimming those data. It is obvious from the results of figure 35 that this estimate was too high.

REFERENCES

1. Capone, Francis J.; Bare, E. Ann; Hollenback, David; and Hutchison, Robert: Subsonic/Supersonic Aerodynamic Characteristics for a Tactical Supercruiser. AIAA-84-2192, Aug. 1984.

2. Capone, Francis J.; Reubush, David E.; Petit, John E.; and Hutchison, Robert A.: Nacelle/Nozzle Integration for Supersonic Fighter Aircraft. Tactical Aircraft Research and Technology - Volume I, NASA CP-2162, Part 2, 1981, pp. 655-694.

3. Capone, Francis J.; and Reubush, David E.: Effect of Thrust Vectoring and Wing Maneuver Devices on Transonic Aeropropulsive Characteristics of a Supersonic Fighter Aircraft. NASA TP-2119, 1983.

4. Capone, Francis J.; and Reubush, David E.: Effects of Varying Podded Nacelle-Nozzle Installations on Transonic Aeropropulsive Characteristics of a Supersonic Fighter Aircraft. NASA TP-2120, 1983.

5. Paulson, J. W., Jr.: An Analysis of Thrust-Induced Effects on the Longitudinal Aerodynamics of STOL Fighter Configurations. AIAA-80-1879, Aug. 1980.

6. Hutchison, R. A.; Sussman, Mark B.; Mainquist, R.; and Paulson, J. W., Jr.: STOL Wind Tunnel Test Results for a Tactical Supercruiser. AIAA-83-1224, June 1983.

7. Reubush, David E.; and Bare, E. Ann: Investigation of a Supersonic Cruise Fighter Model Flow Field. NASA TM-86361, 1985.

8. Tinoco, E. N.; and Mercer, J. E.: FLEXSTAB - A Summary of the Functions and Capabilities of the NASA Flexible Airplane Analysis Computer System. NASA CR-2564, 1975.

9. Peddrew, Kathryn H., compiler: A User's Guide to the Langley 16-Foot Transonic Tunnel. NASA TM-83186, 1981.

10. Aiello, Robert A.: NASA Lewis 10- by 10-Foot Supersonic Wind Tunnel. NASA TM X-71625, 1974.

11. Mercer, Charles E.; Berrier, Bobby L.; Capone, Francis J.; Grayston, Alan M.; and Sherman, C. D.: Computations for the 16-Foot Transonic Tunnel - NASA Langley Research Center. NASA TM-86319, 1984.

12. Re, Richard J.; and Reubush, David E.: Effect of Several Airframe/Nozzle Modifications on the Drag of a Variable-Sweep Bomber Configuration. NASA TM-80129, 1979.

13. Craidon, Charlotte B.: User's Guide for a Computer Program for Calculating the Zero-Lift Wave Drag of Complex Aircraft Configurations. NASA TM-85670, 1983.

14. Middleton, W. D.; and Lundry, J. L.: A System for Aerodynamic Design and Analysis of Supersonic Aircraft. Part 1 - General Description and Theoretical Development. NASA CR-3351, 1980.

15. Lamar, John E.: A Modified Multhopp Approach for Predicting Lifting Pressures and Camber Shape for Composite Planforms in Subsonic Flow. Supplement to NASA TN D-4427, 1968.

16. Lamar, John E.: Some Recent Applications of the Suction Analogy to Vortex-Lift Estimates. Aerodynamic Analyses Requiring Advanced Computers, Part II, NASA SP-347, 1975, pp. 985-1011.

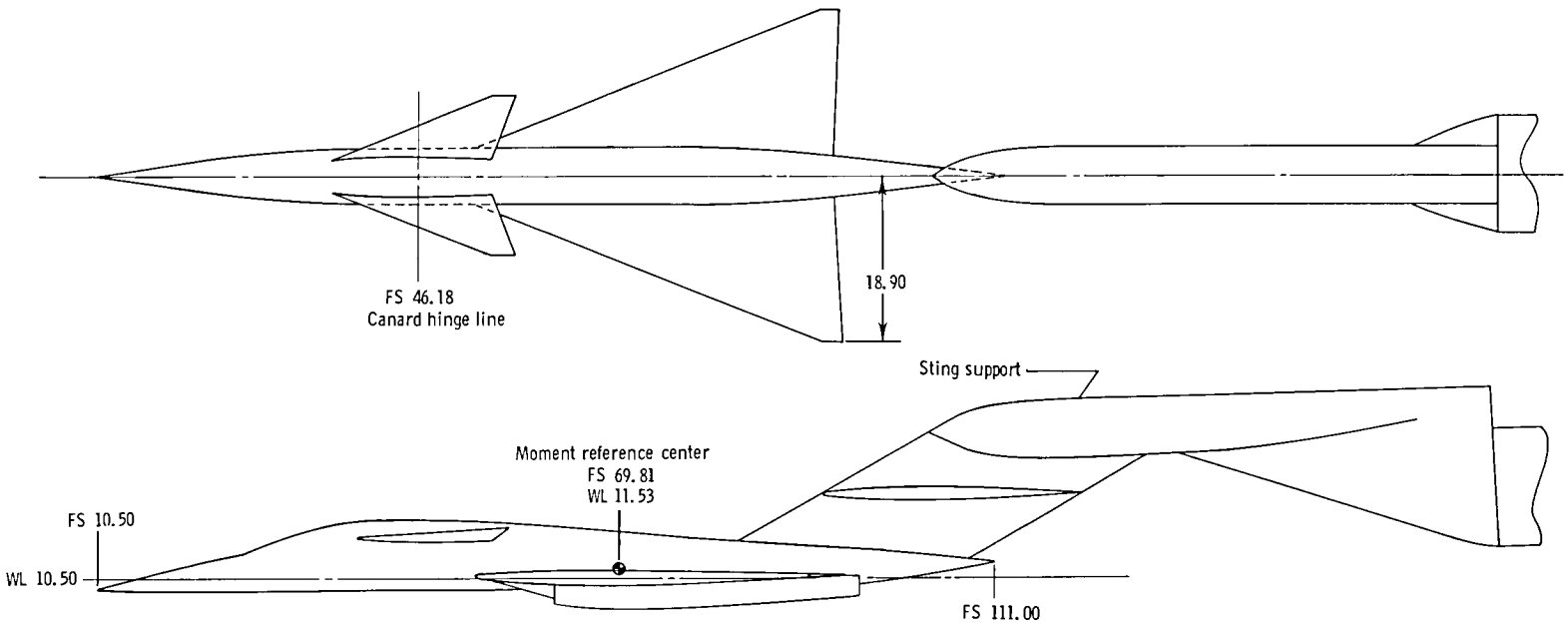

Figure 1.- Sketch showing general arrangement of model and support system. All linear dimensions in inches.

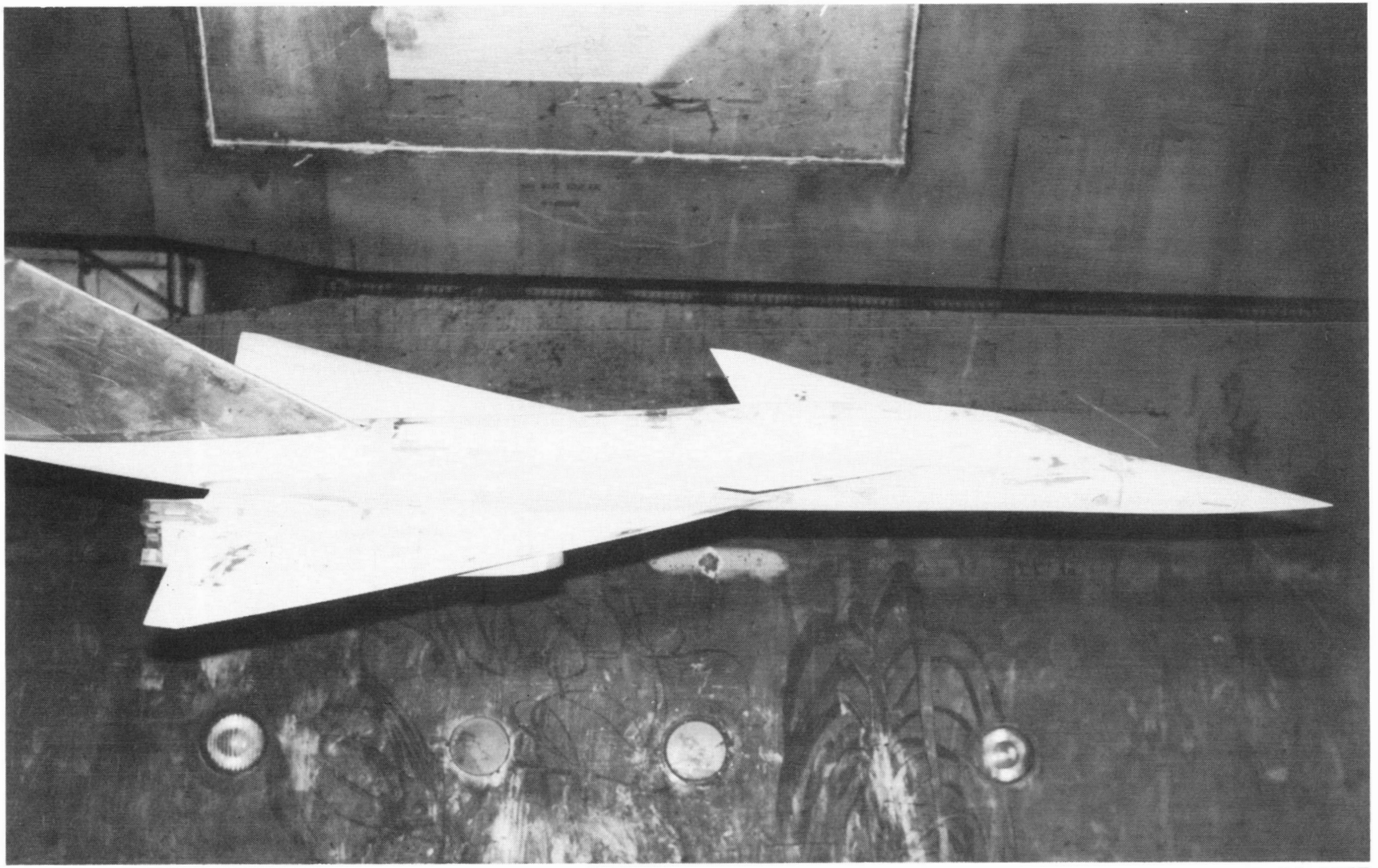

L-84-4657

(a) Model in Langley 16-Foot Transonic Tunnel.

Figure 2.- Photographs of model.

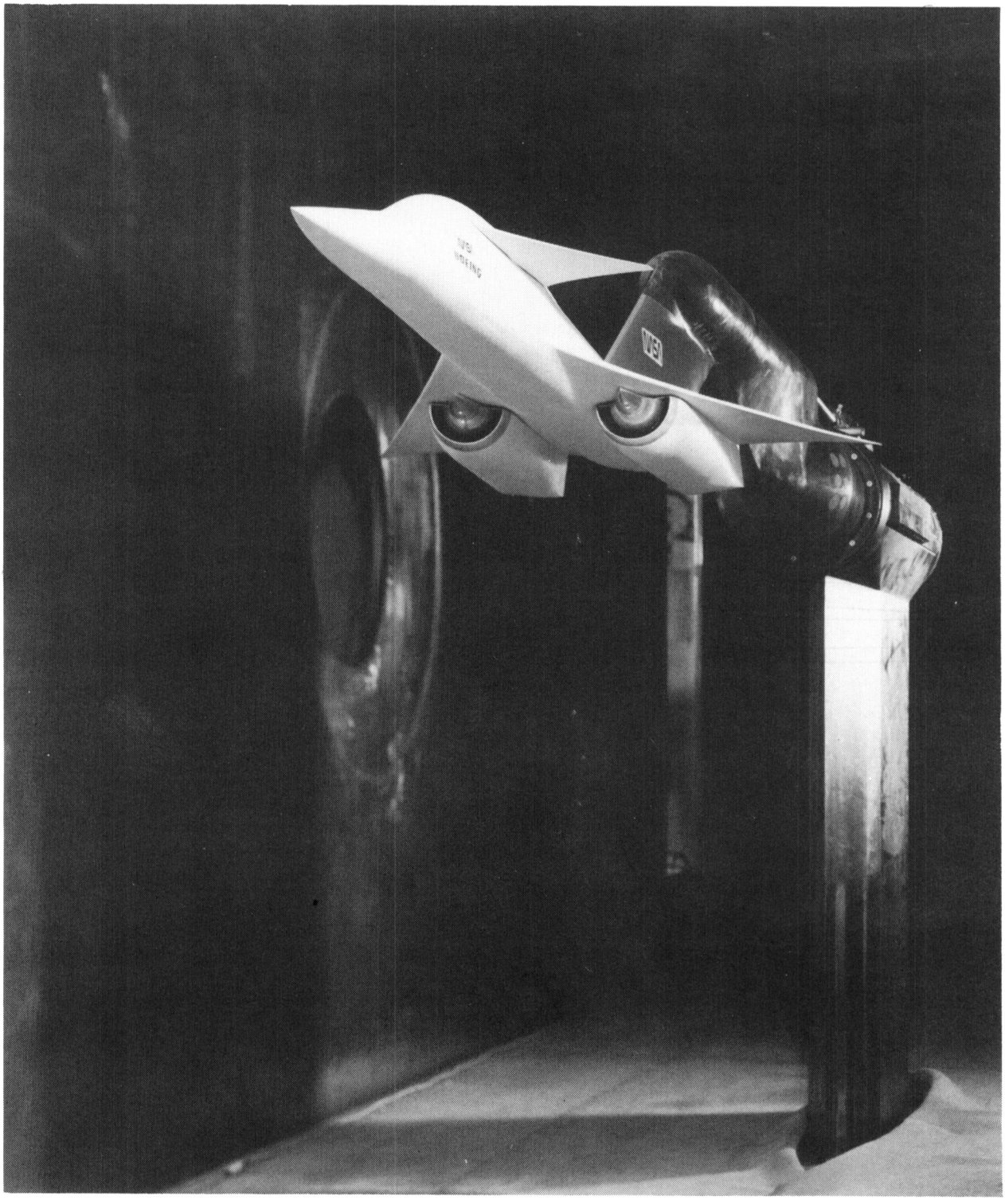

(b) Model in Lewis 10- by 10-Foot Supersonic Tunnel.

Figure 2.- Concluded.

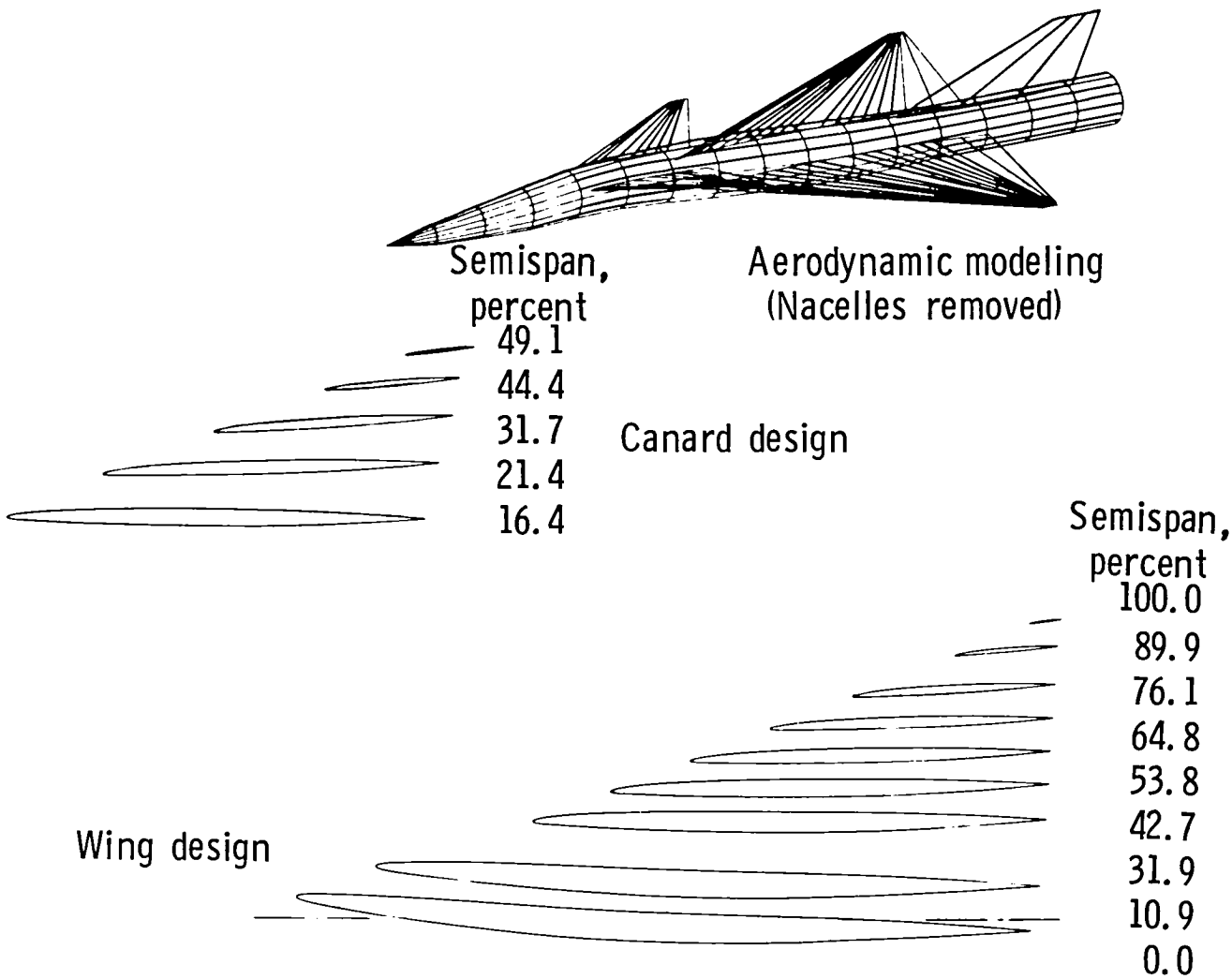

Figure 3.- Wing-canard design characteristics.

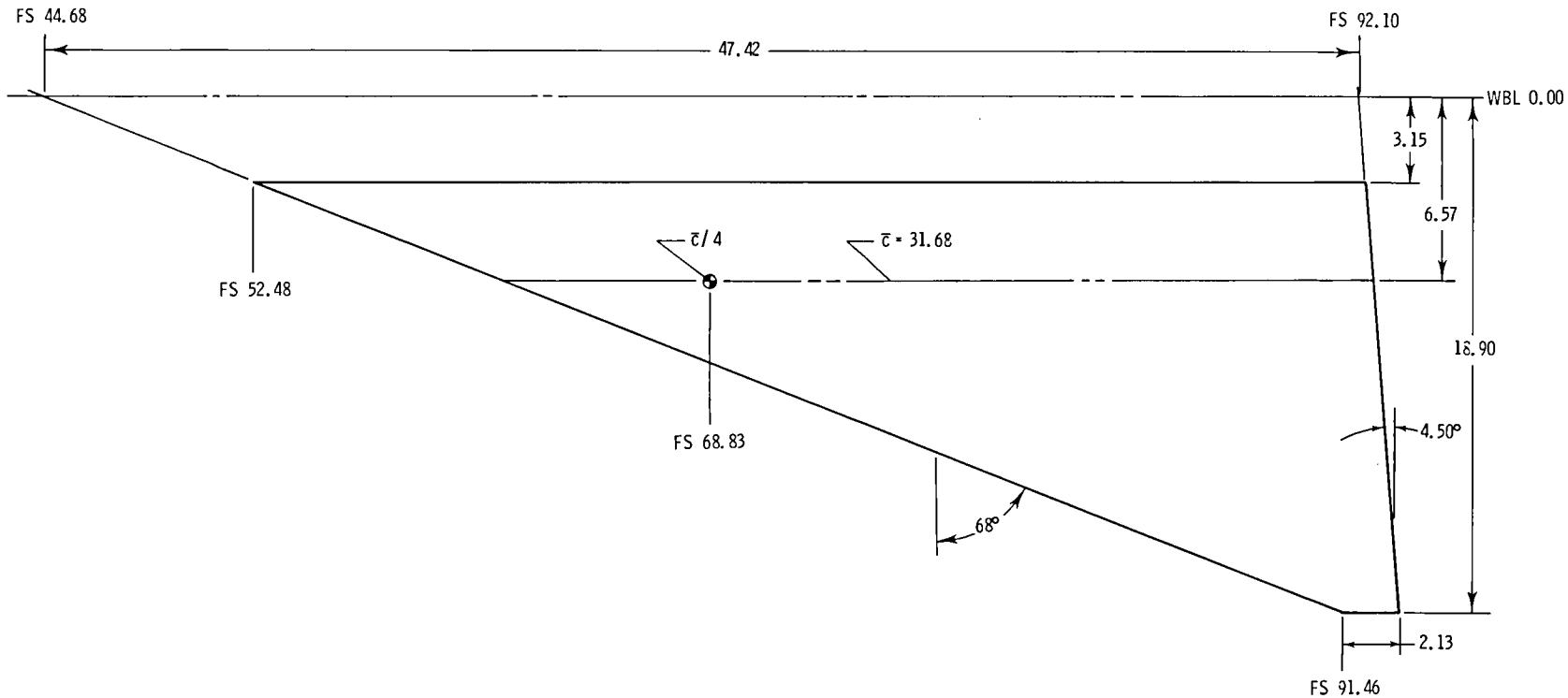

Figure 4.- Sketch showing planform geometry of wing. All linear dimensions in inches.

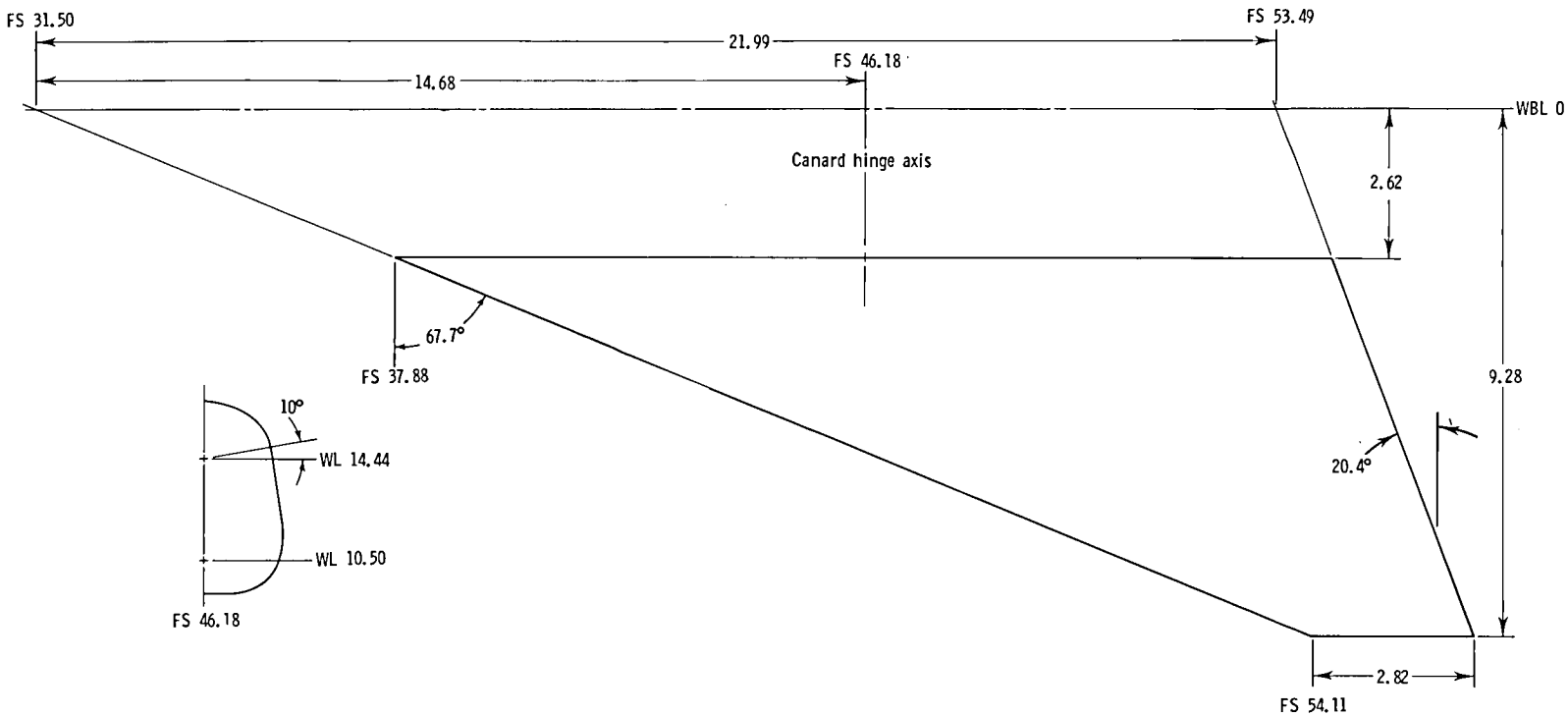

Figure 5.- Sketch showing planform geometry of canard. All linear dimensions in inches.

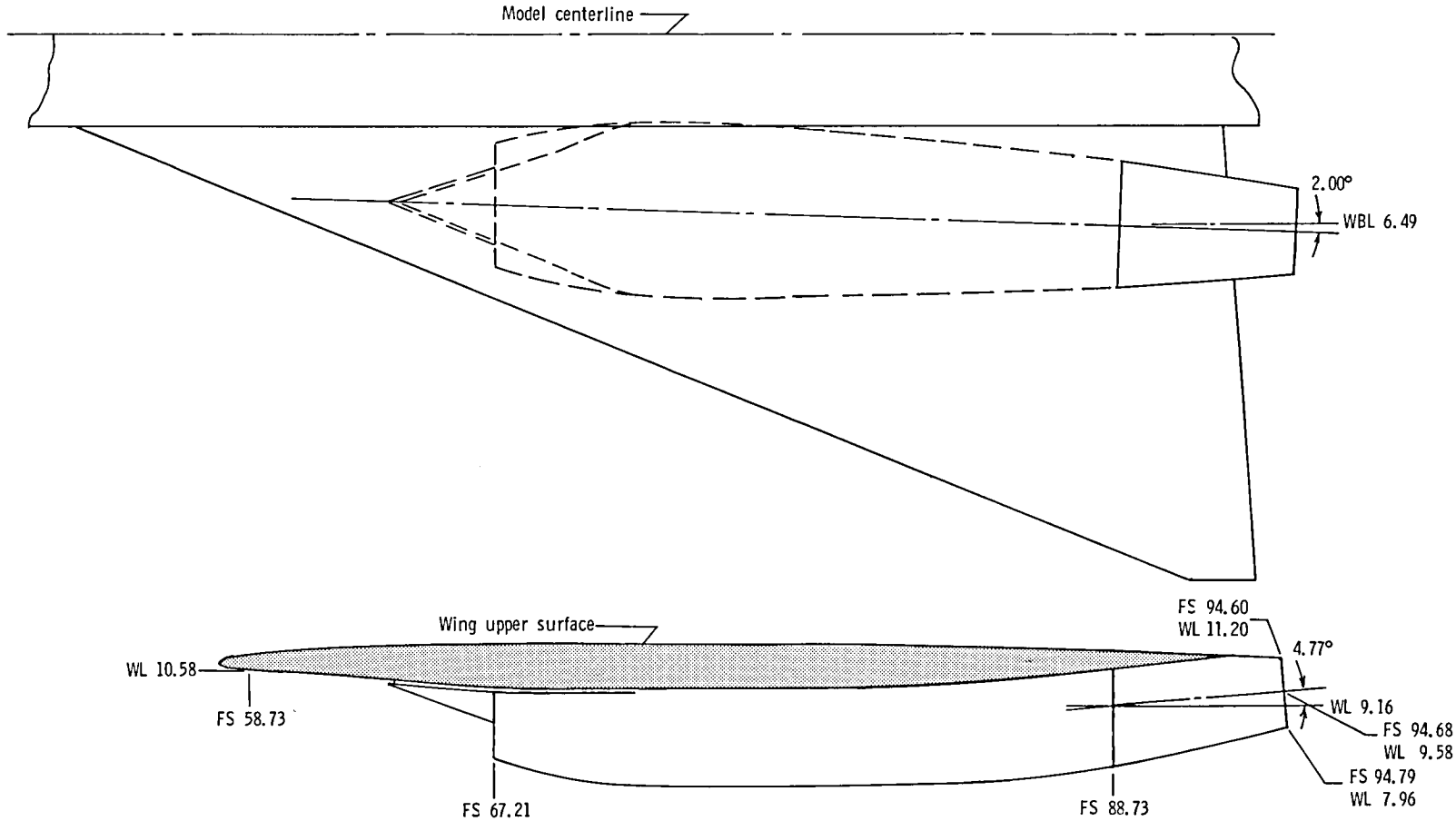

(a) Nacelle installation.

Figure 6.- Nacelle installation and inlet and exit details. All linear dimensions in inches unless otherwise indicated.

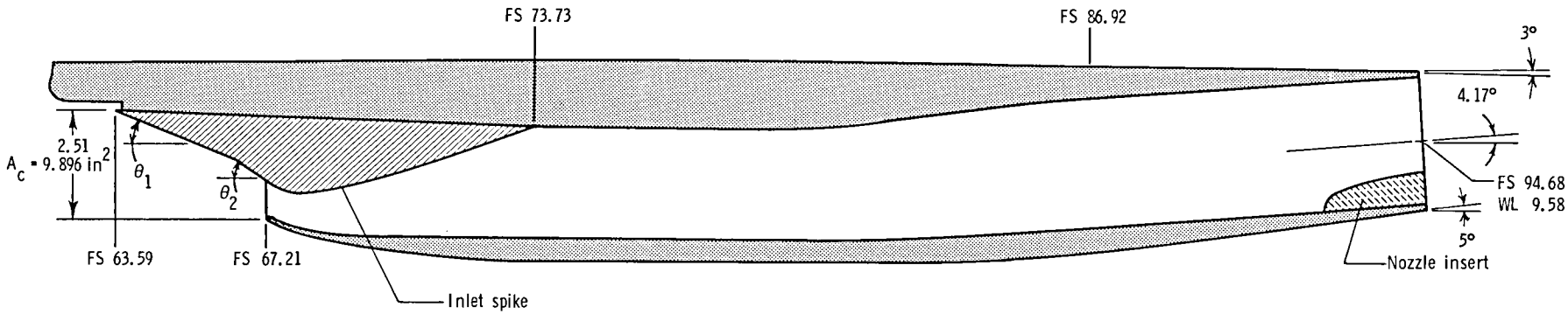

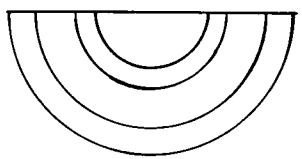

M_{in}	θ_1, deg	θ_2, deg
1.50	12	12
1.75	20	24
2.00	20	29
2.20	20	33

A_e/A_c	d_e, in.	A_e, in^2
0.555	1.82	5.492
.636	2.08	6.294
.700	2.29	6.927
.779	2.55	7.709
.850	2.78	8.412
.924	3.02	9.144

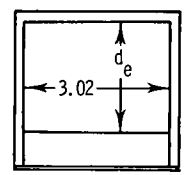

(b) Inlet and exit details.

Figure 6.- Continued.

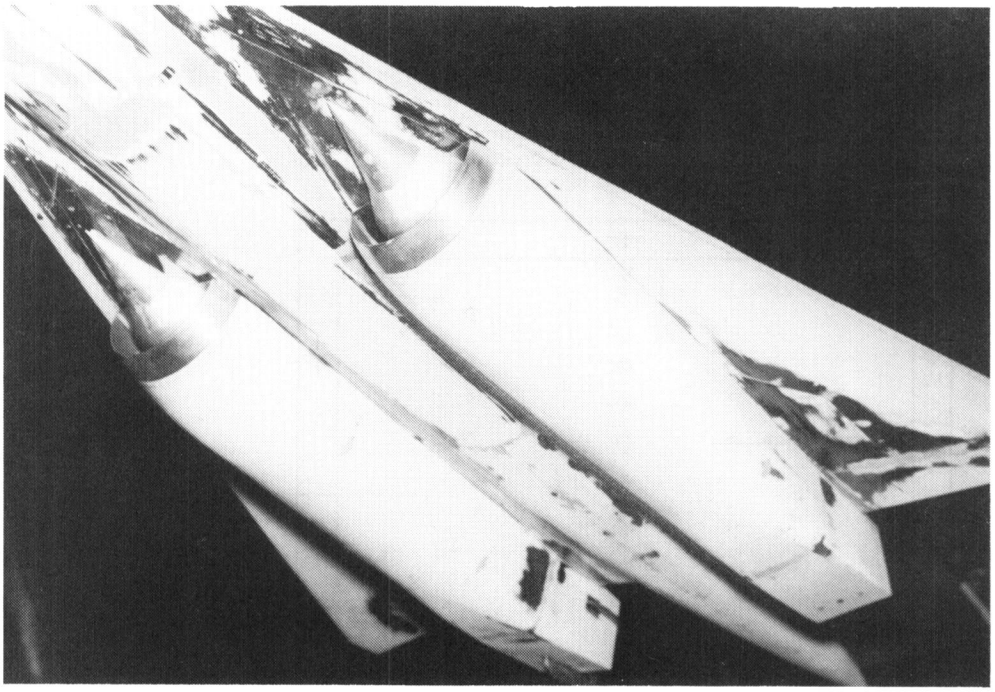

$M_{in} = 2.00$

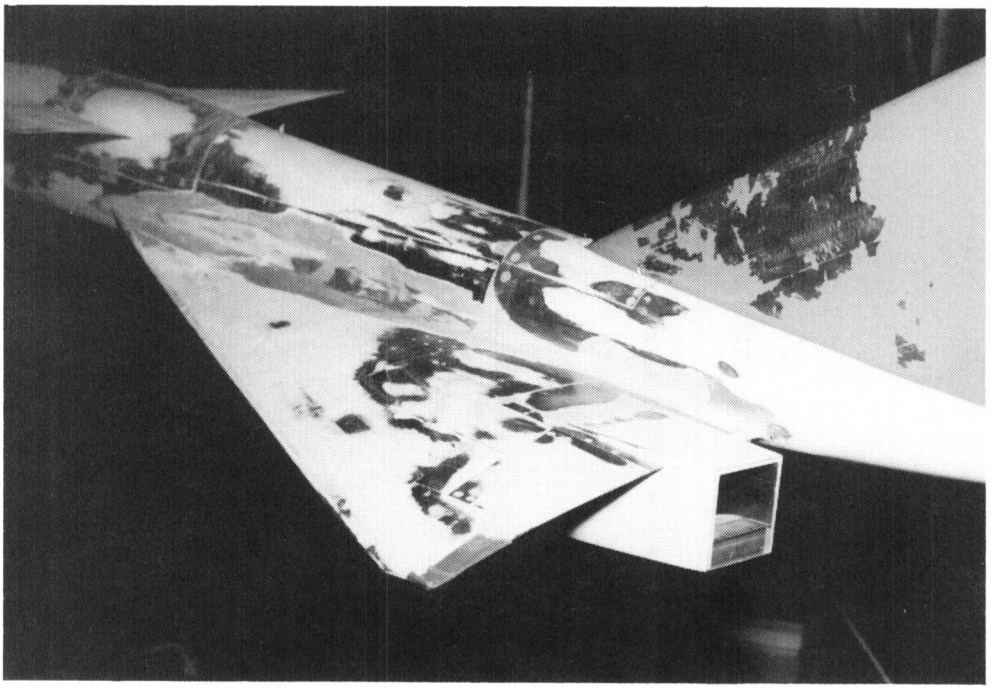

$A_e/A_c = 0.636$

(c) Photographs.

Figure 6.- Concluded.

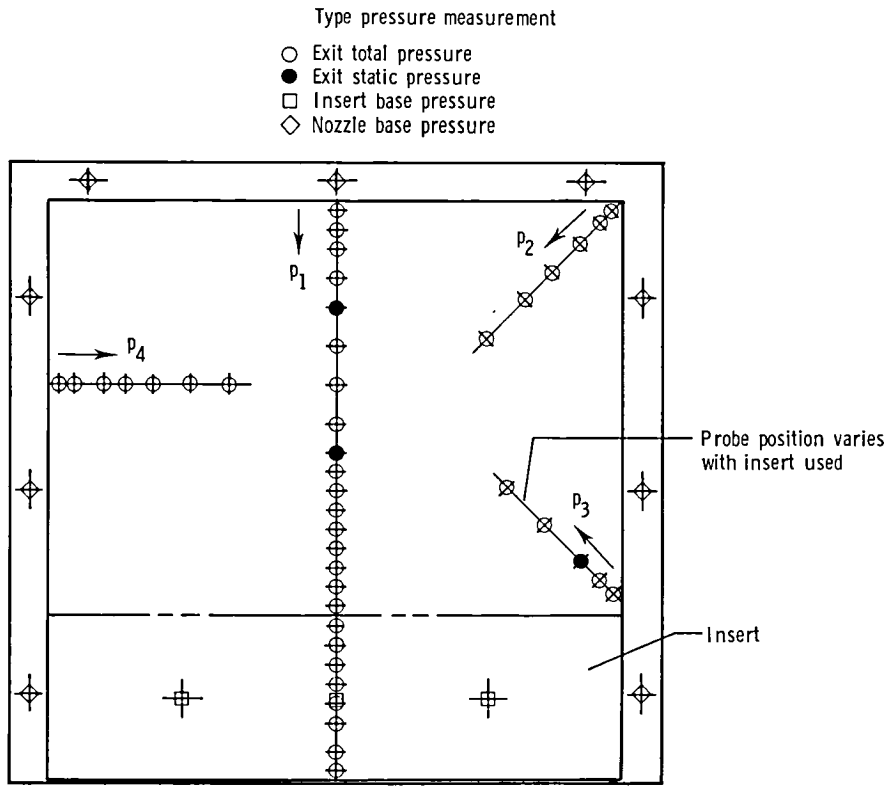

Probe	p_1	p_2	p_3	p_4
1	0.05	0.05	0.05	0.05
2	.15	.15	.15	.15
3	.25	.38	.40	.30
4	.40	.52	.55	.40
5	.55	.73	.76	.55
6	.75	1.01		.75
7	.95			.95
8	1.15			
9	1.30			
10	1.40			
11	1.50			
12	1.60			
13	1.70			
14	1.80			
15	1.90			
16	2.00			
17	2.10			
18	2.20			
19	2.30			
20	2.40			
21	2.50			
22	2.60			
23	2.70			
24	2.85			
25	2.95			

(a) Probe dimensions.

Figure 7.- Nozzle exit pressure instrumentation.
All dimensions in inches.

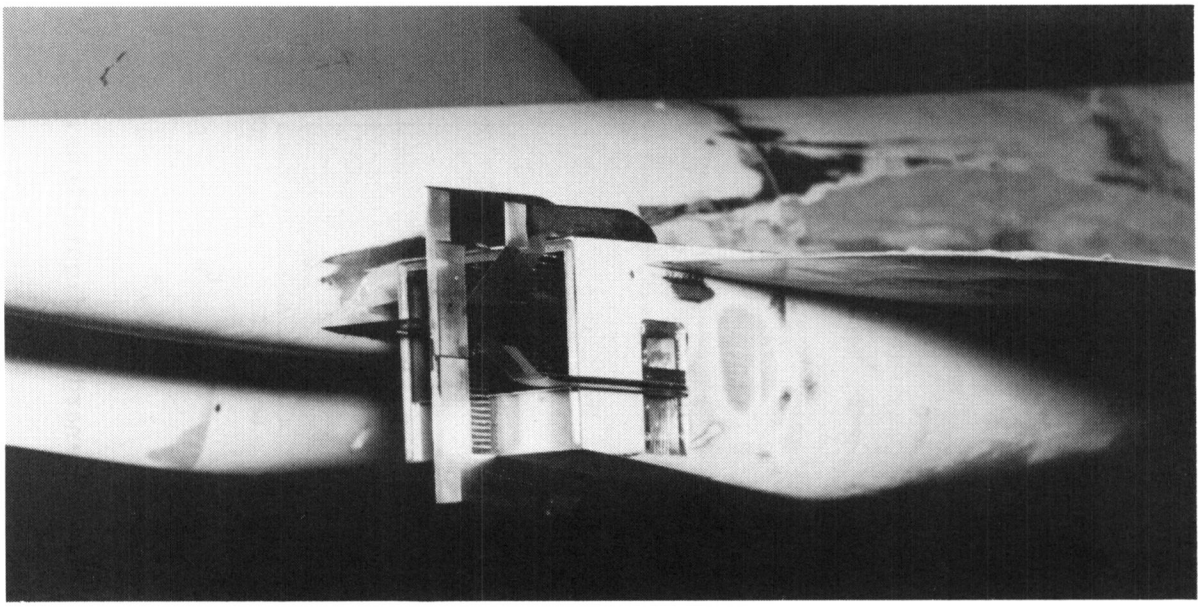

A_e/A_c = 0.636

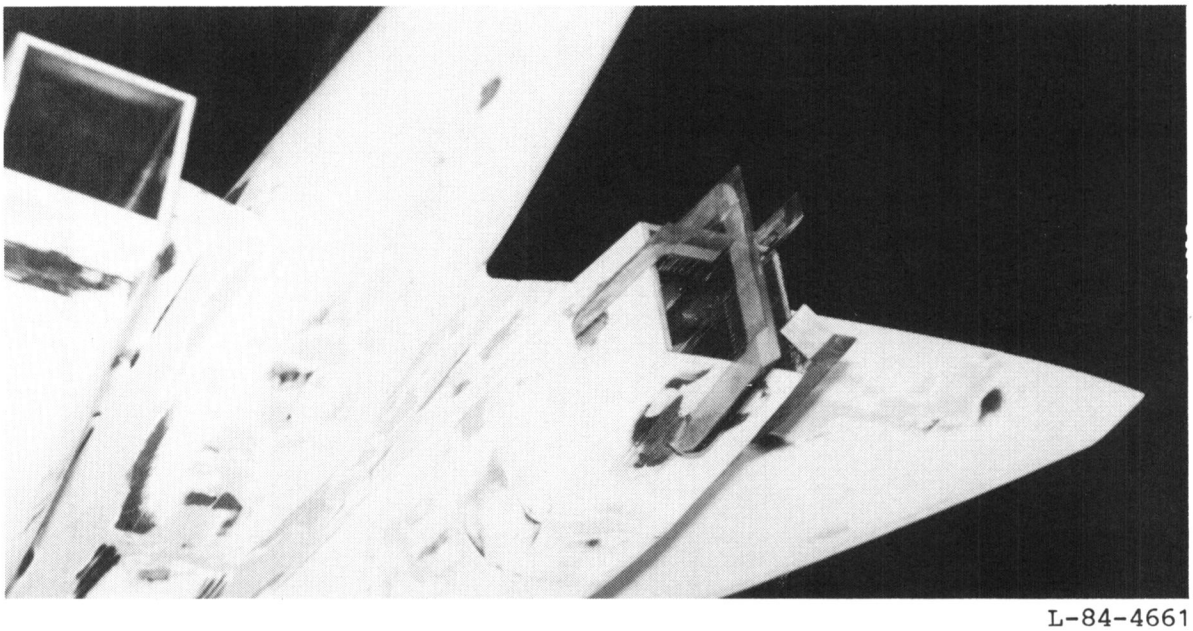

L-84-4661

A_e/A_c = 0.924

(b) Photographs.

Figure 7.- Concluded.

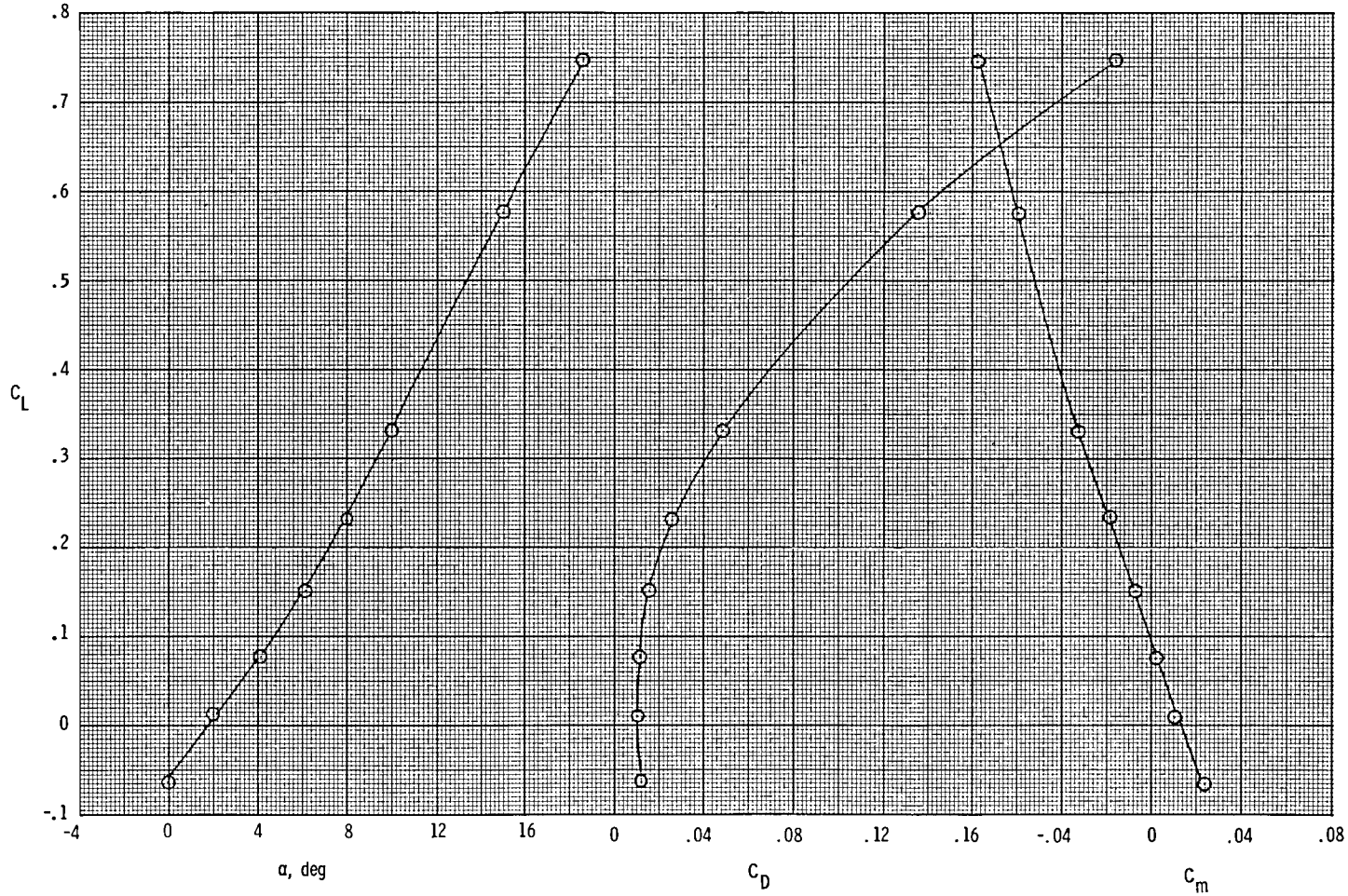

(a) M = 0.40; canard off.

Figure 8.- Longitudinal characteristics of wing-body and wing-body-canard configurations.

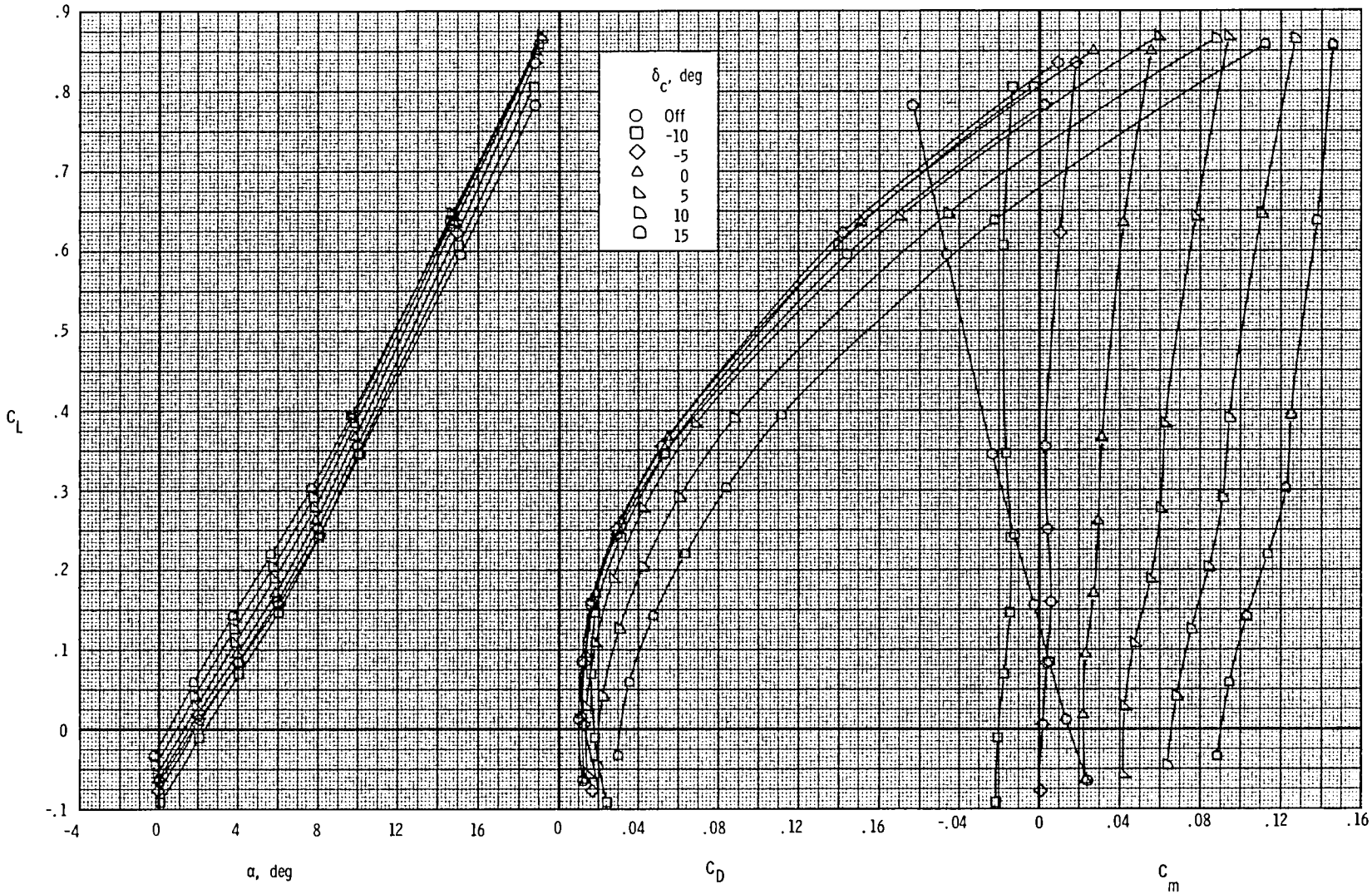

(b) M = 0.60.

Figure 8.- Continued.

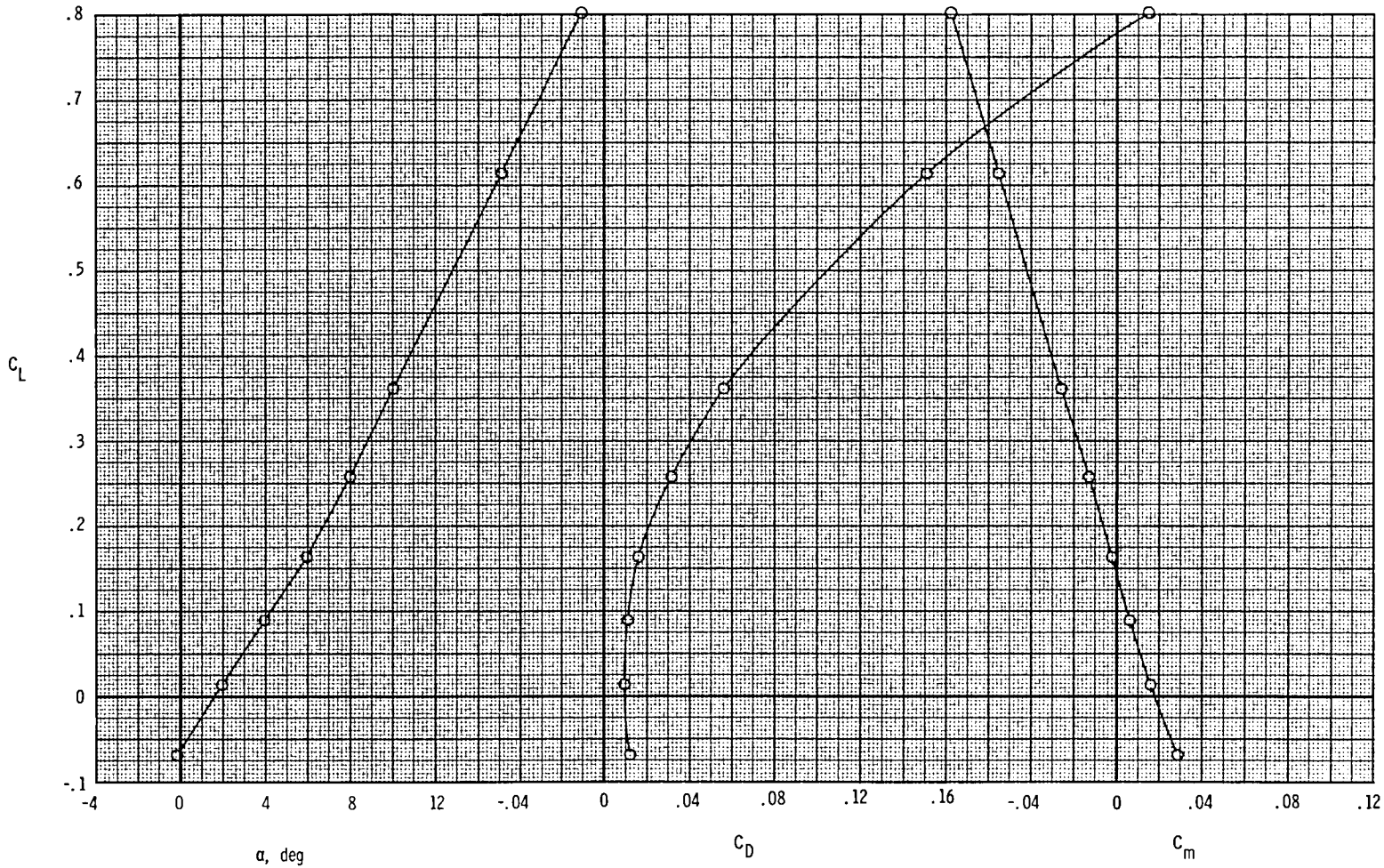

(c) M = 0.80; canard off.

Figure 8.- Continued.

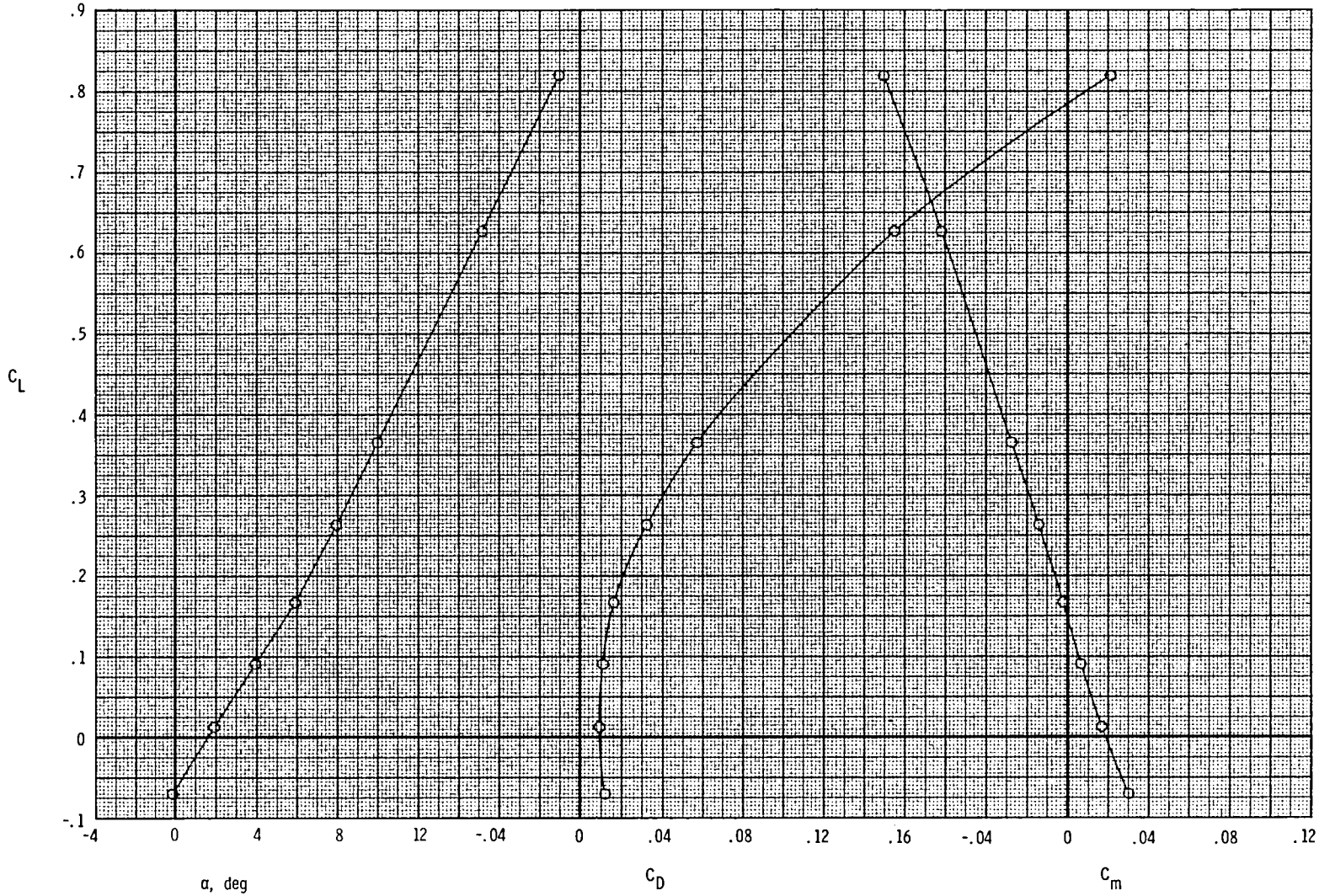

(d) M = 0.85; canard off.

Figure 8.- Continued.

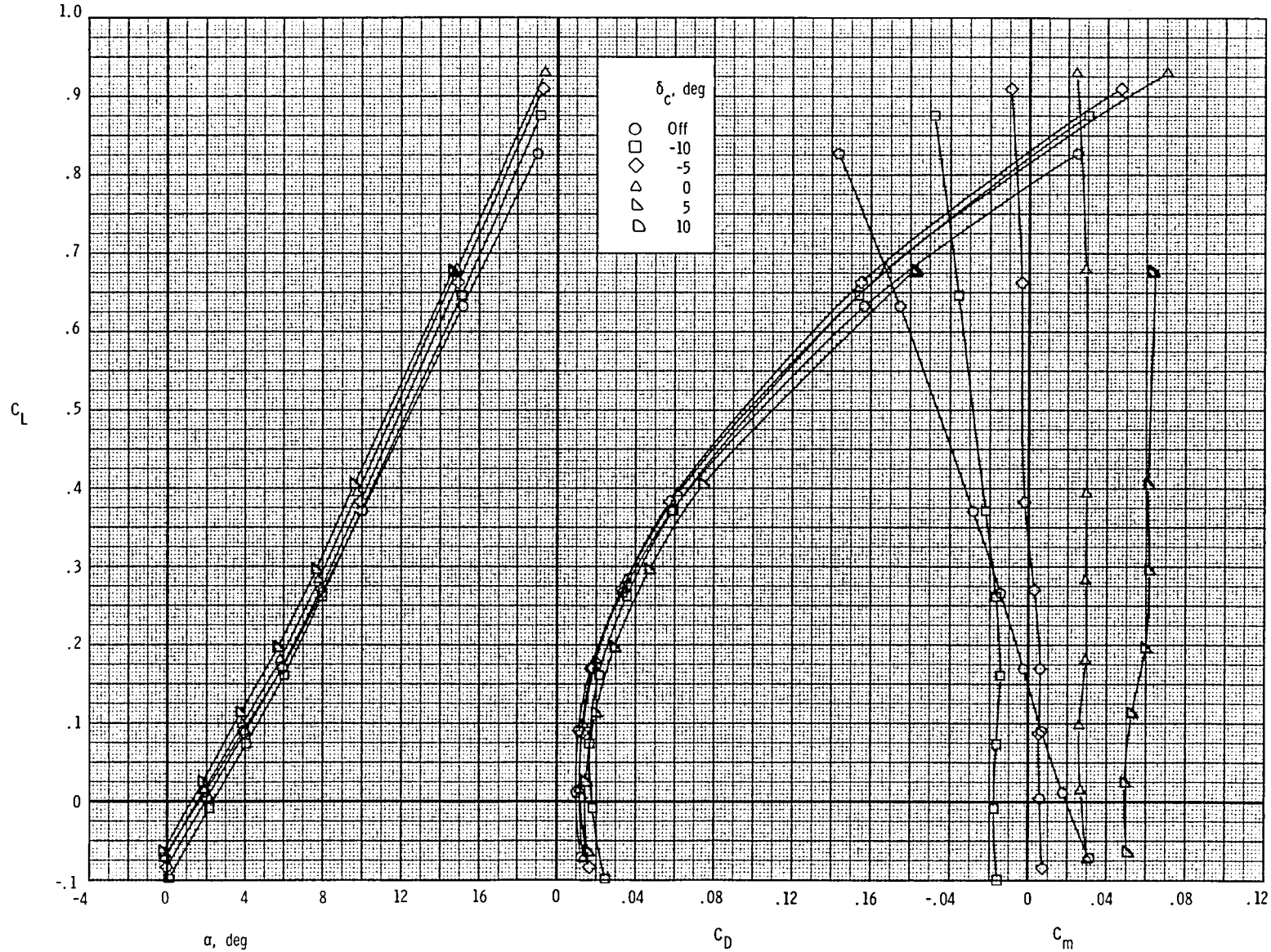

(e) M = 0.87.

Figure 8.- Continued.

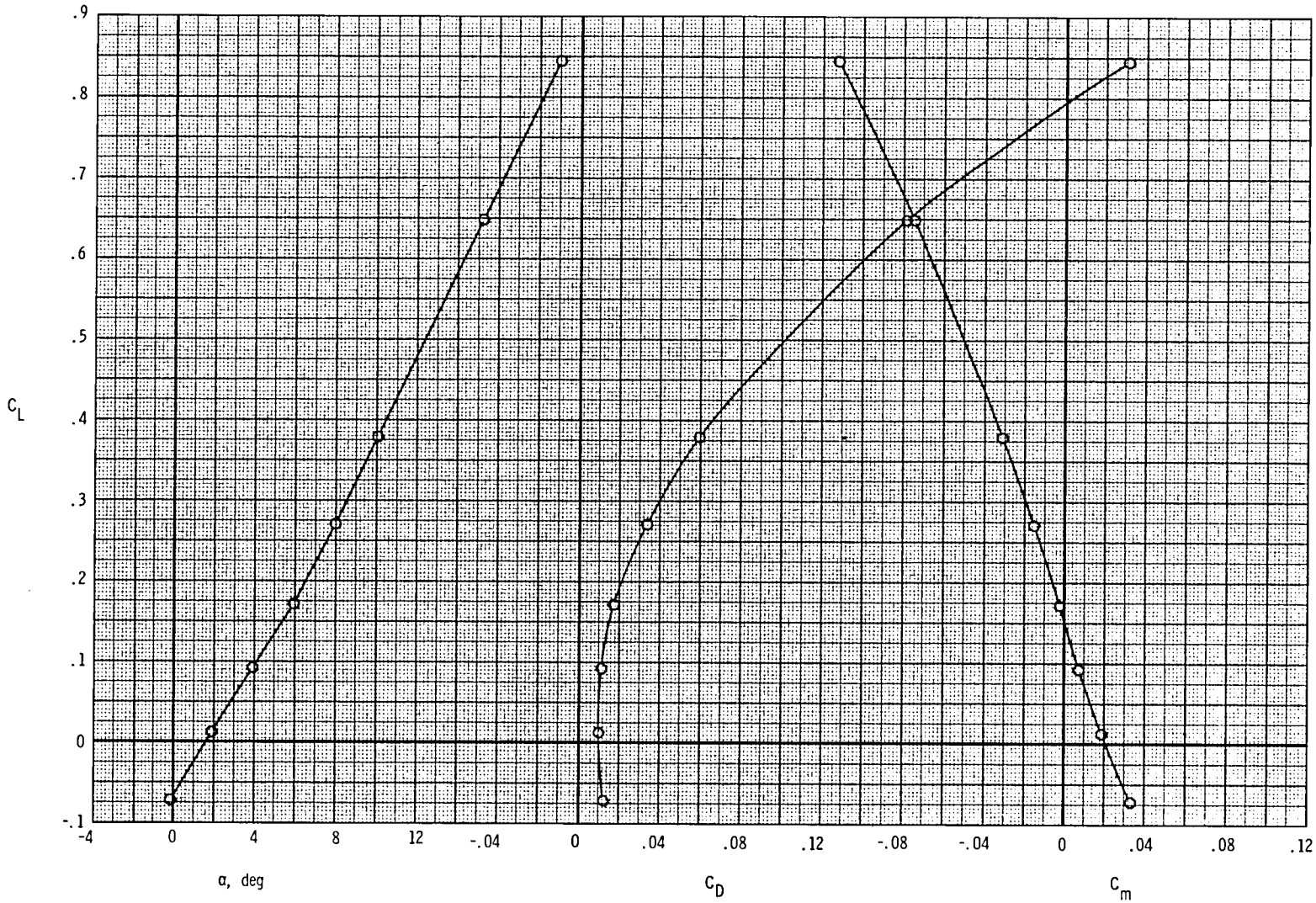

(f) M = 0.90; canard off.

Figure 8.- Continued.

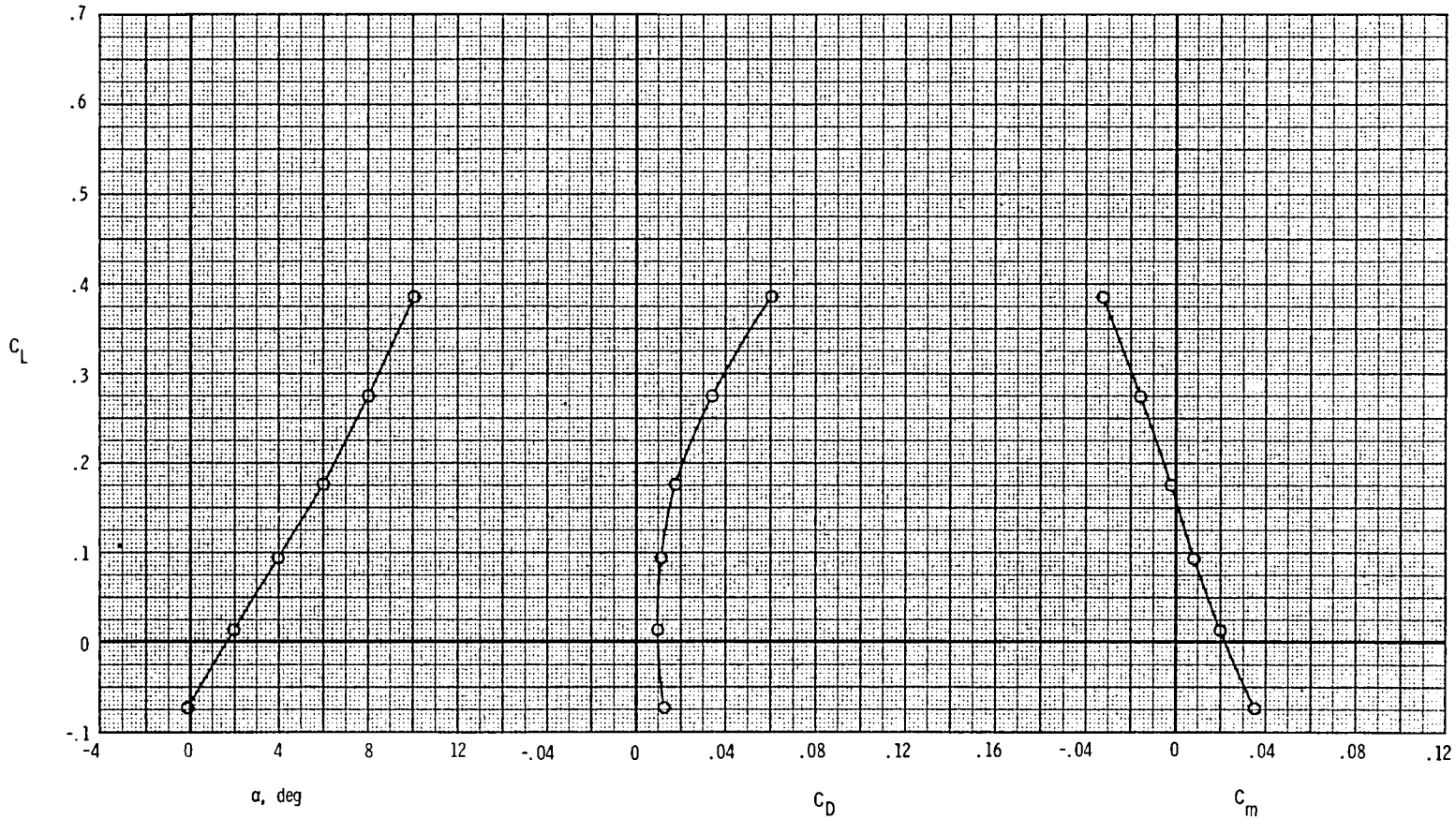

(g) M = 0.92; canard off.

Figure 8.- Continued.

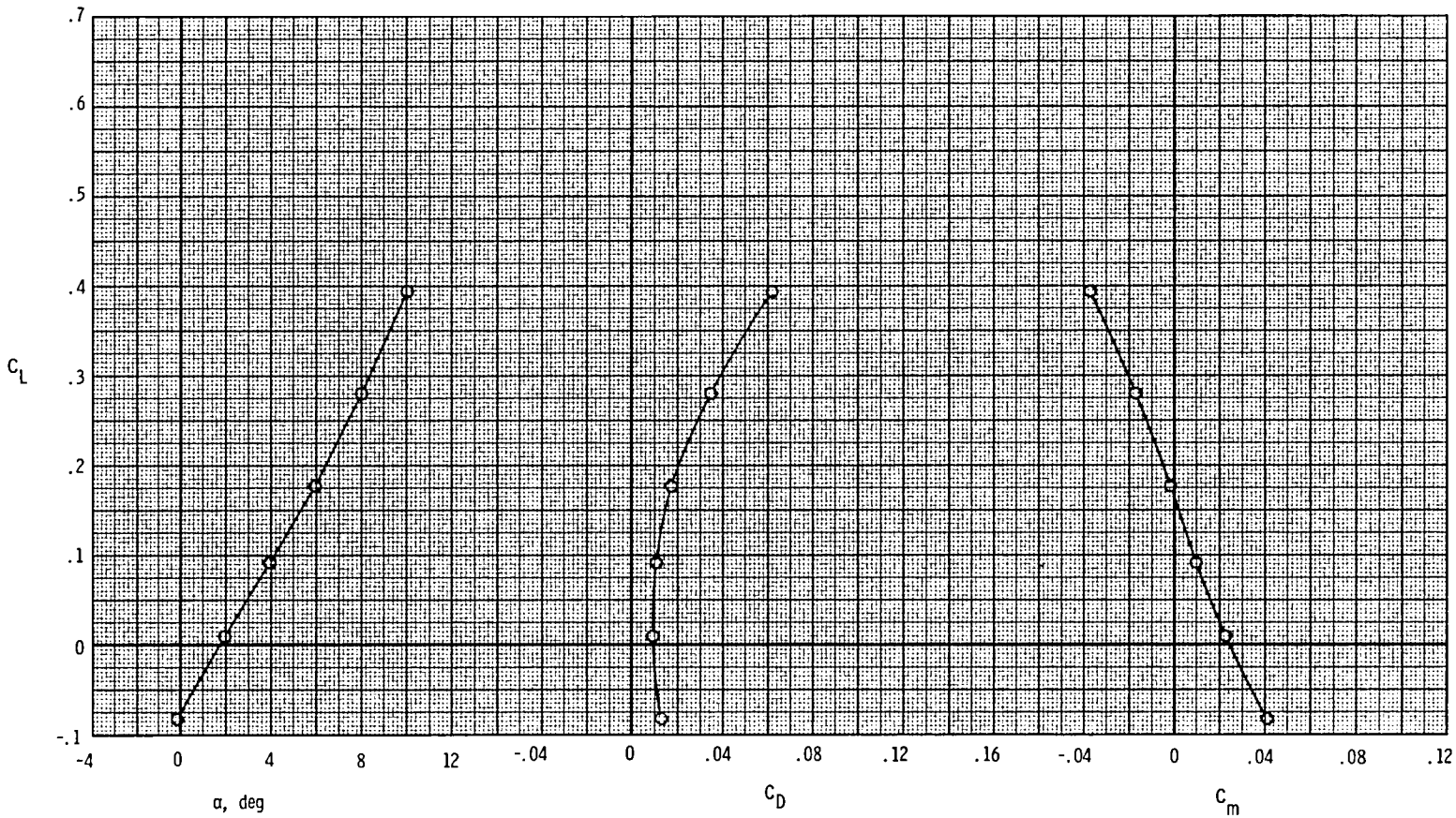

(h) M = 0.95; canard off.

Figure 8.- Continued.

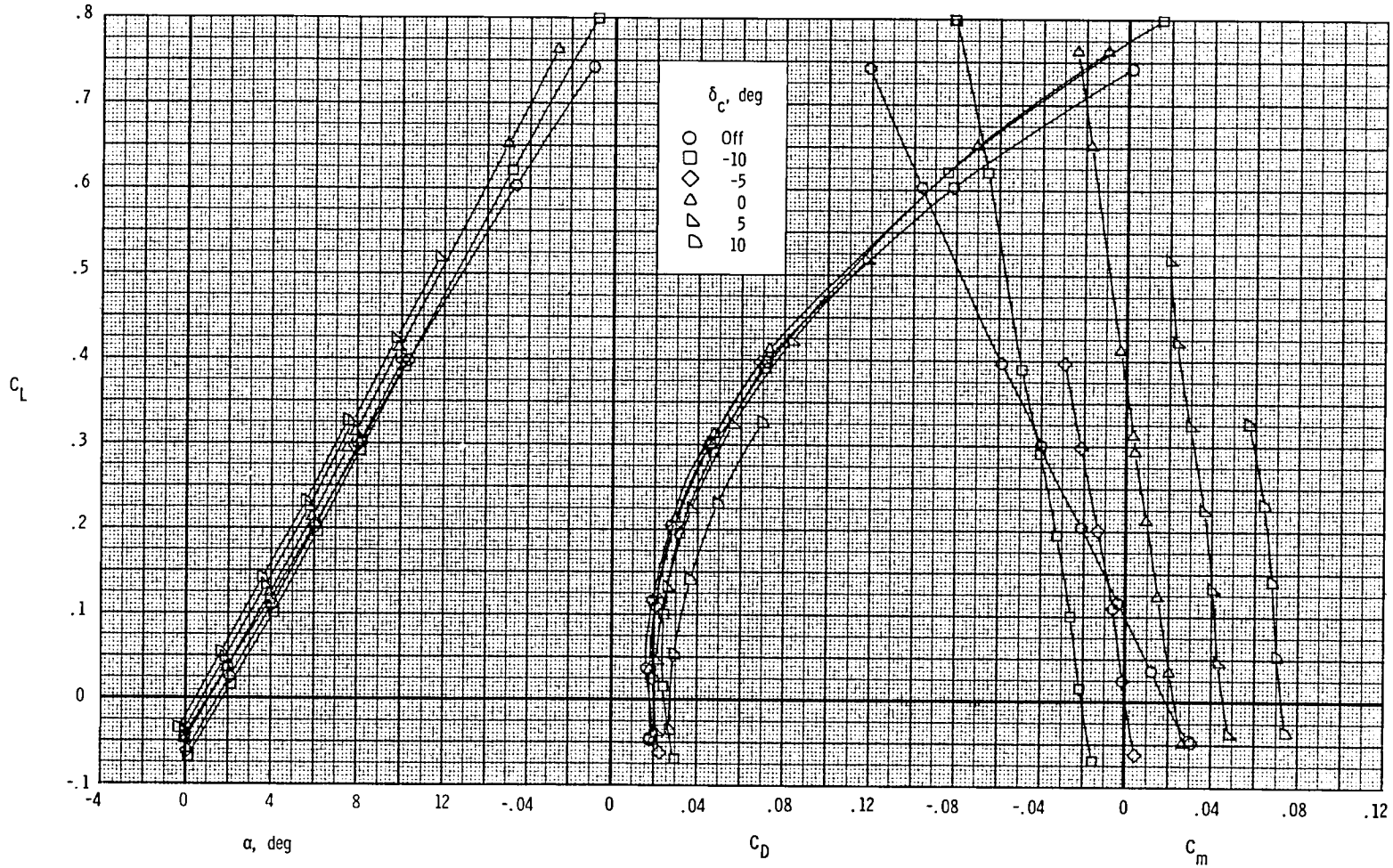

(i) M = 1.20.

Figure 8.- Continued.

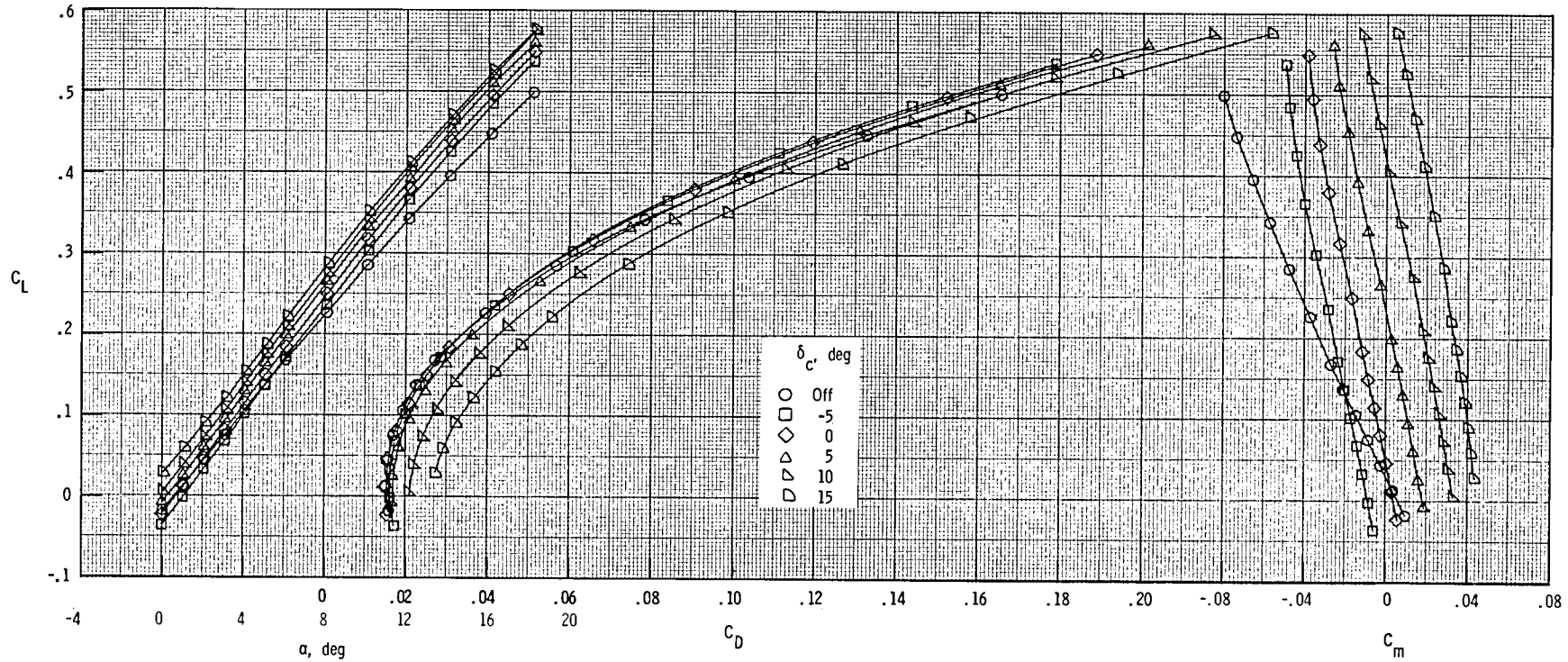

(j) M = 2.00.

Figure 8.- Continued.

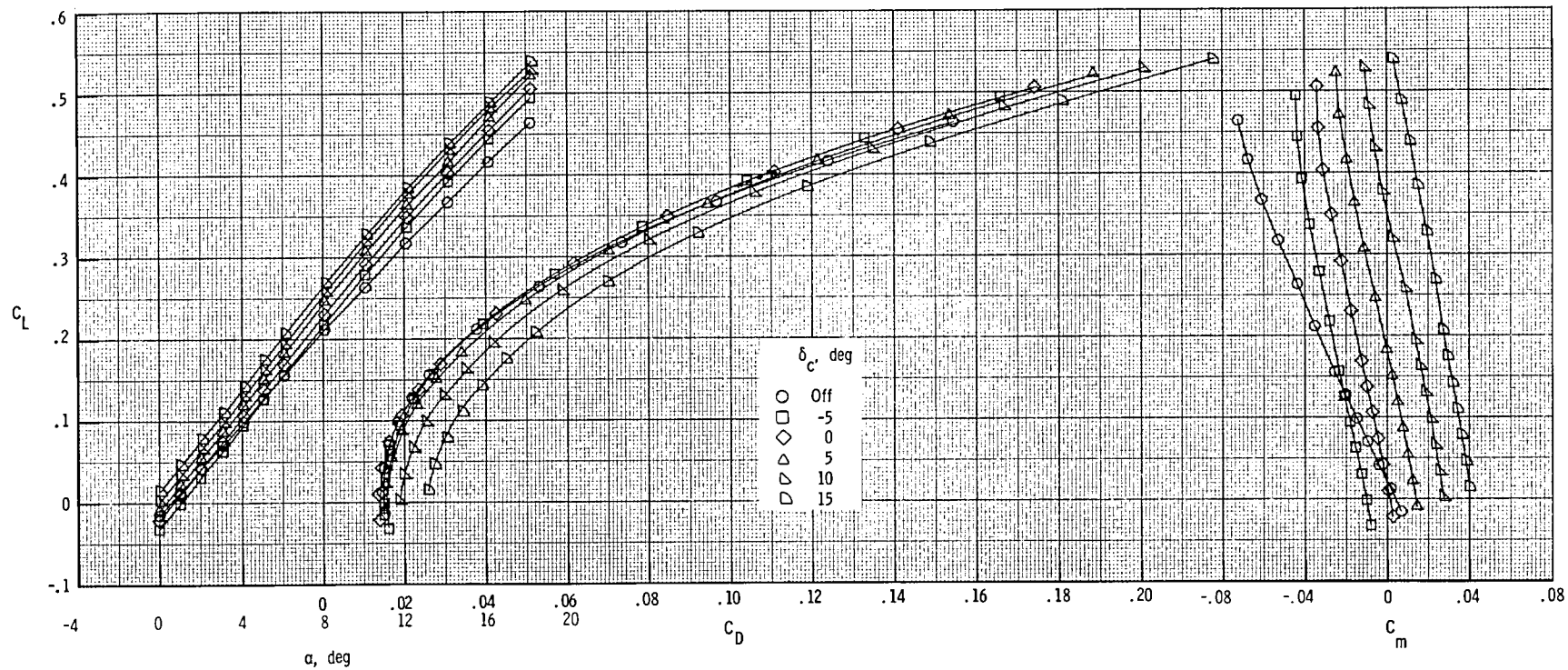

(k) M = 2.17.

Figure 8.- Continued.

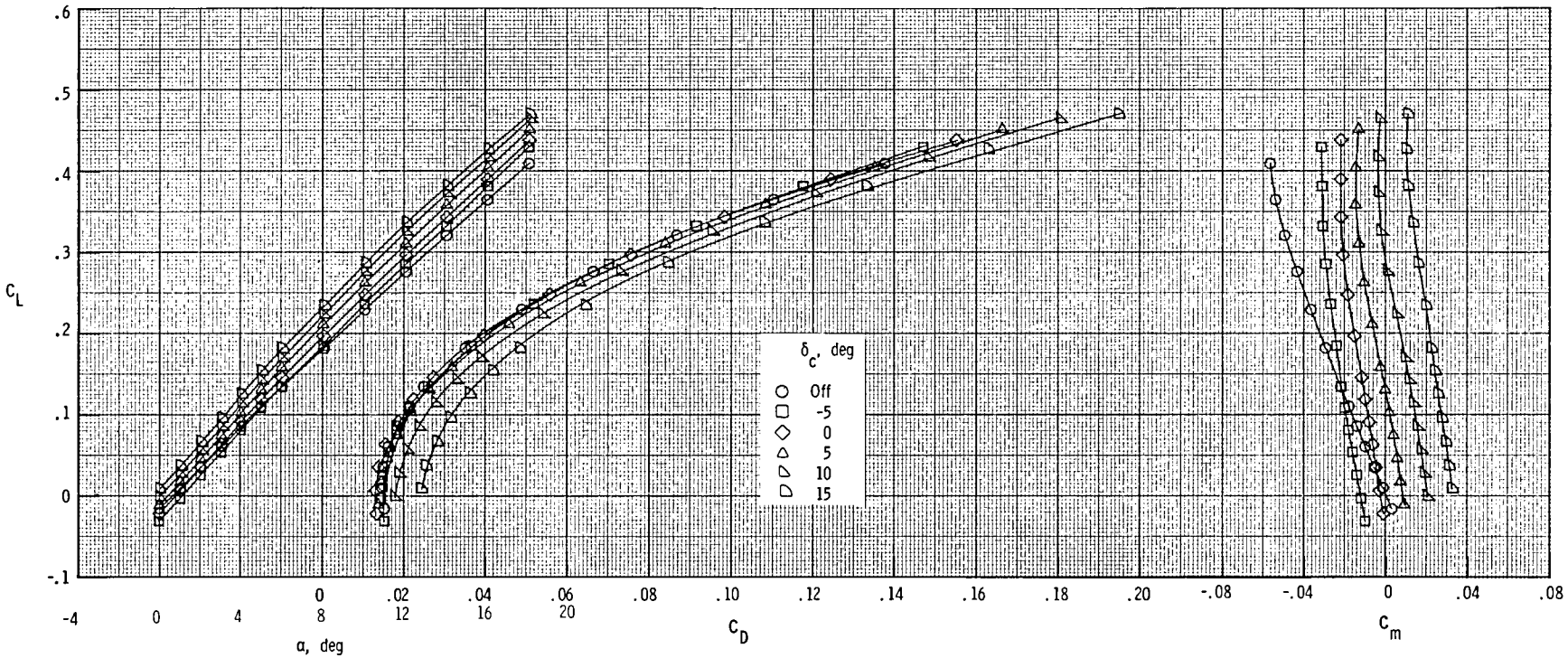

(1) M = 2.47.

Figure 8.- Concluded.

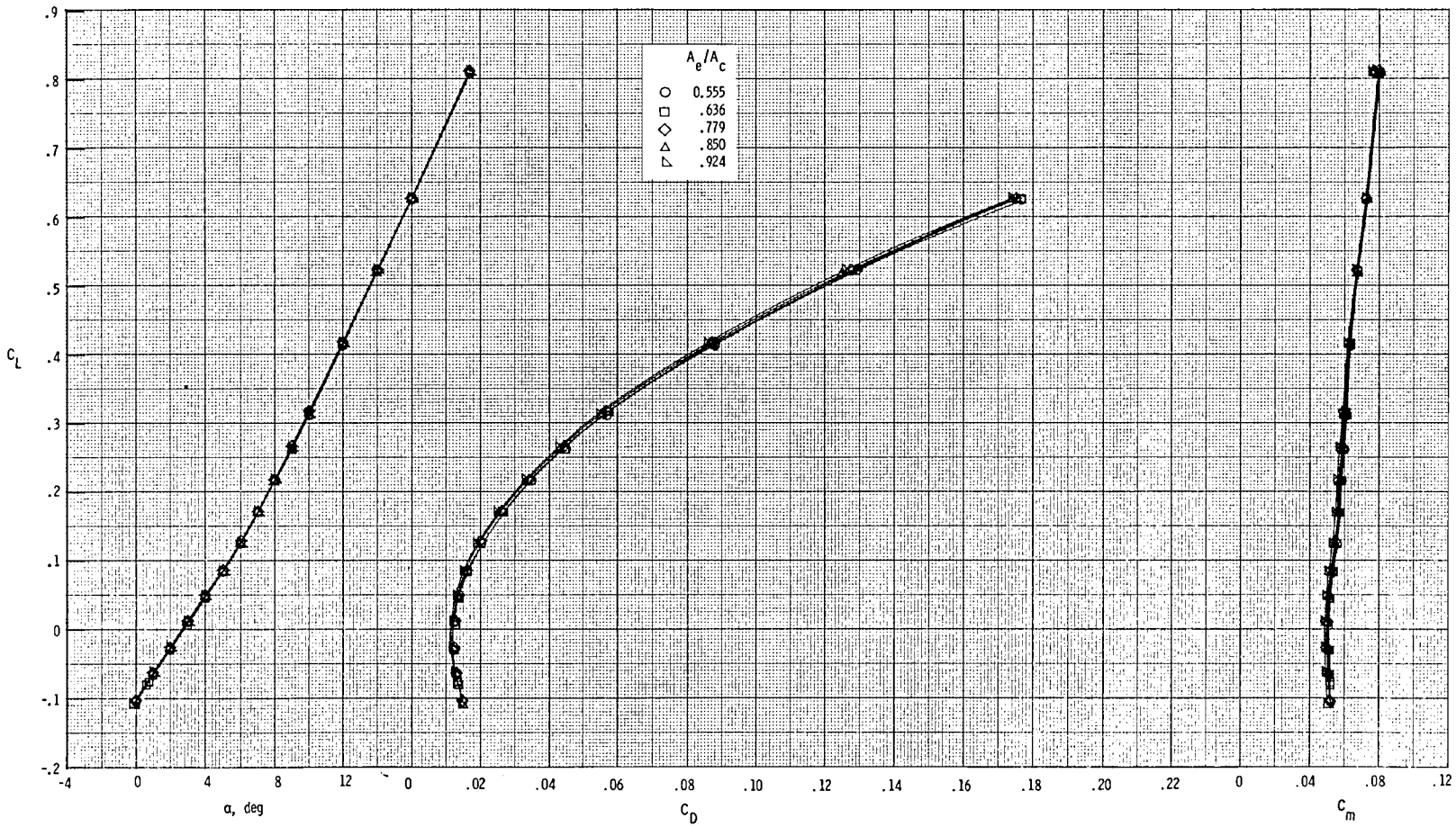

(a) M = 0.60.

Figure 9.- Effect of inlet mass flow ratio on longitudinal aerodynamic characteristics for WBCN with inlet spike designed for $M_{in} < 1.50$.

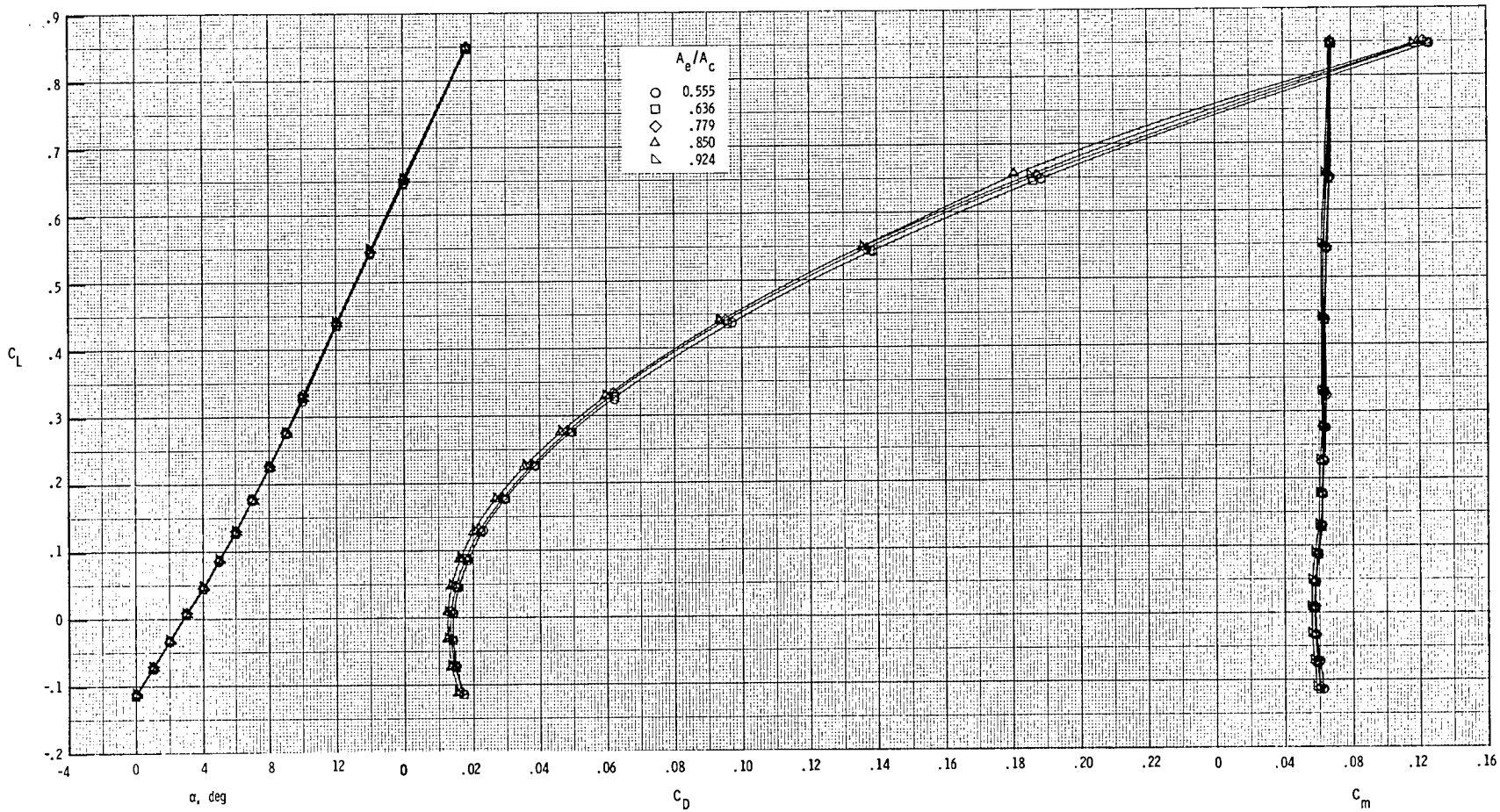

(b) M = 0.80.

Figure 9.- Continued.

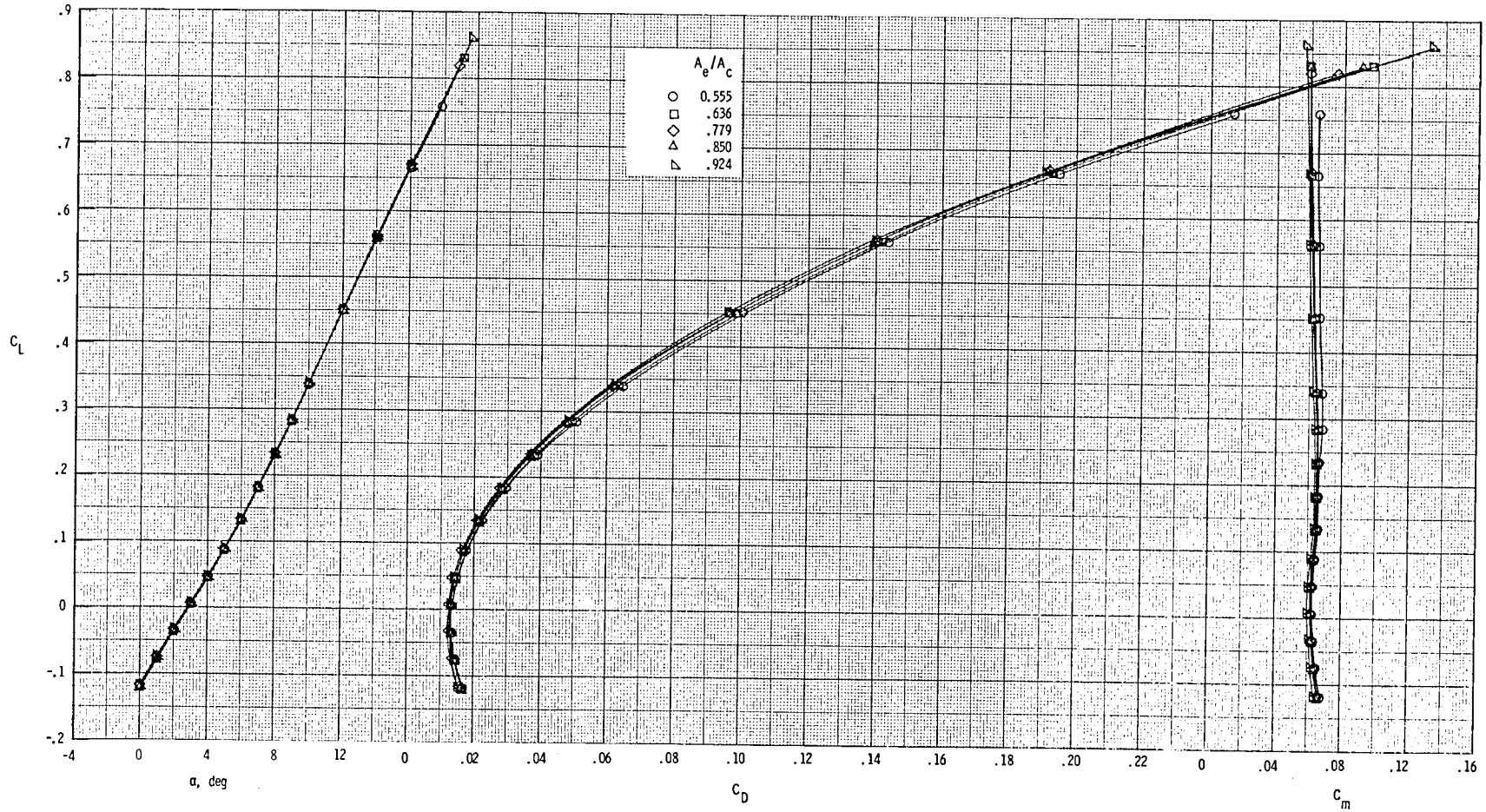

(c) M = 0.87.

Figure 9.- Continued.

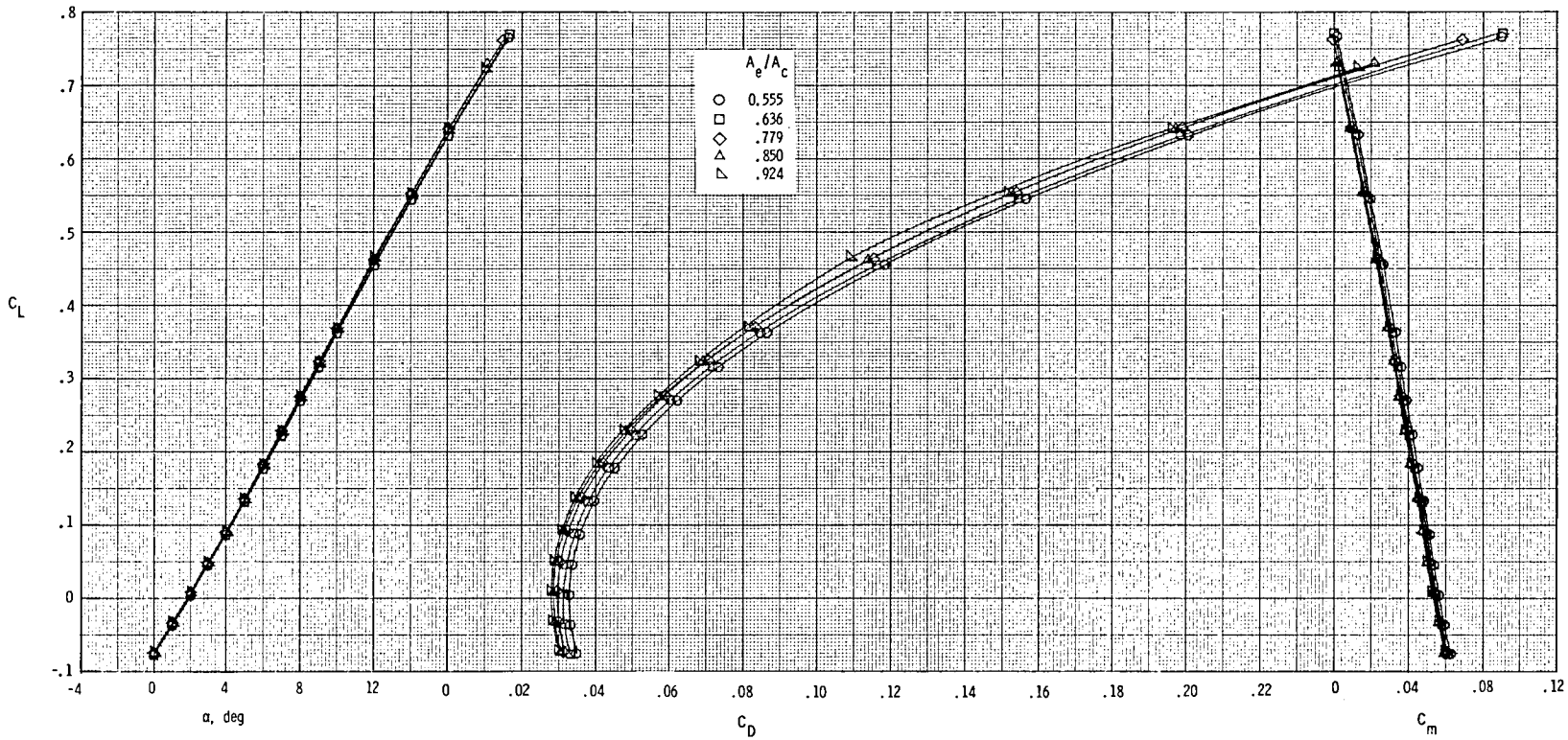

(d) M = 1.20.

Figure 9.- Concluded.

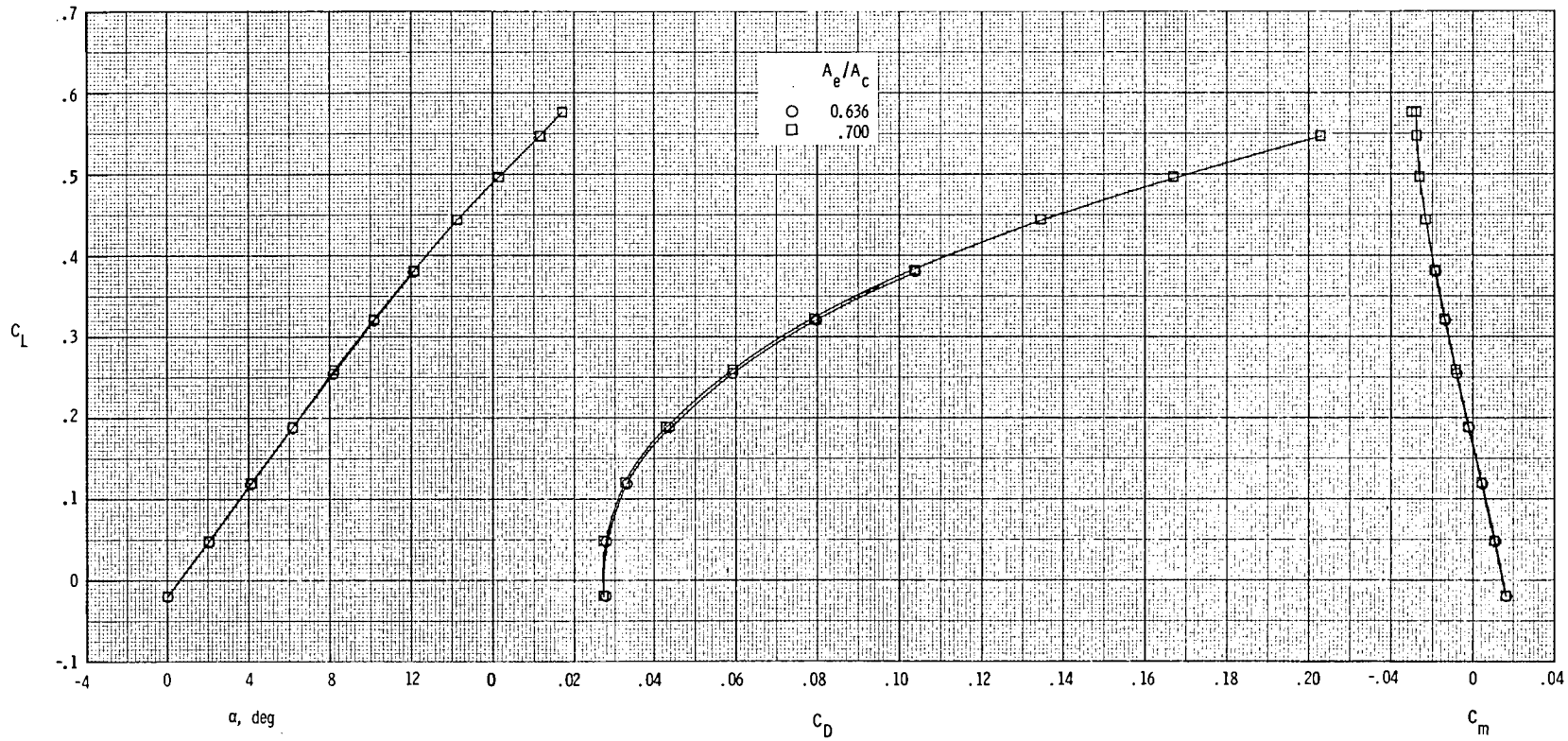

(a) M = 2.00.

Figure 10.- Effect of inlet mass flow ratio on longitudinal aerodynamic characteristics for WBCN with inlet spike designed for M_{in} = 1.75.

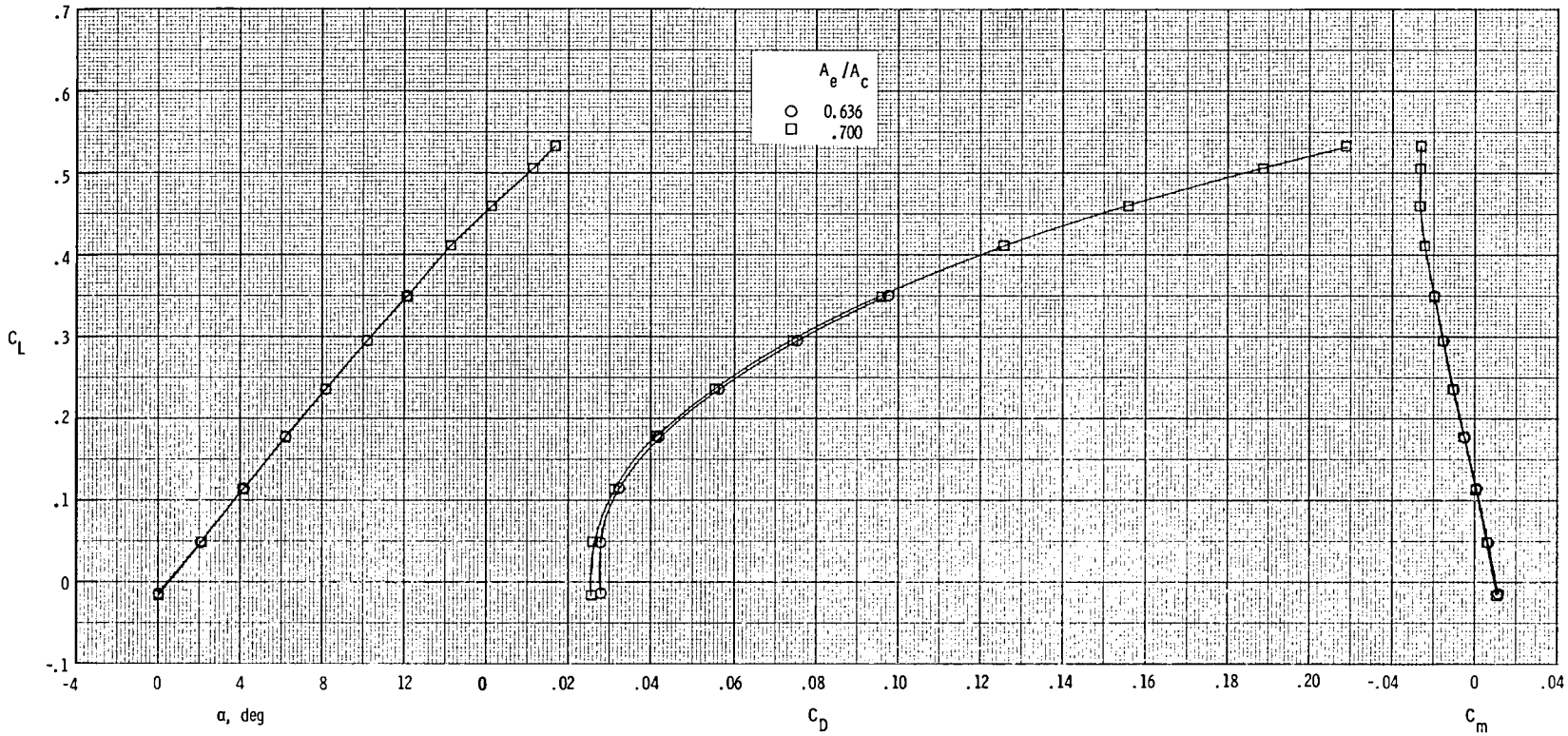

(b) M = 2.17.

Figure 10.- Continued.

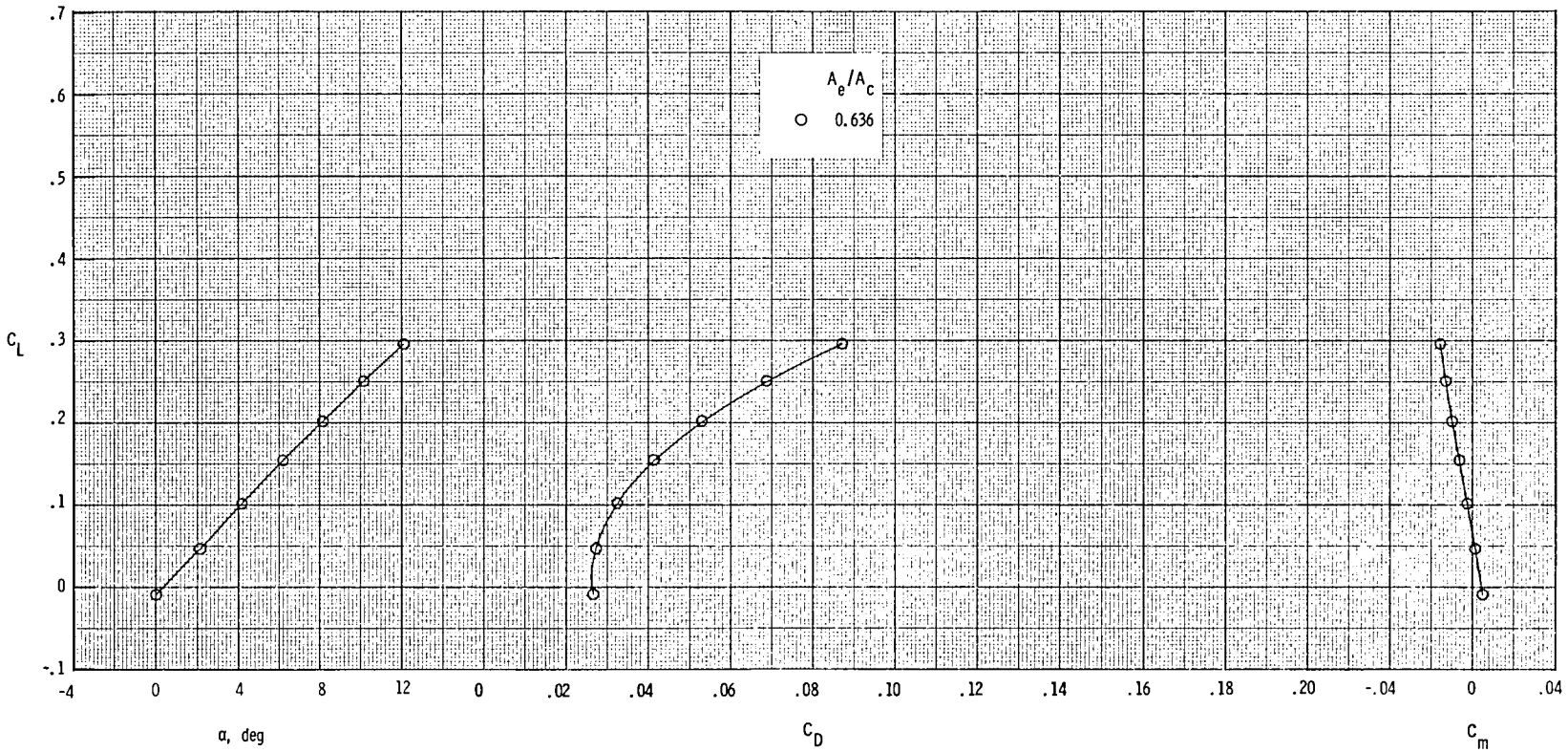

(c) M = 2.47.

Figure 10.- Concluded.

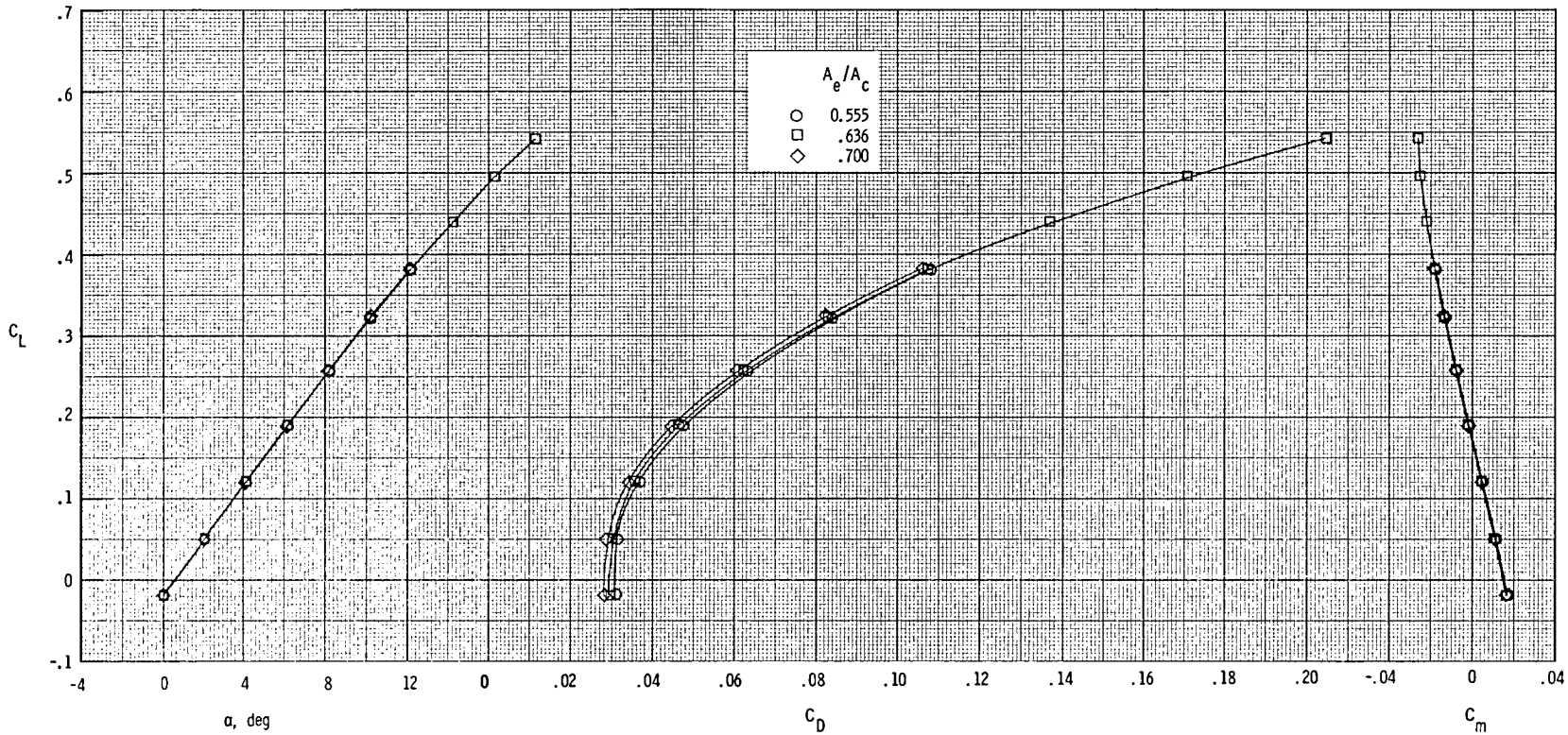

(a) M = 2.00.

Figure 11.- Effect of inlet mass flow ratio on longitudinal aerodynamic characteristics for WBCN with inlet spike designed for M_{in} = 2.00.

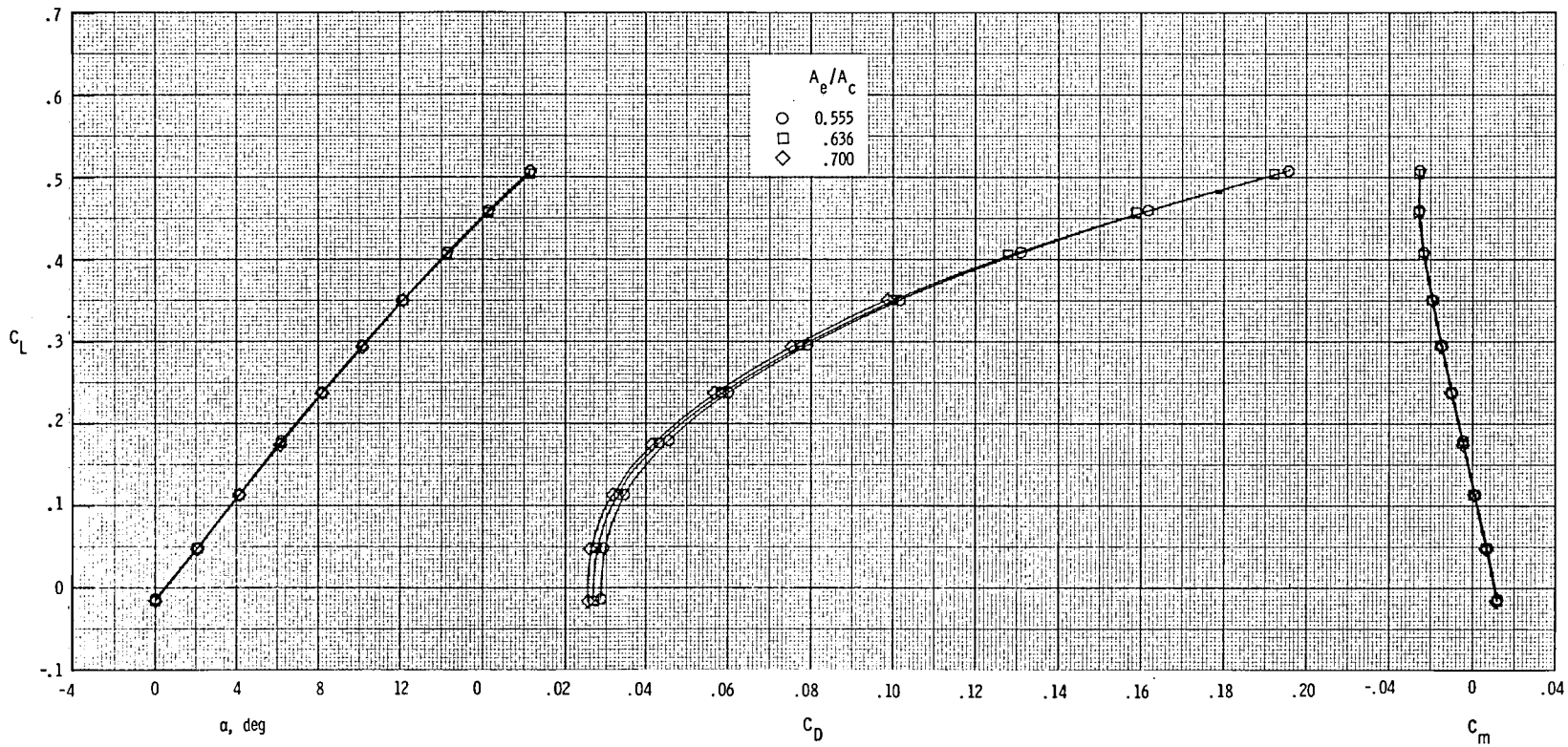

(b) M = 2.17.

Figure 11.- Continued.

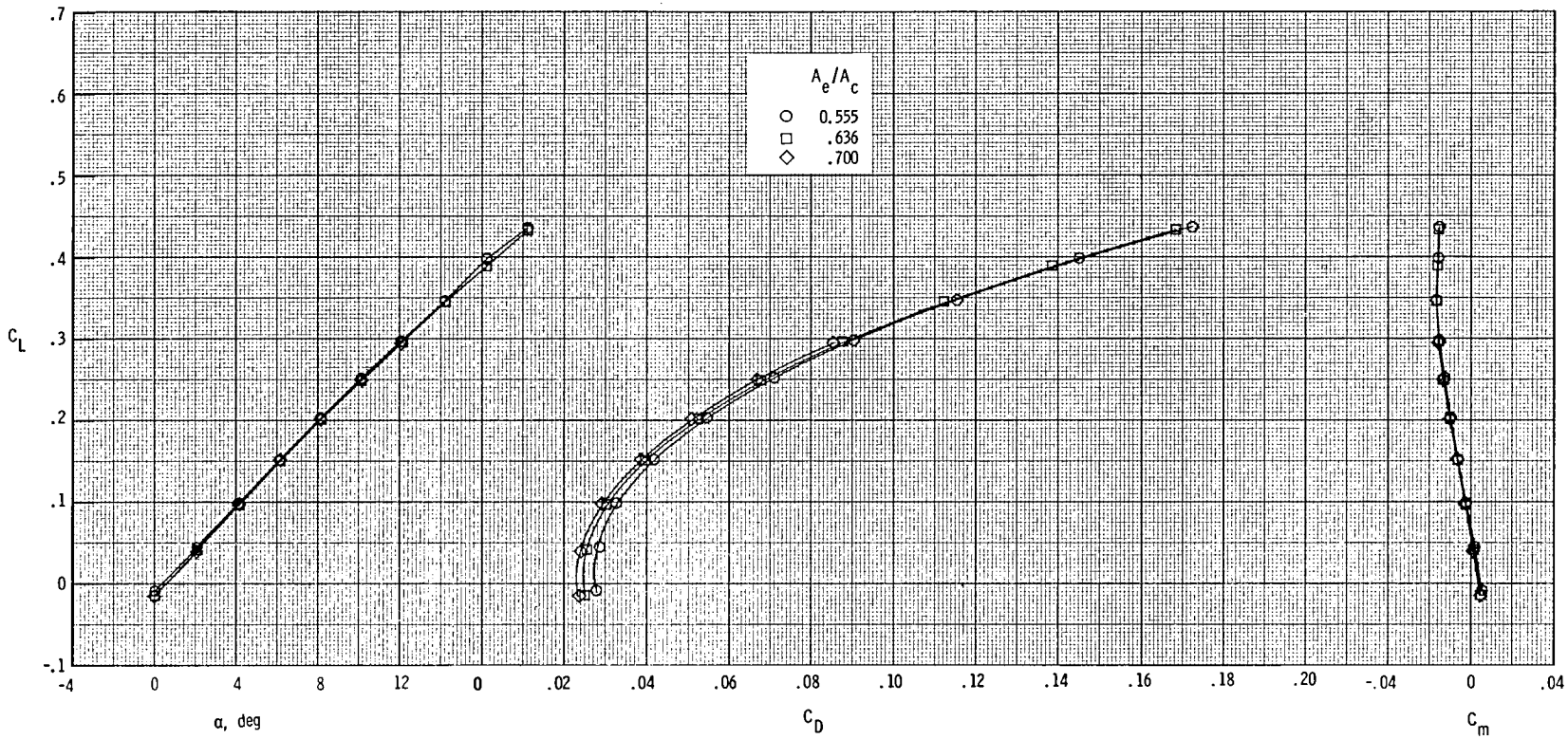

(c) M = 2.47.

Figure 11.- Concluded.

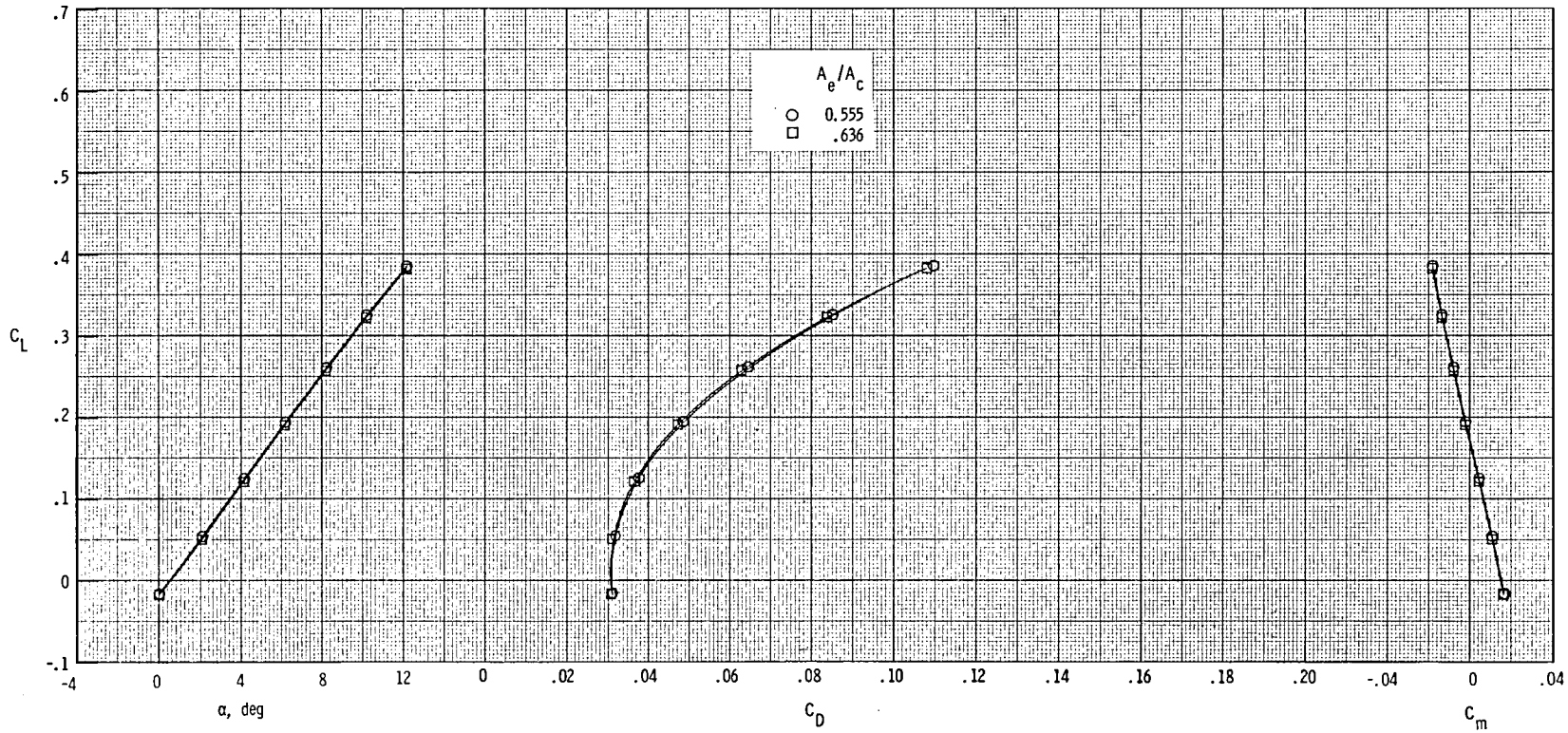

(a) M = 2.00.

Figure 12.- Effect of inlet mass flow ratio on longitudinal aerodynamic characteristics for WBCN with inlet spike designed for M_{in} = 2.20.

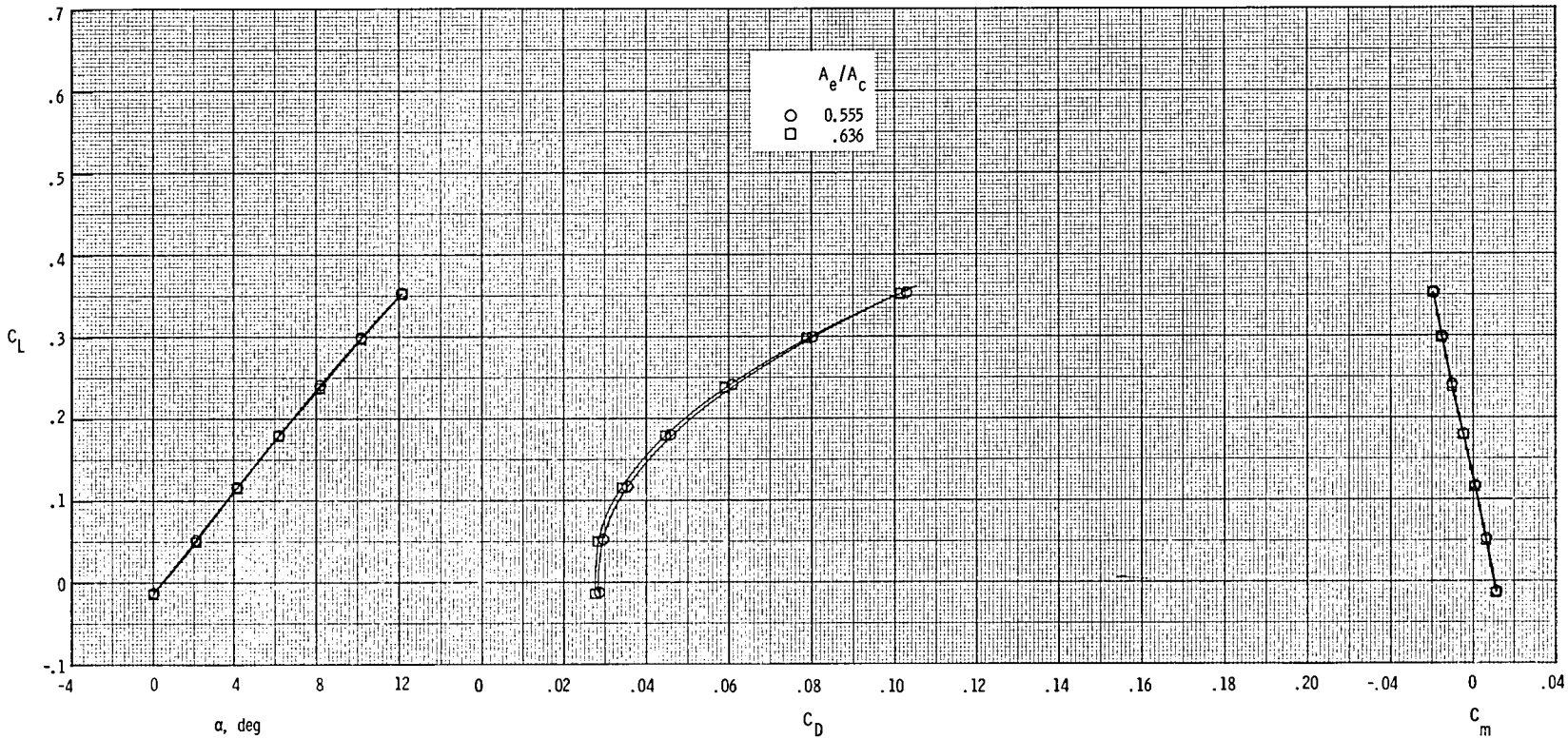

(b) M = 2.17.

Figure 12.- Continued.

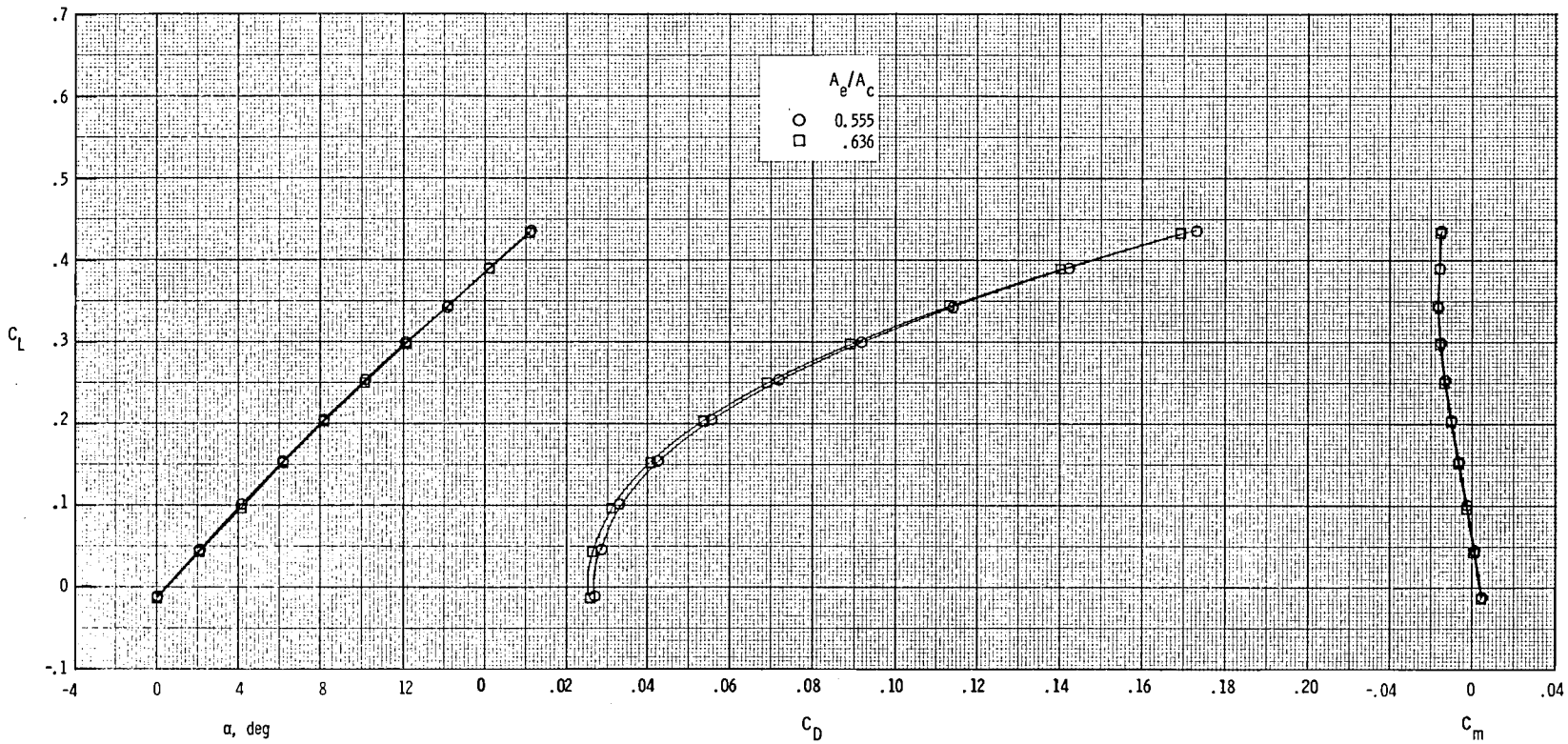

(c) M = 2.47.

Figure 12.- Concluded.

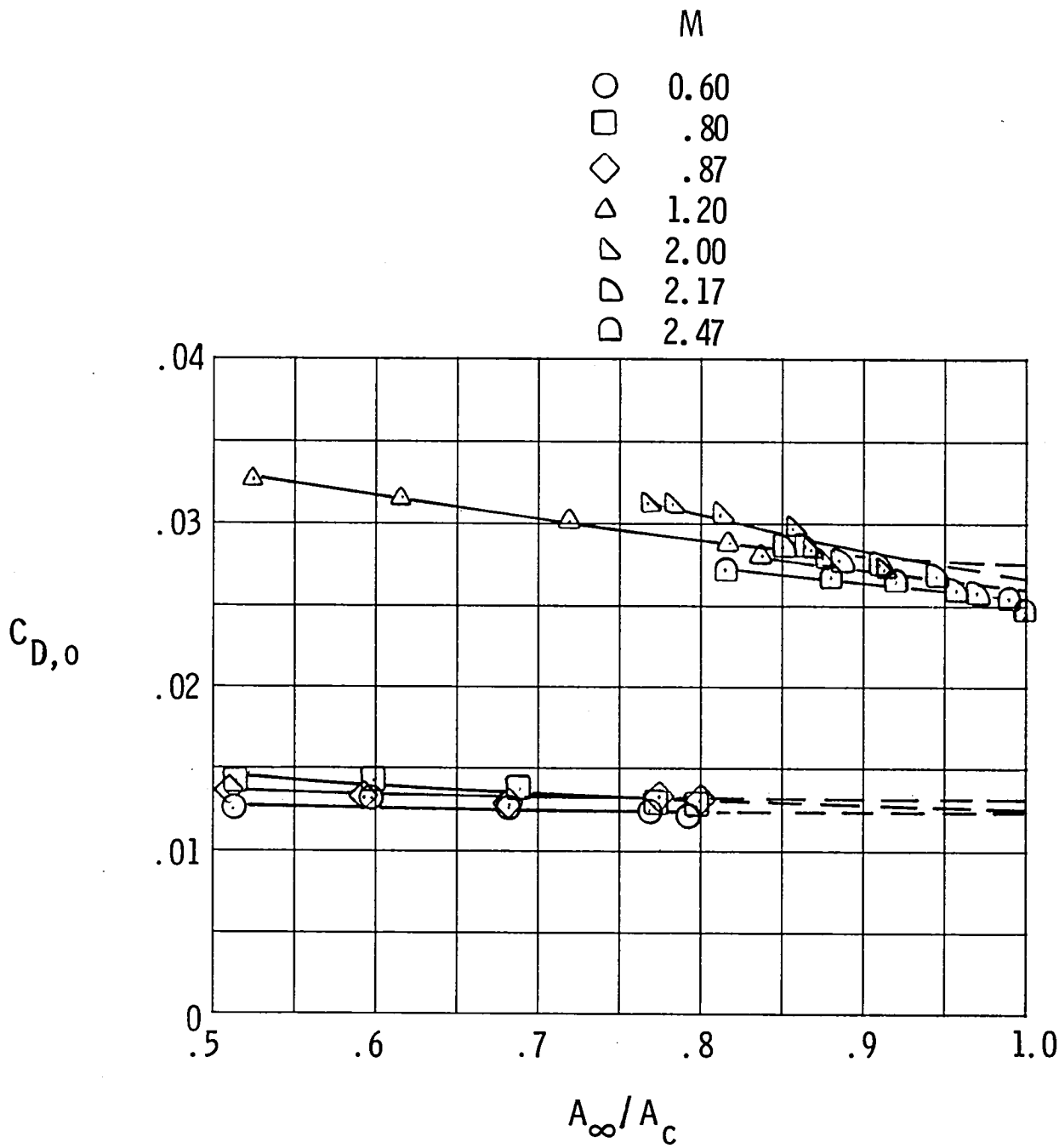

Figure 13.- Effect of capture ratio variation on drag coefficient for WBC. $C_L = 0$.

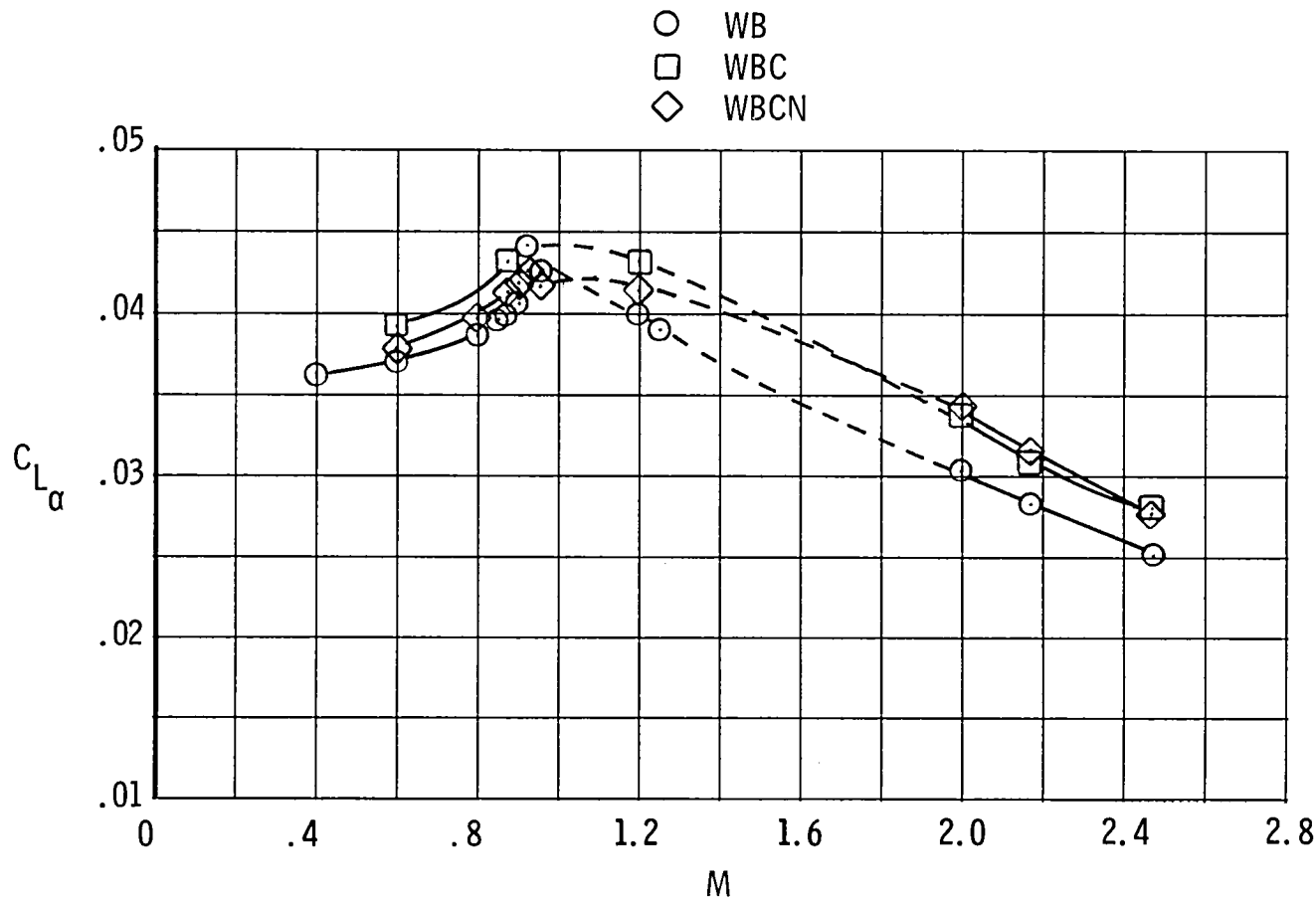

Figure 14.- Lift-curve slope characteristics. $A_\infty/A_c = 1.0$; $\delta_c = 0°$.

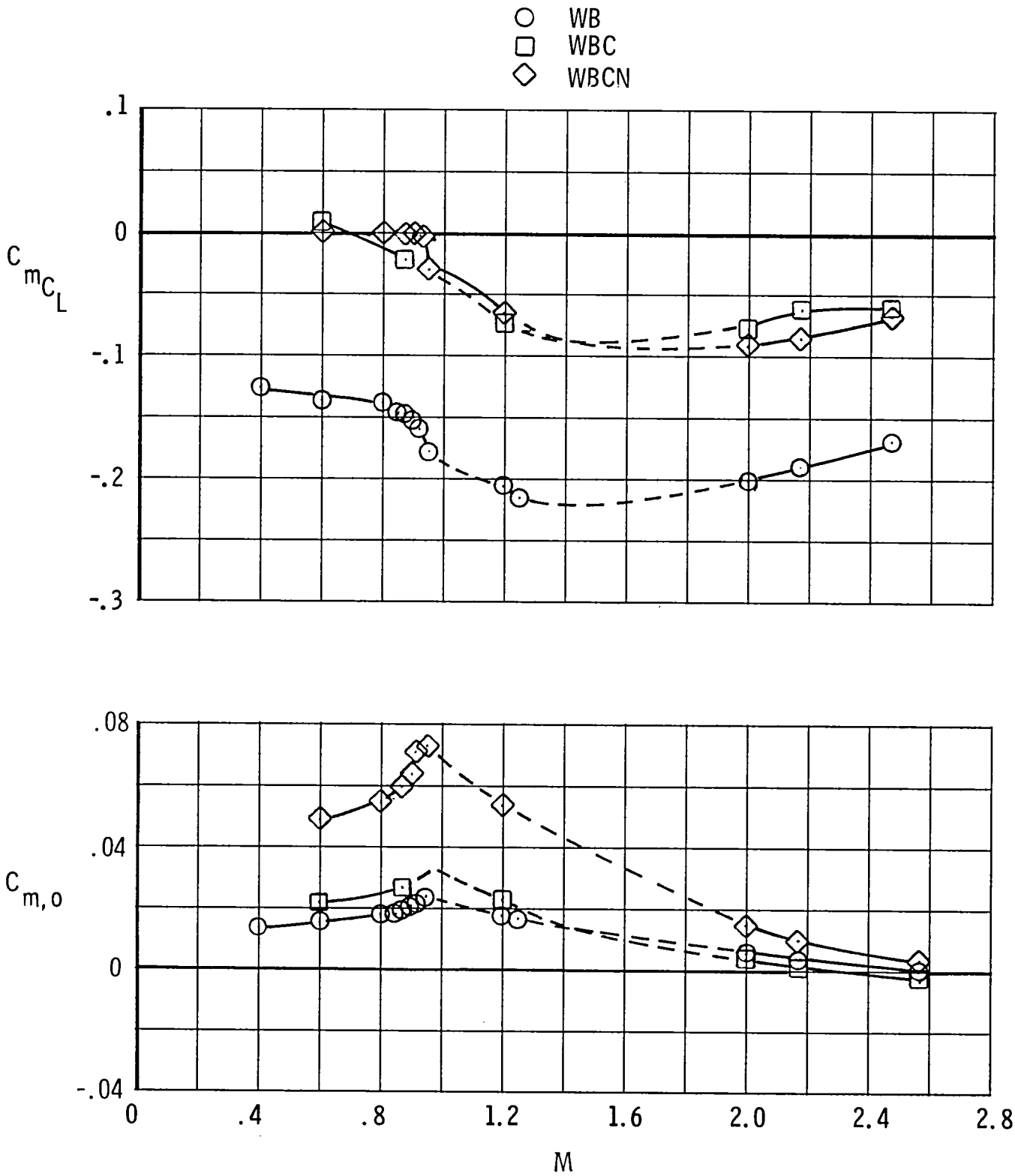

Figure 15.- Longitudinal stability characteristics. $A_\infty/A_c = 1.0$; $\delta_c = 0°$.

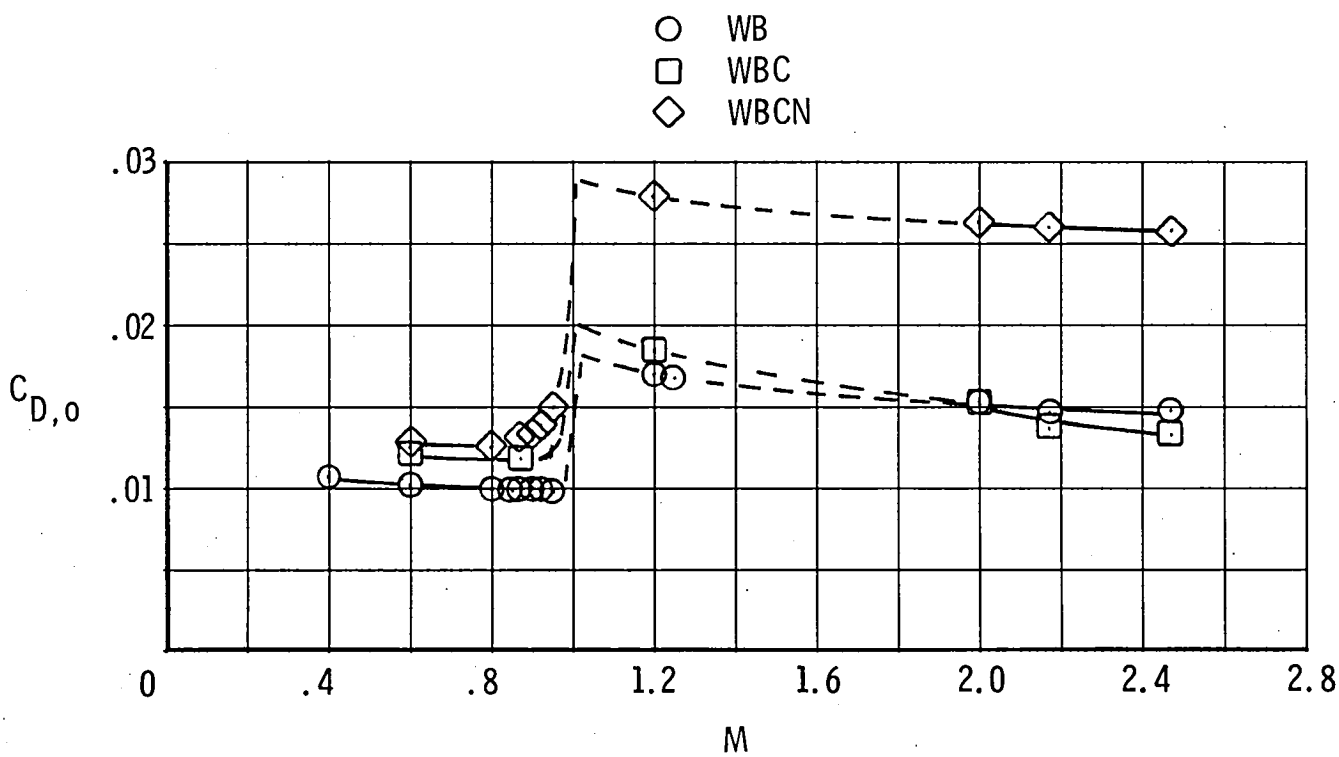

Figure 16.- Zero-lift drag characteristics. $A_\infty/A_c = 1.0$; $\delta_c = 0°$.

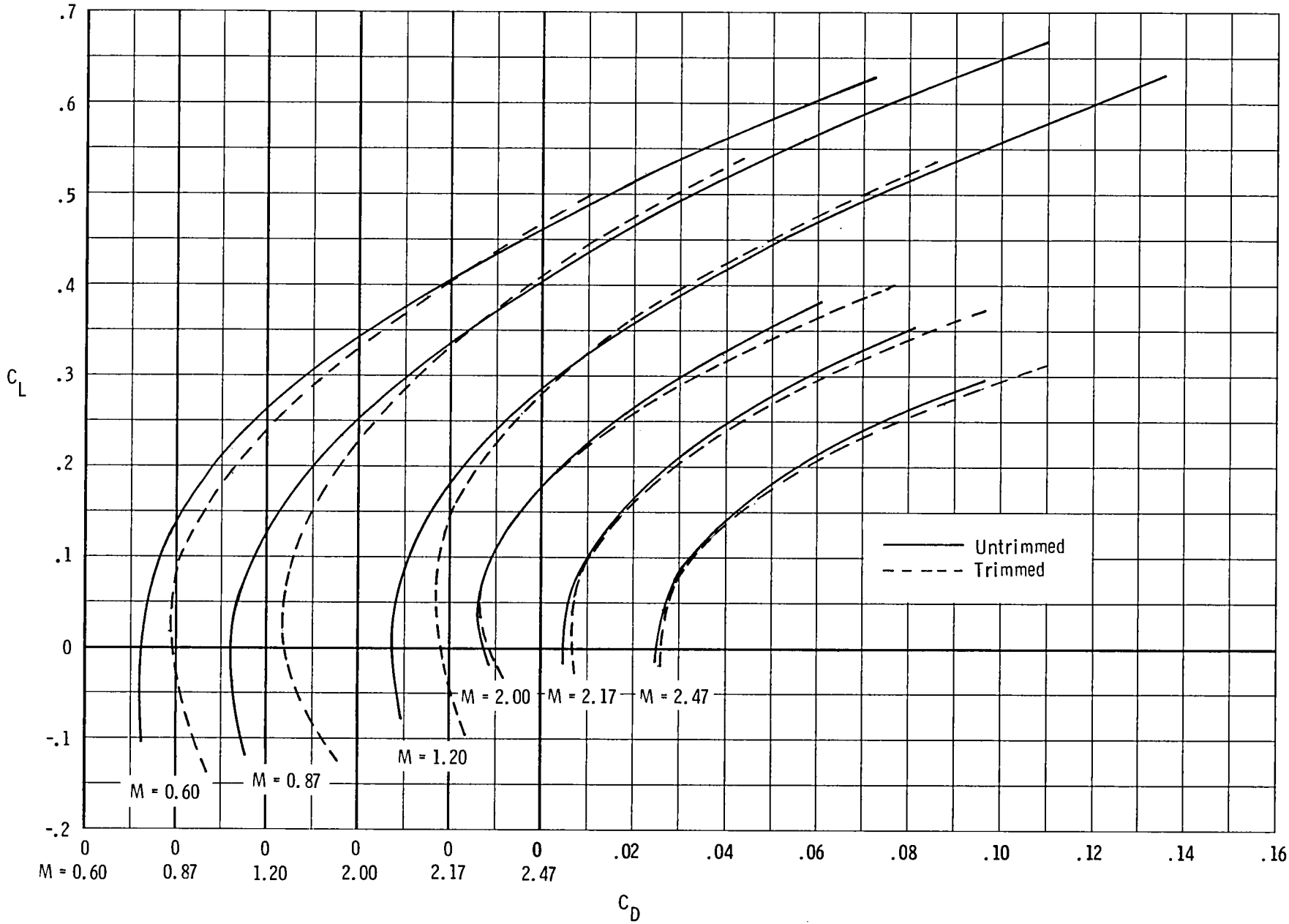

Figure 17.- Comparison of untrimmed and trimmed drag polars for WBCN. $A_\infty/A_c = 1.0$.

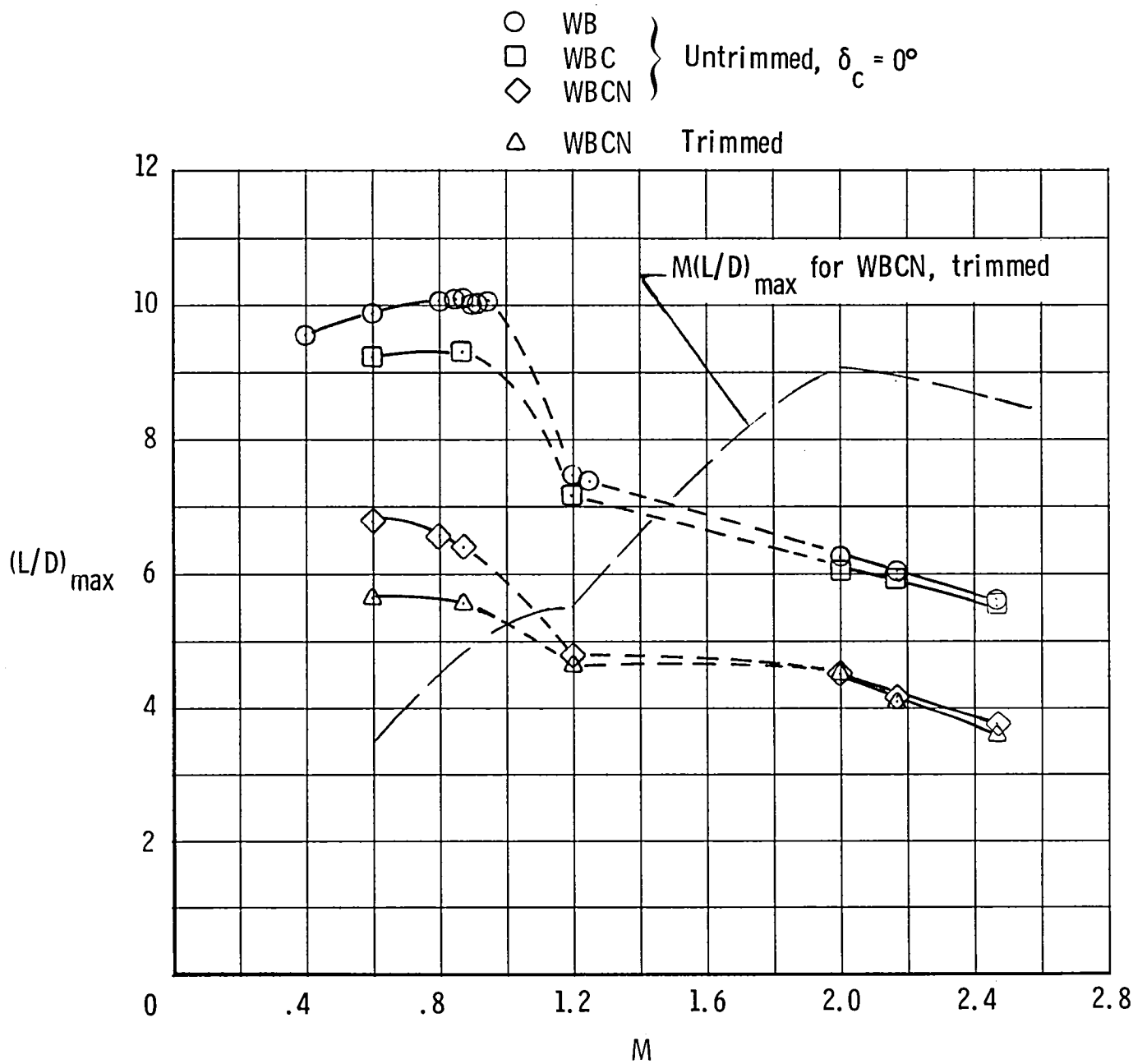

Figure 18.- Maximum lift-drag ratio characteristics. $A_\infty/A_c = 1.0$.

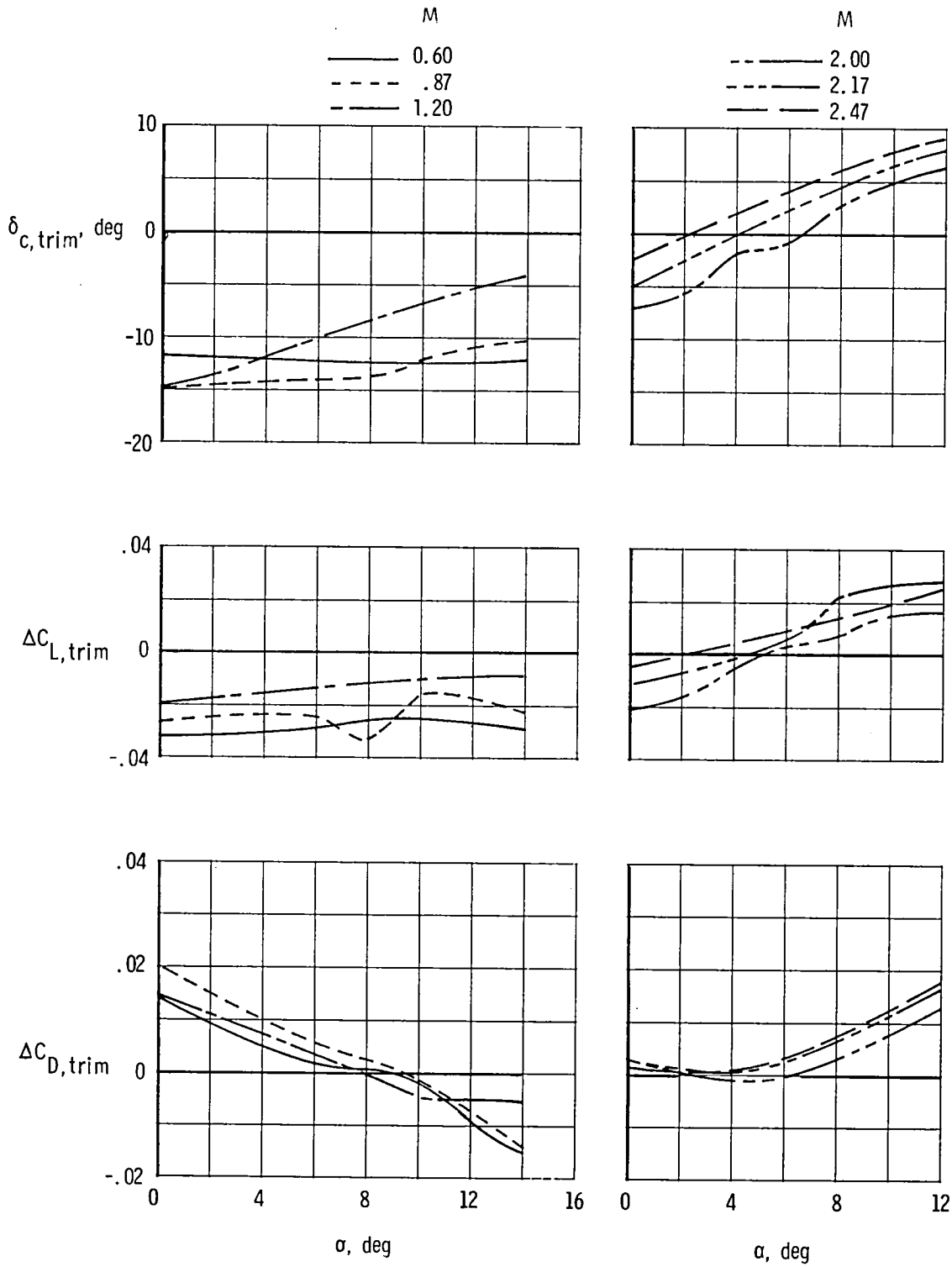

Figure 19.- Canard deflection required for trim and trim drag increments. A_∞/A_c = 1.0.

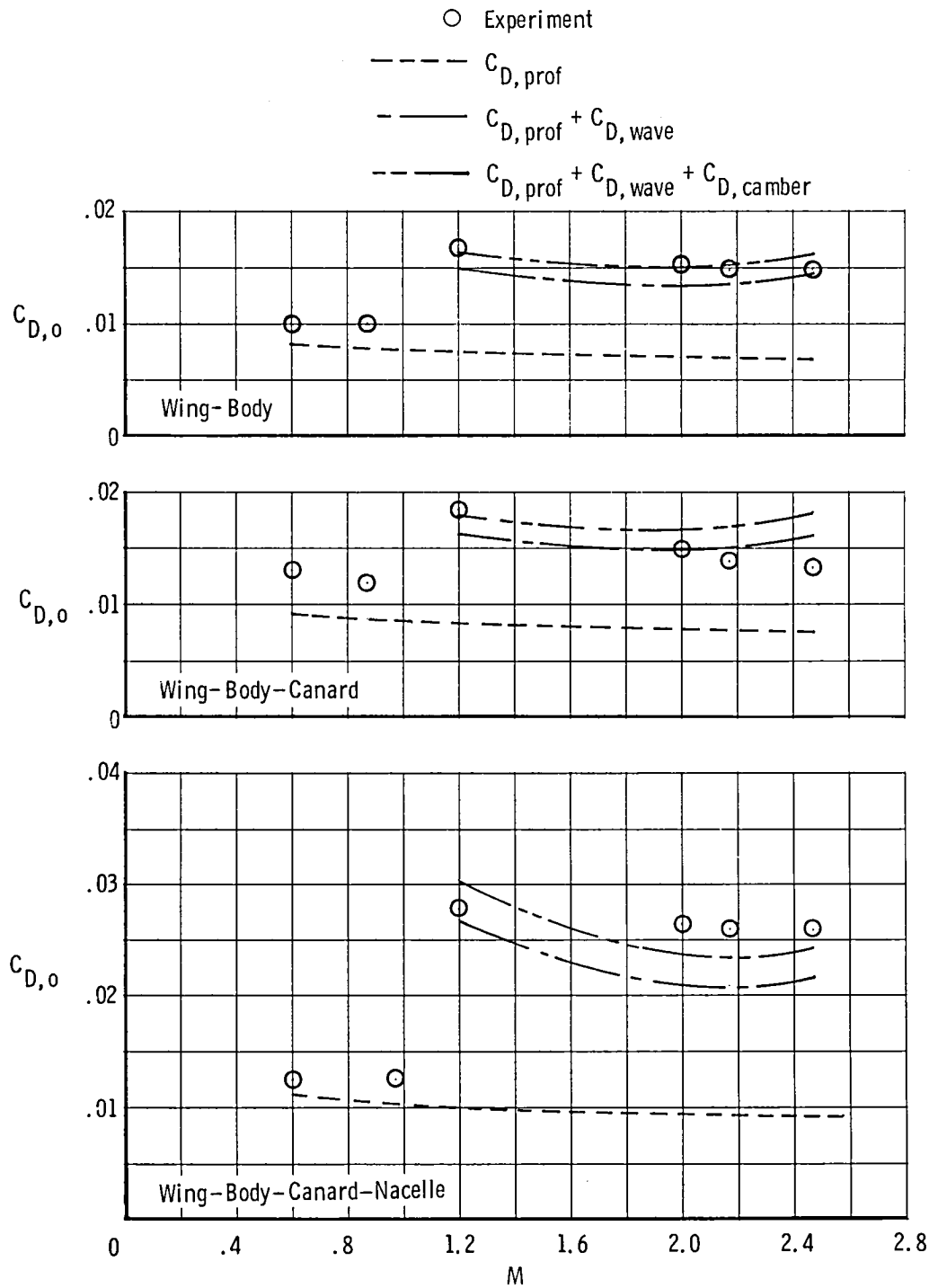

Figure 20.- Component zero-lift drag characteristics. $A_\infty/A_c = 1.0$; $\delta_c = 0°$.

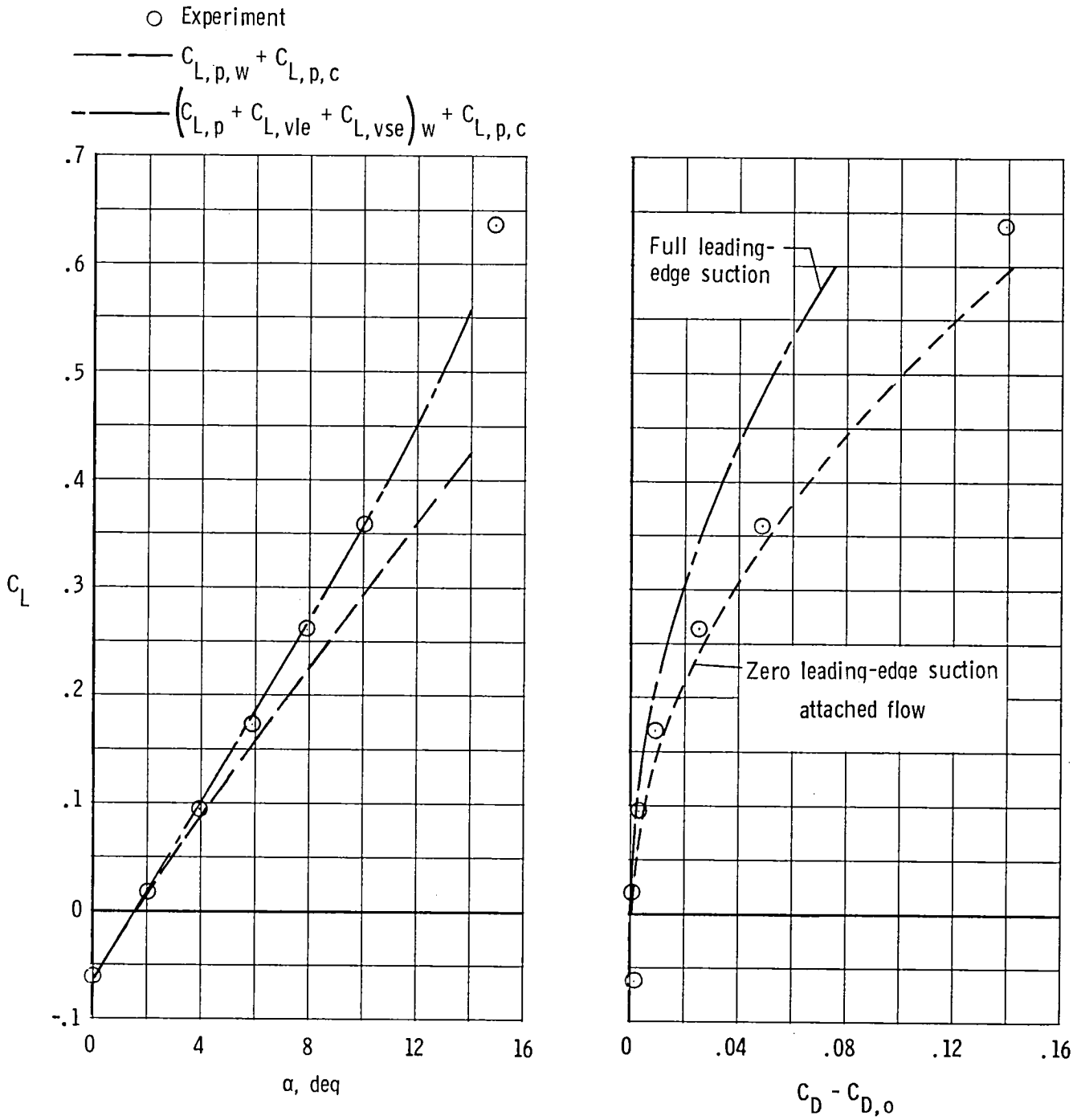

(a) M = 0.60.

Figure 21.- Comparison of experimental and theoretical wing-body-canard aerodynamic characteristics for nacelles off. $\delta_c = 0°$.

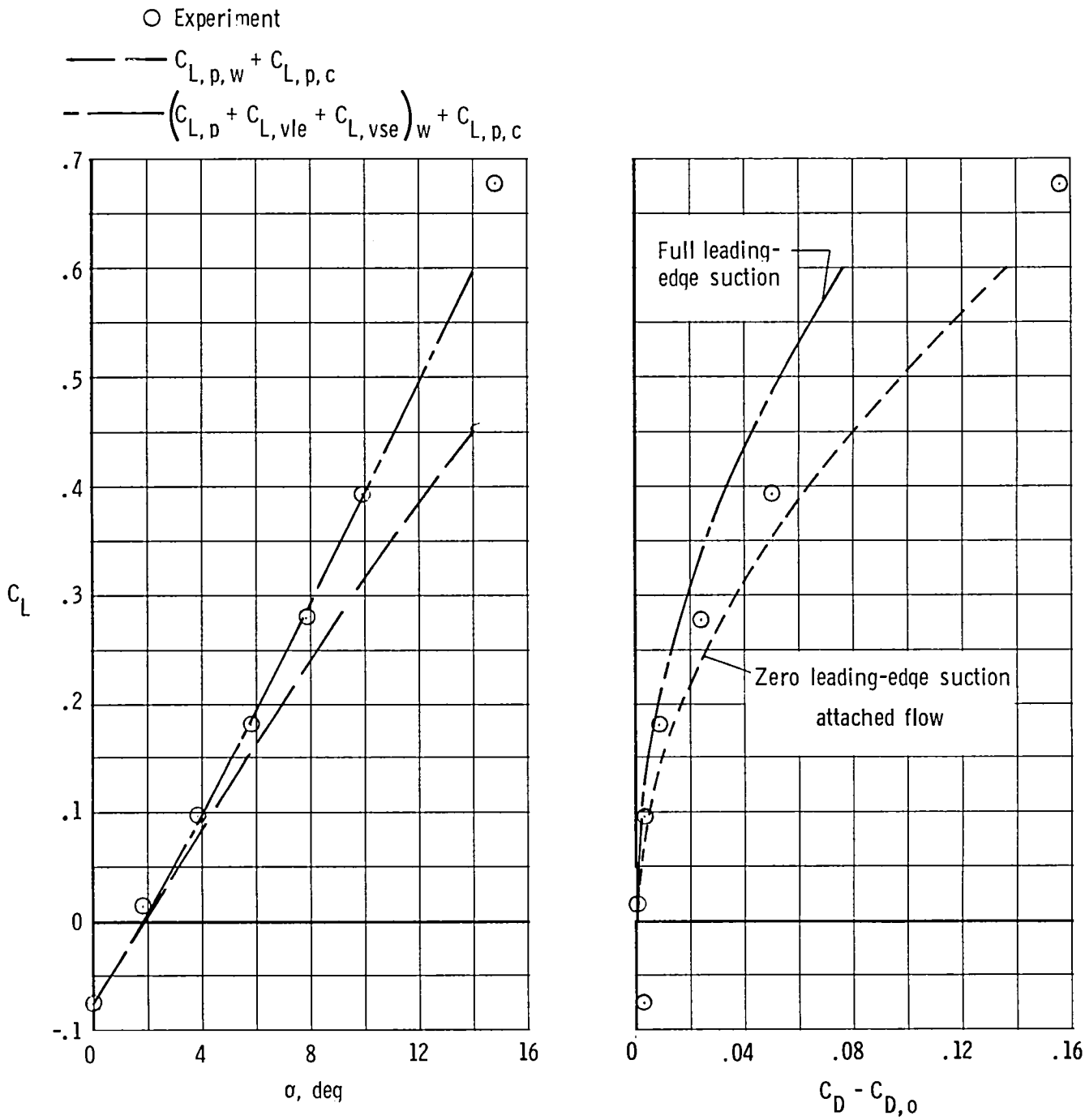

(b) M = 0.87.

Figure 21.- Concluded.

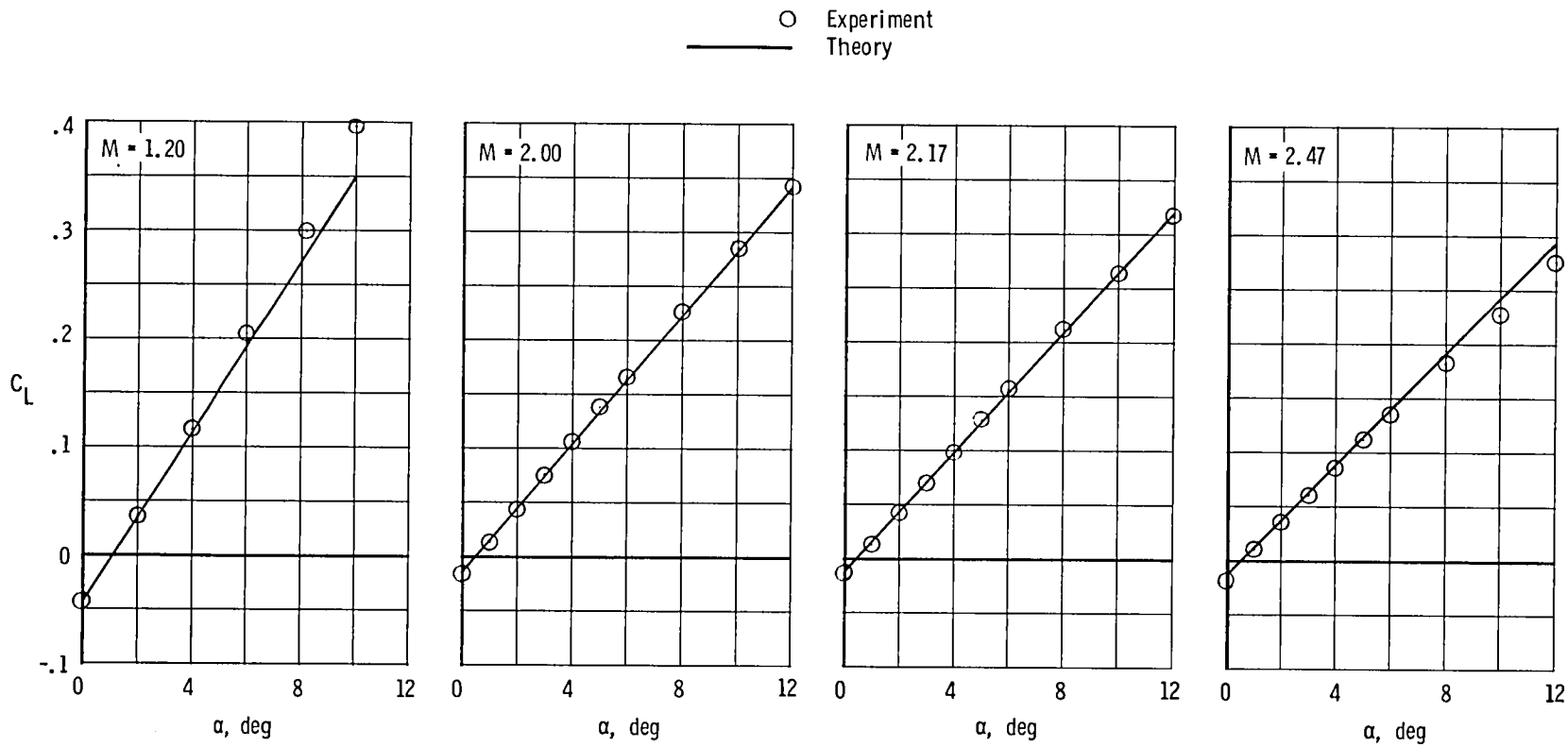

(a) WB.

Figure 22.- Comparison of experimental and theoretical lift characteristics.

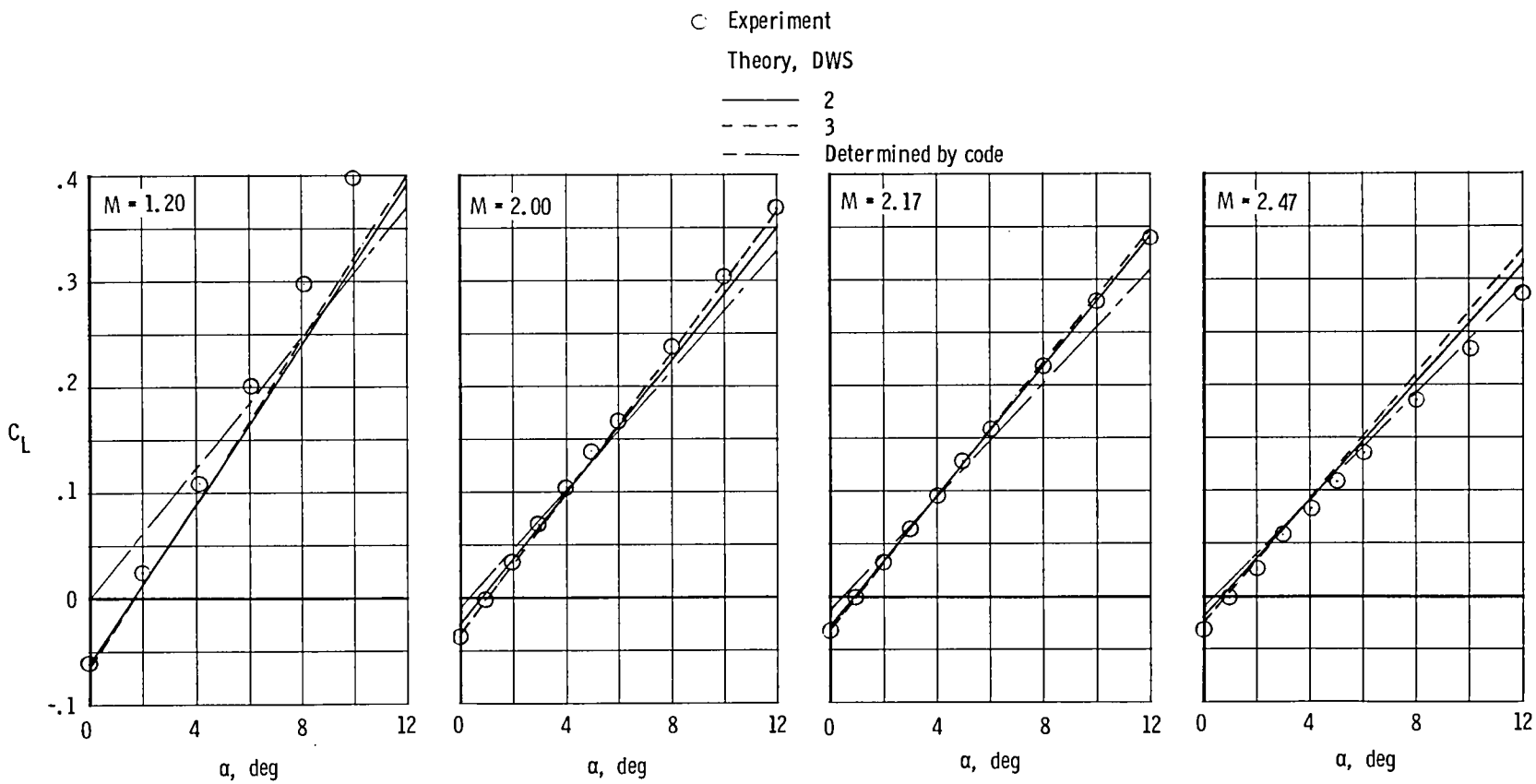

(b) WBC; $\delta_c = -5°$.

Figure 22.- Continued.

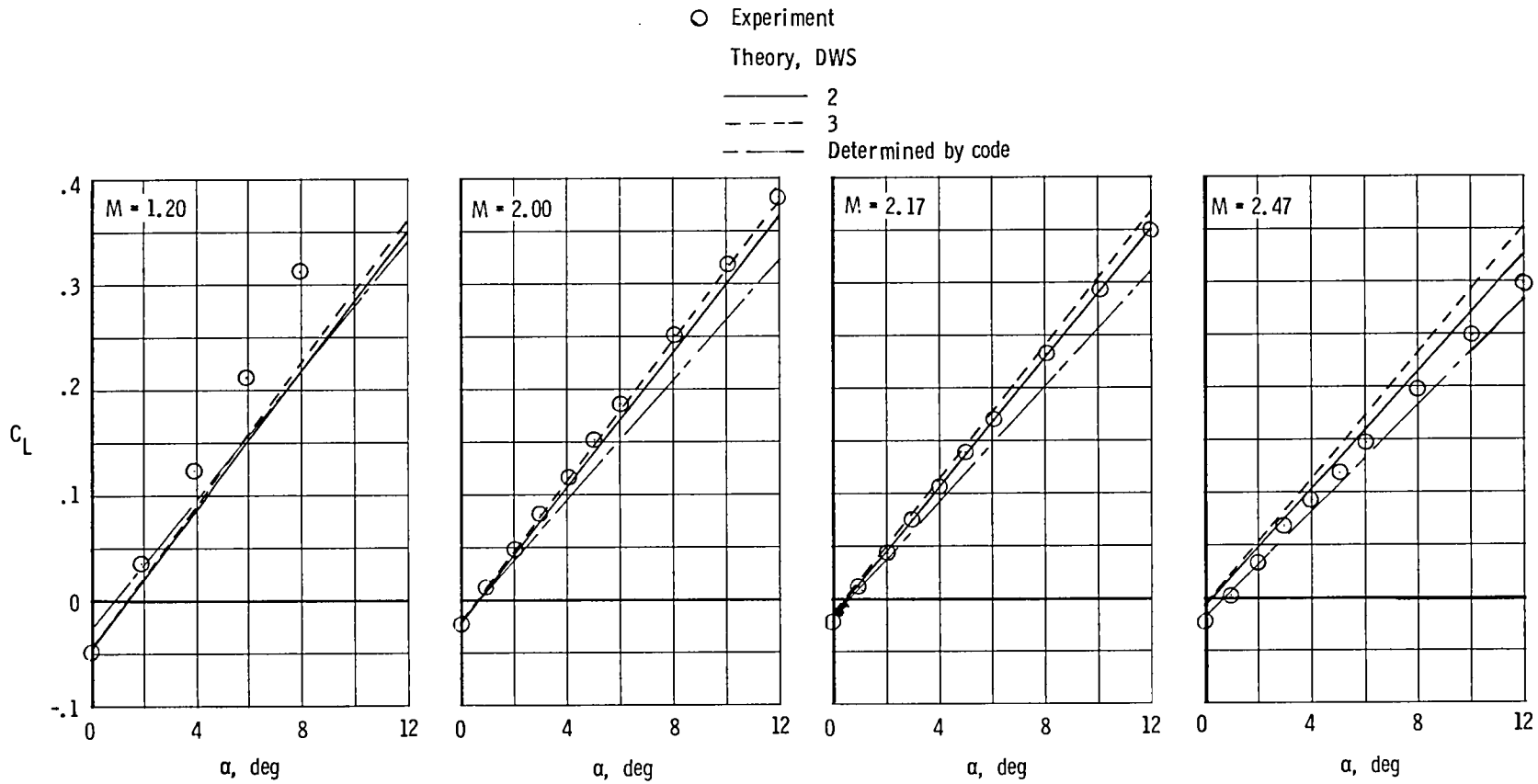

(c) WBC; $\delta_c = 0°$.

Figure 22.- Continued.

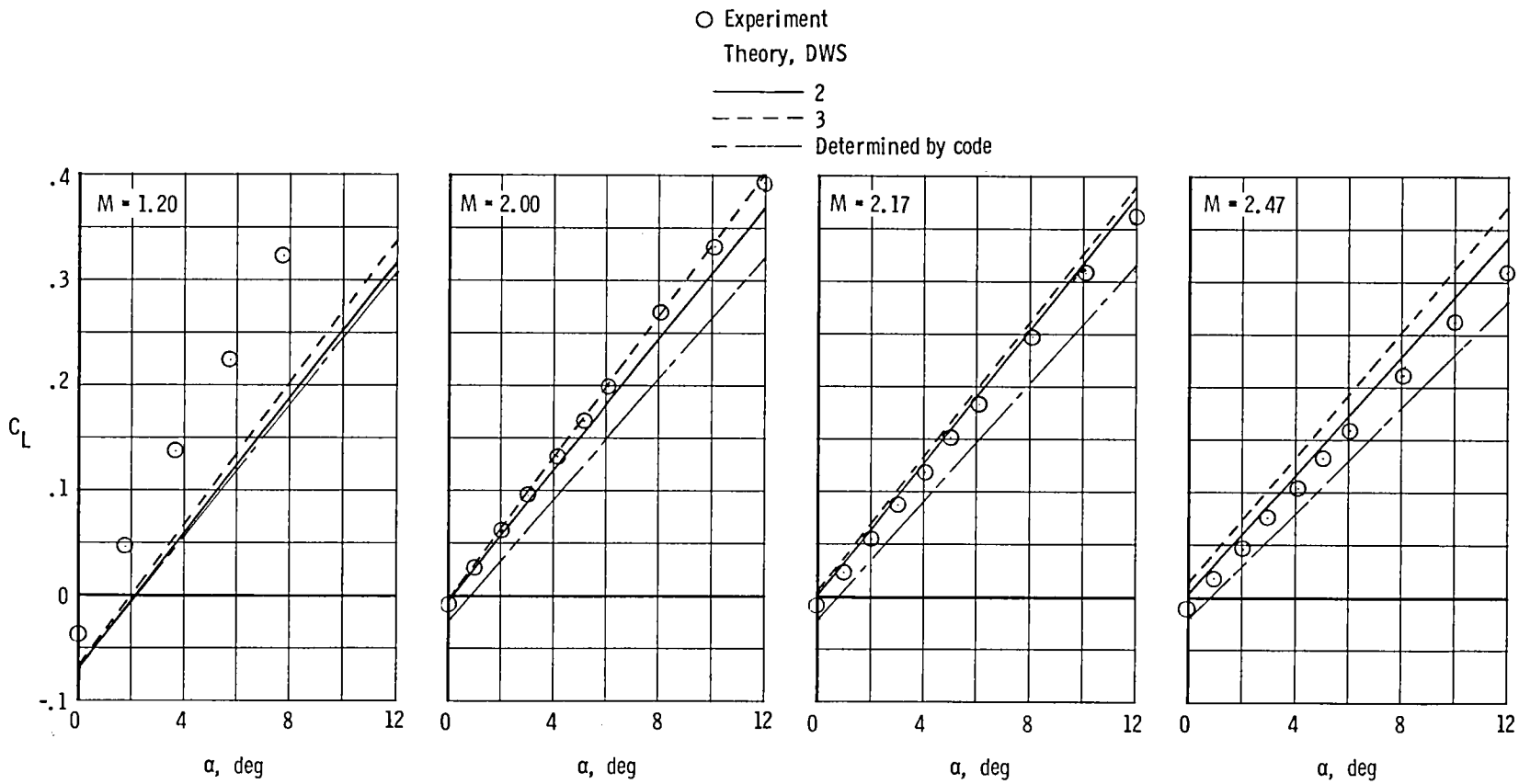

(d) WBC; $\delta_c = 5°$.

Figure 22.- Continued.

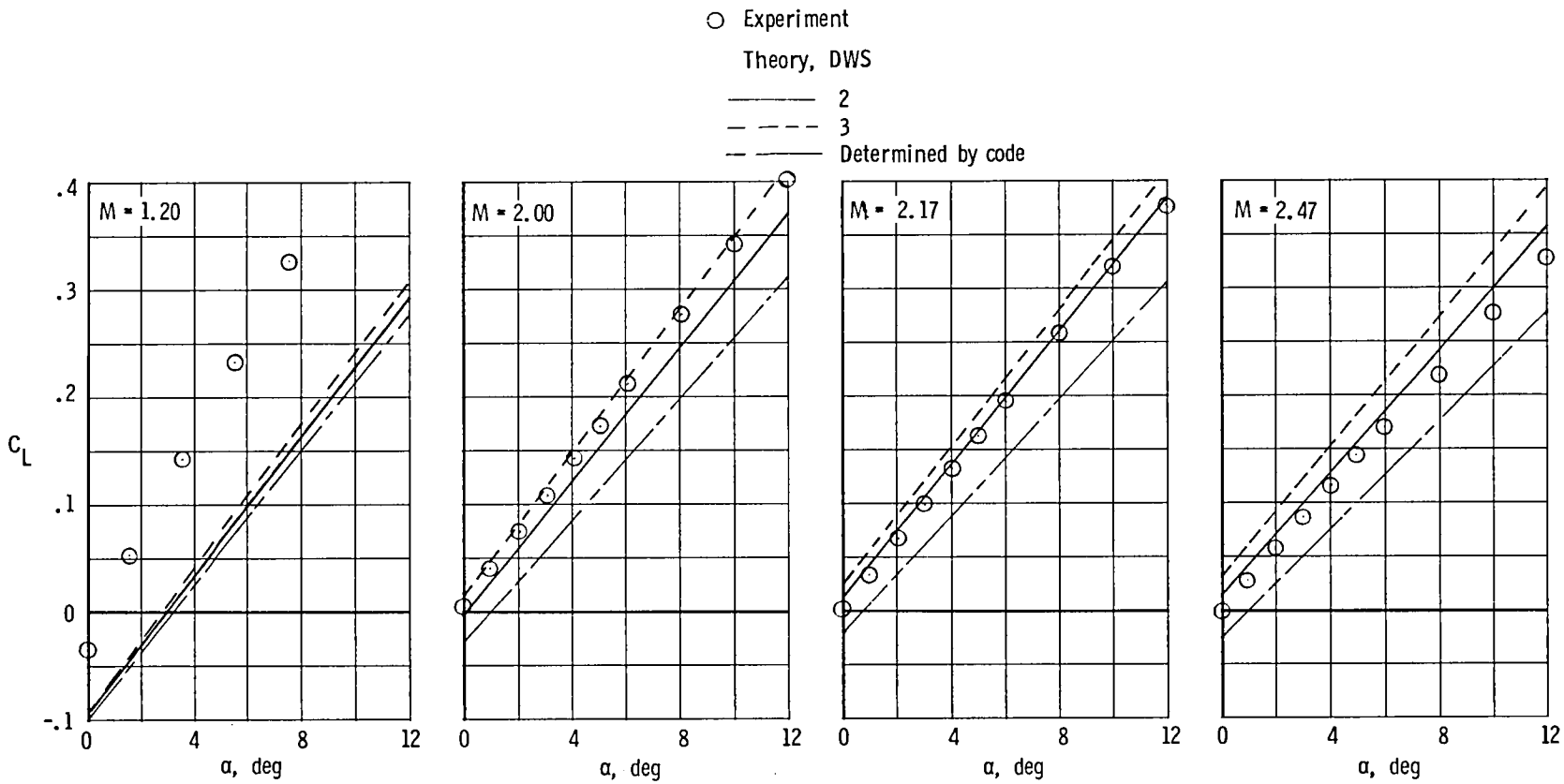

(e) WBC; $\delta_c = 10°$.

Figure 22.- Continued.

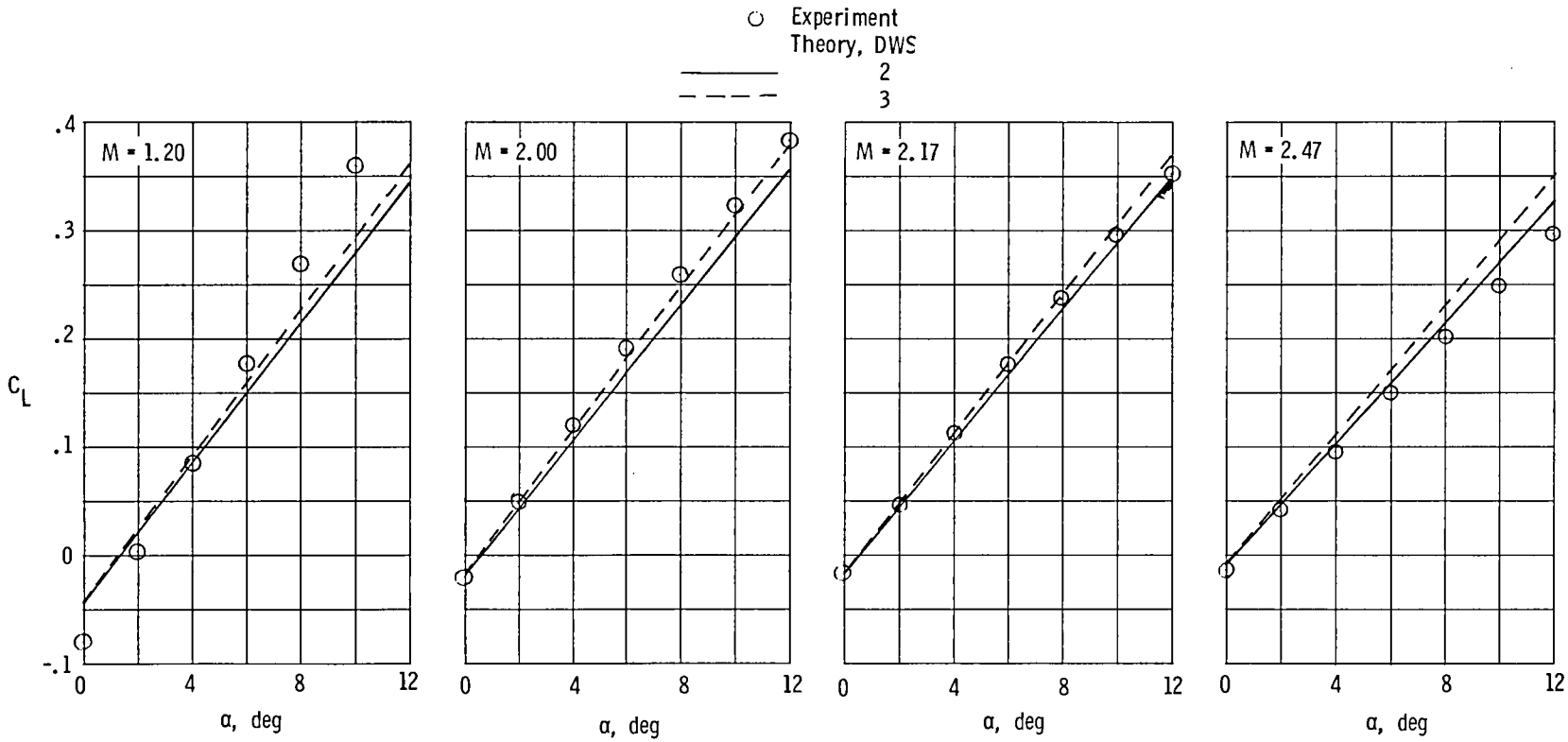

(f) WBCN; $\delta_c = 0°$; $A_\infty/A_c = 1.00$.

Figure 22.- Concluded.

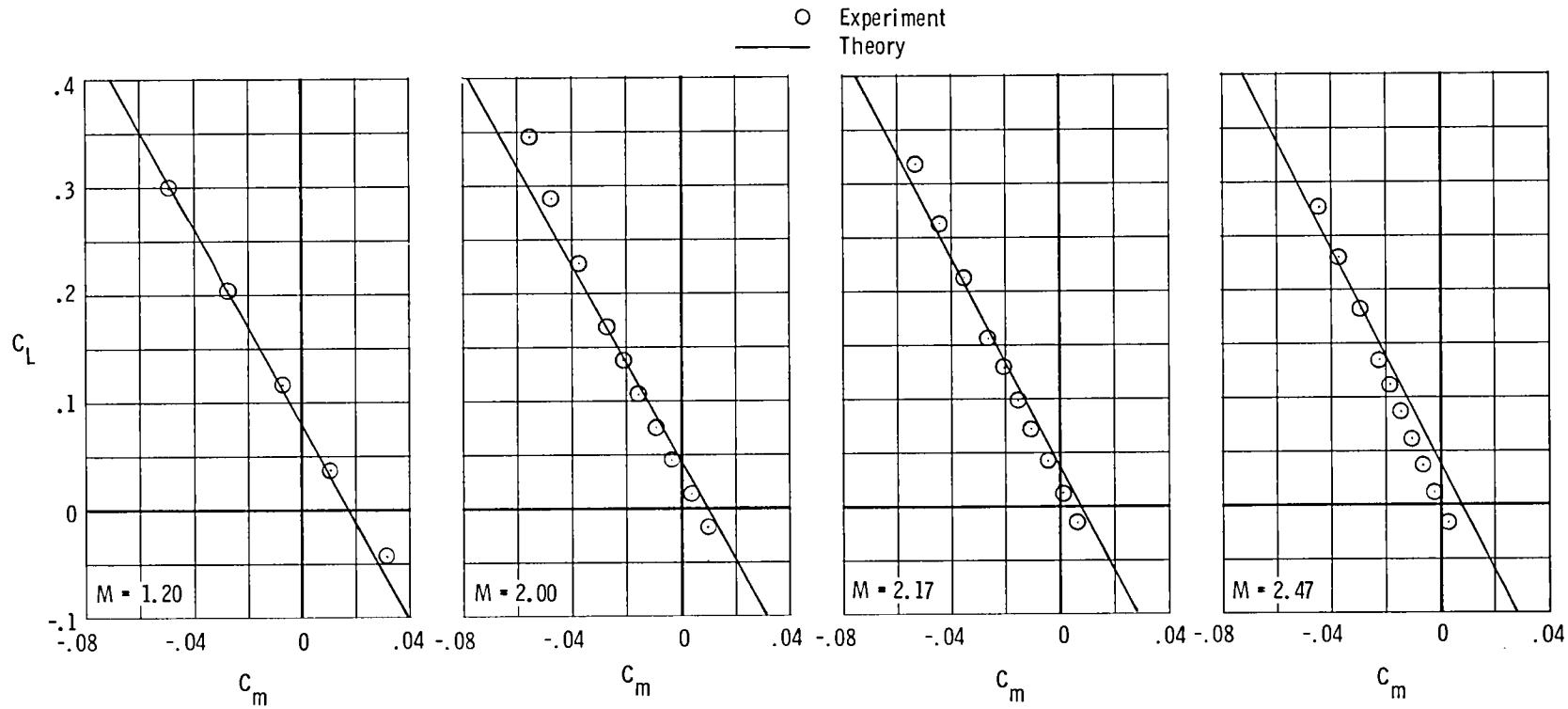

(a) WB.

Figure 23.- Comparison of experimental and theoretical pitch characteristics.

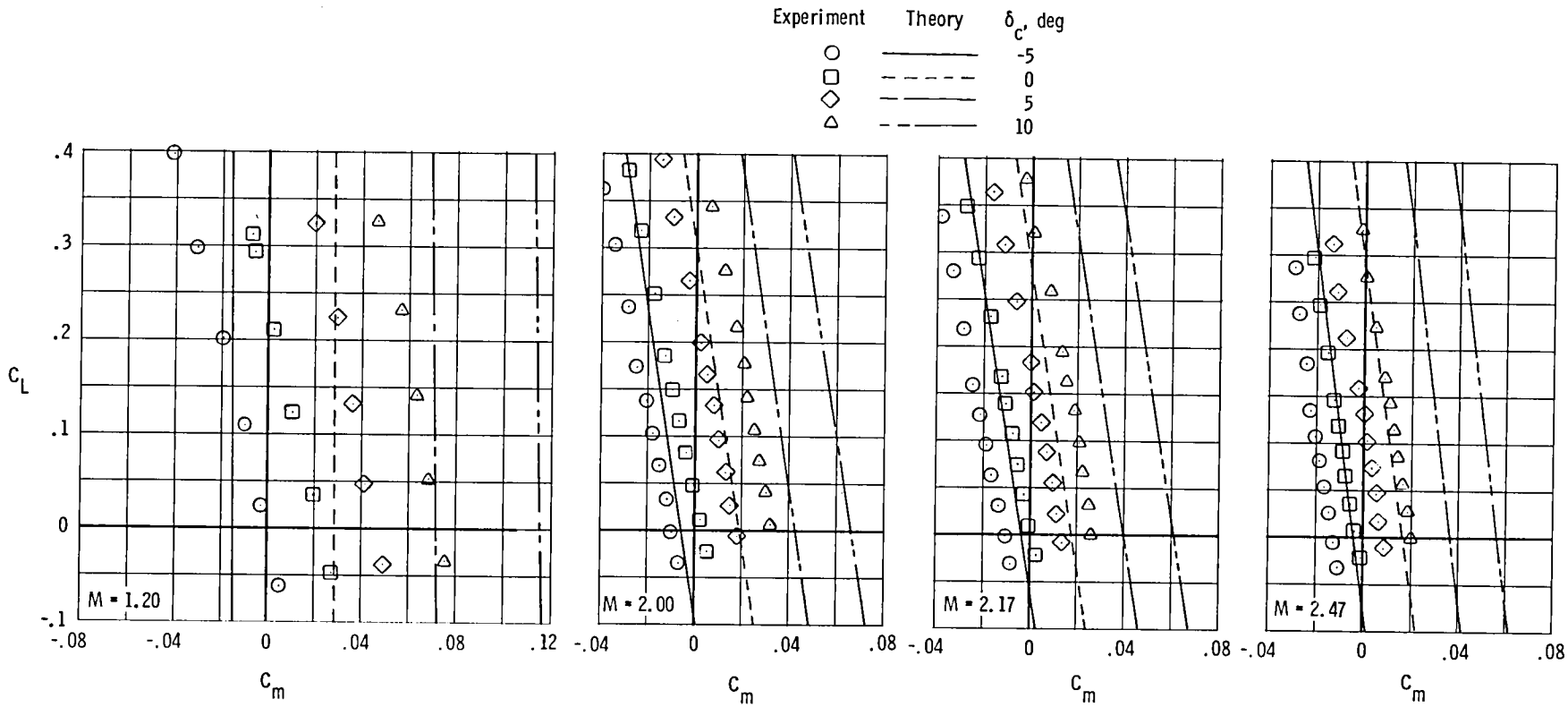

(b) WBC; δ_c = -5° to 10°.

Figure 23.- Continued.

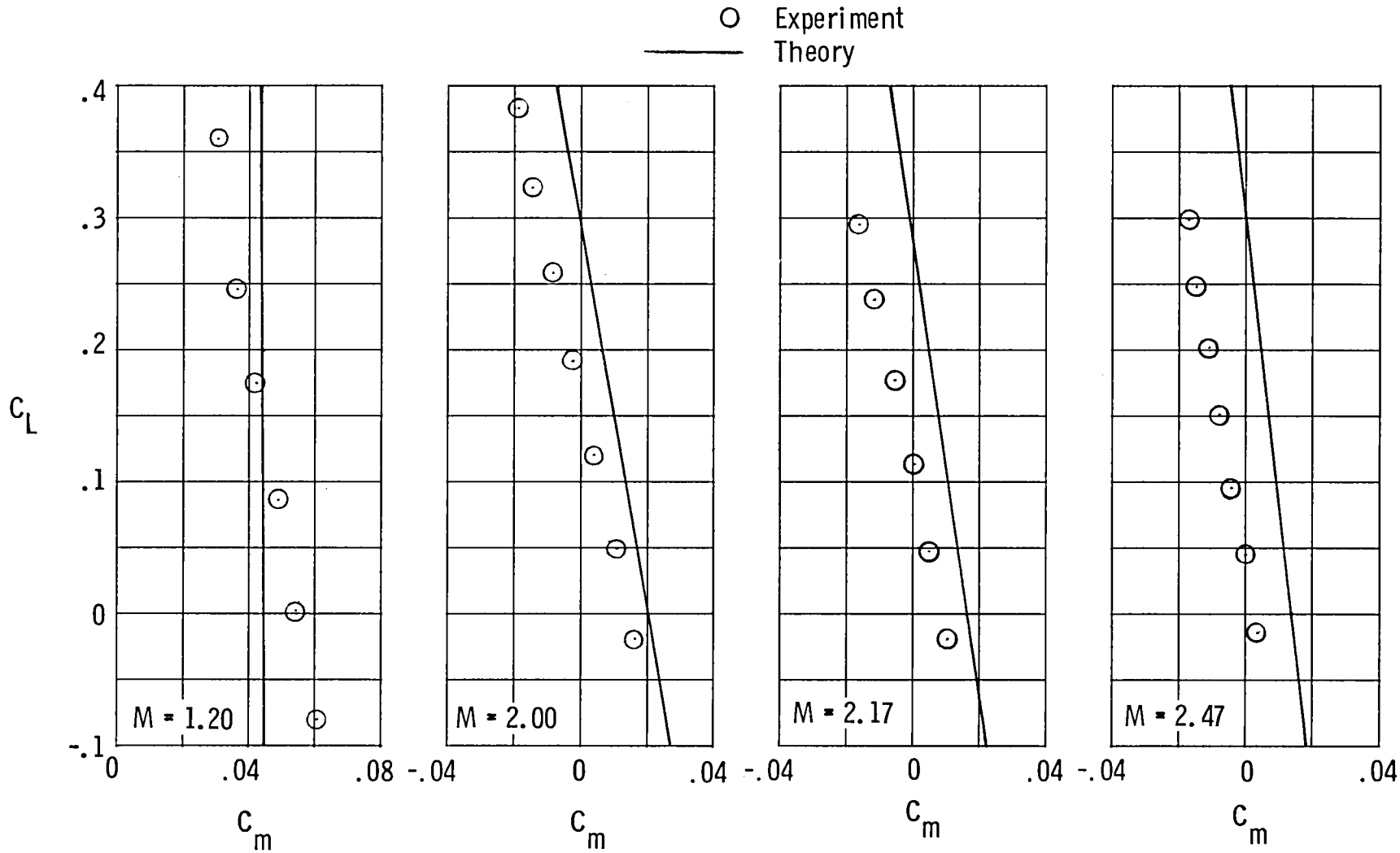

(c) WBCN; $\delta_c = 0°$; $A_\infty/A_c = 1.00$.

Figure 23.- Concluded.

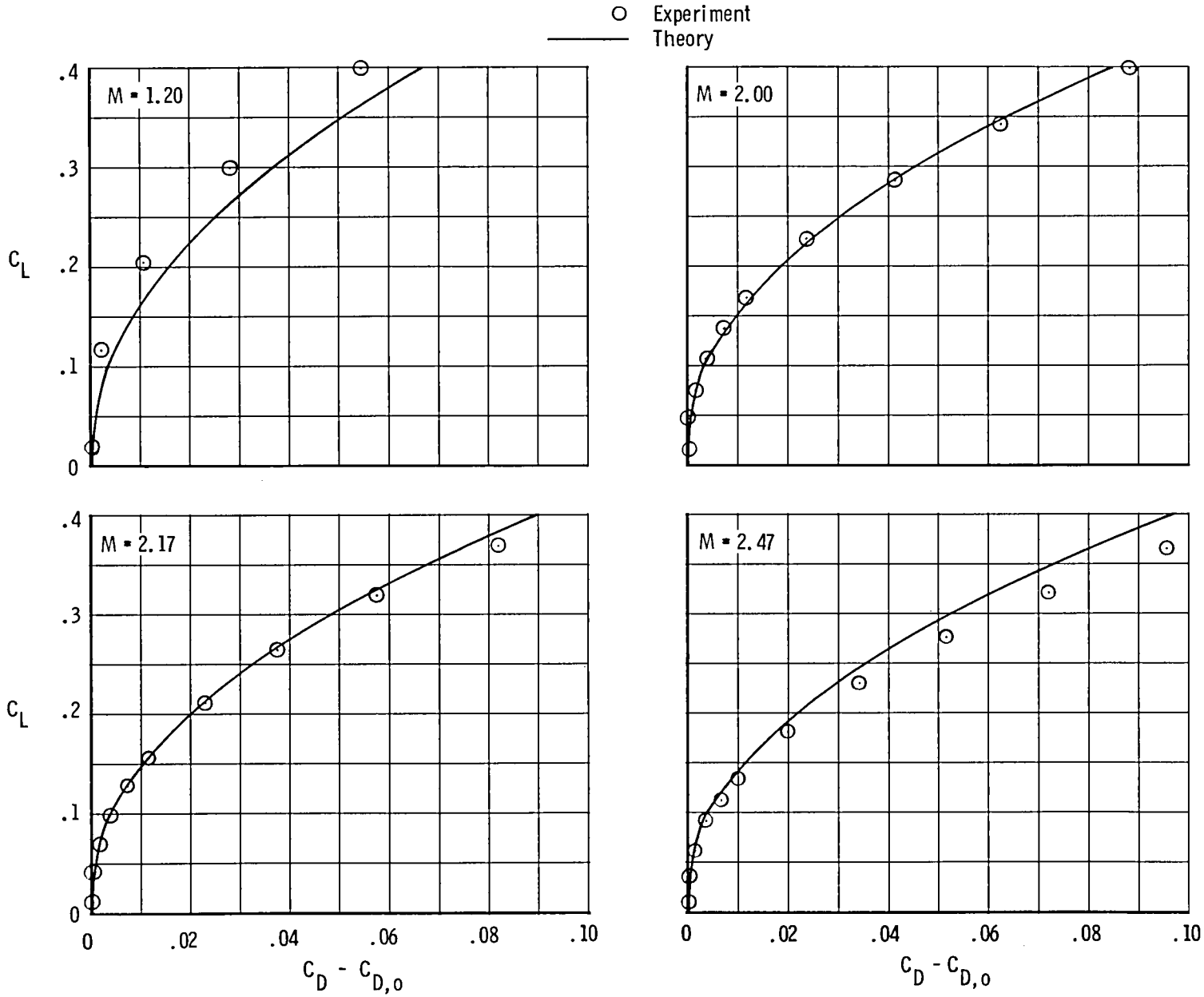

(a) WB.

Figure 24.- Comparison of experimental and theoretical drag-due-to-lift characteristics.

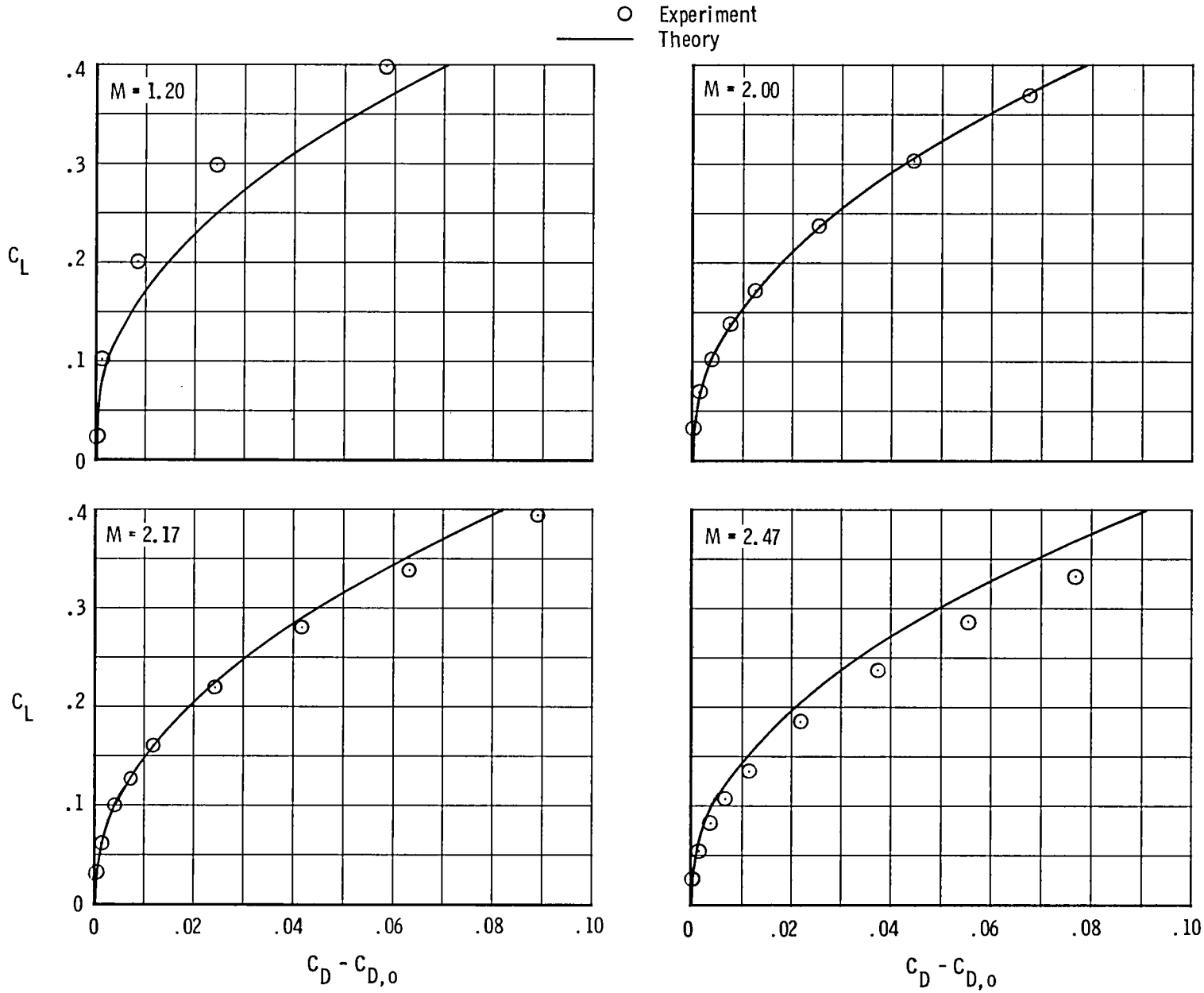

(b) WBC; $\delta_c = -5°$.

Figure 24.- Continued.

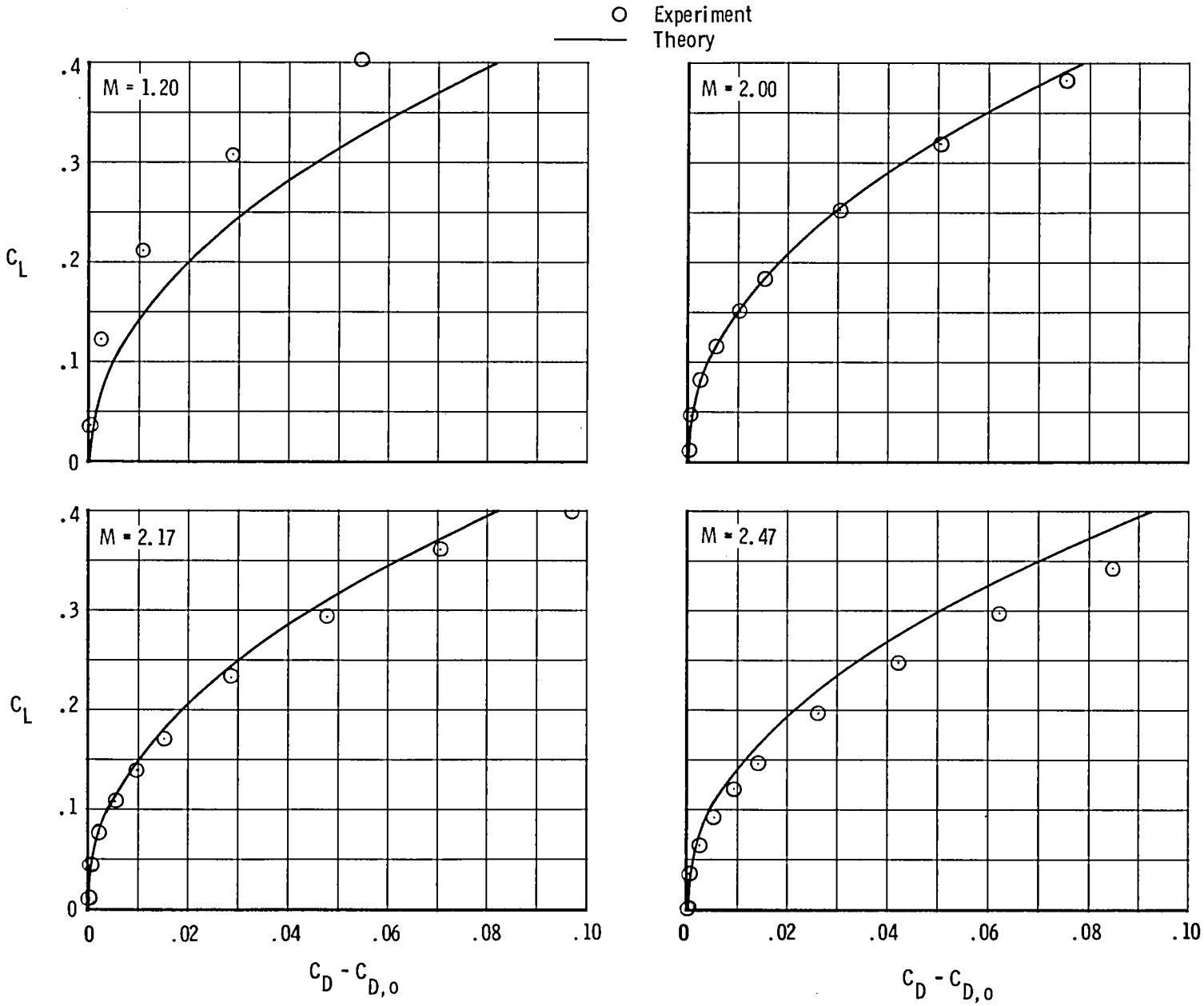

(c) WBC; $\delta_c = 0°$.

Figure 24.- Continued.

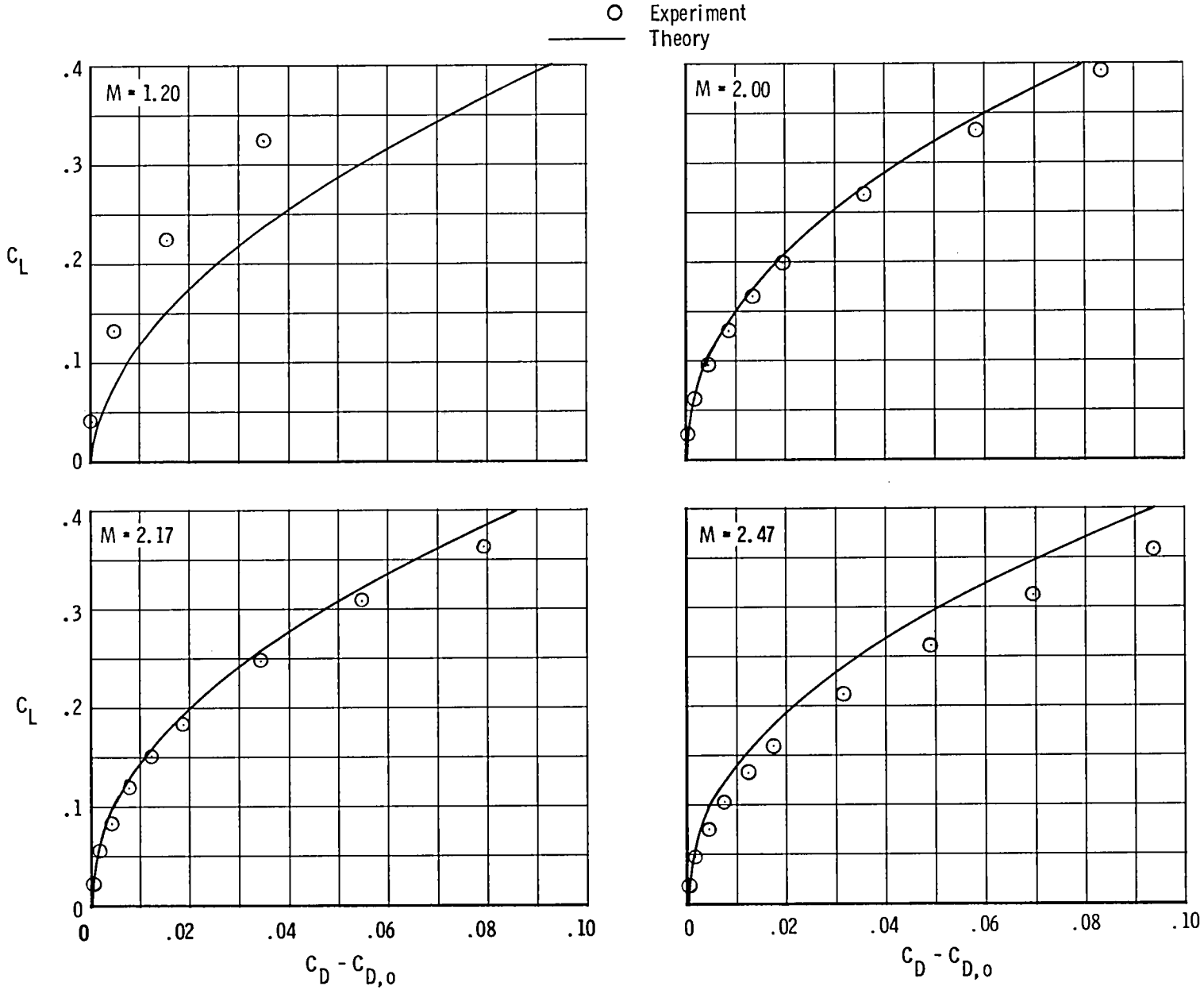

(d) WBC; $\delta_c = 5°$.

Figure 24.- Continued.

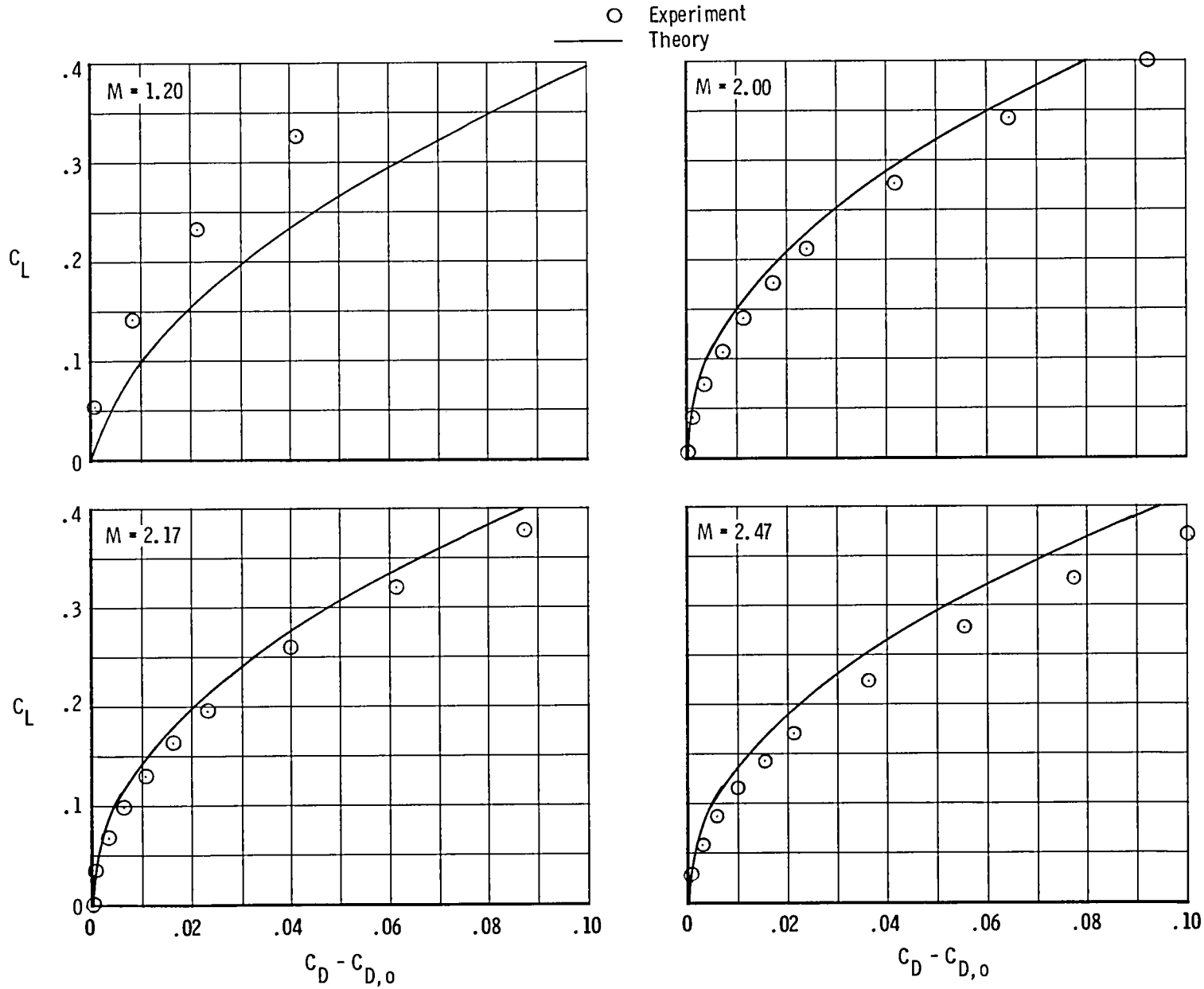

(e) WBC; $\delta_c = 10°$.

Figure 24.- Continued.

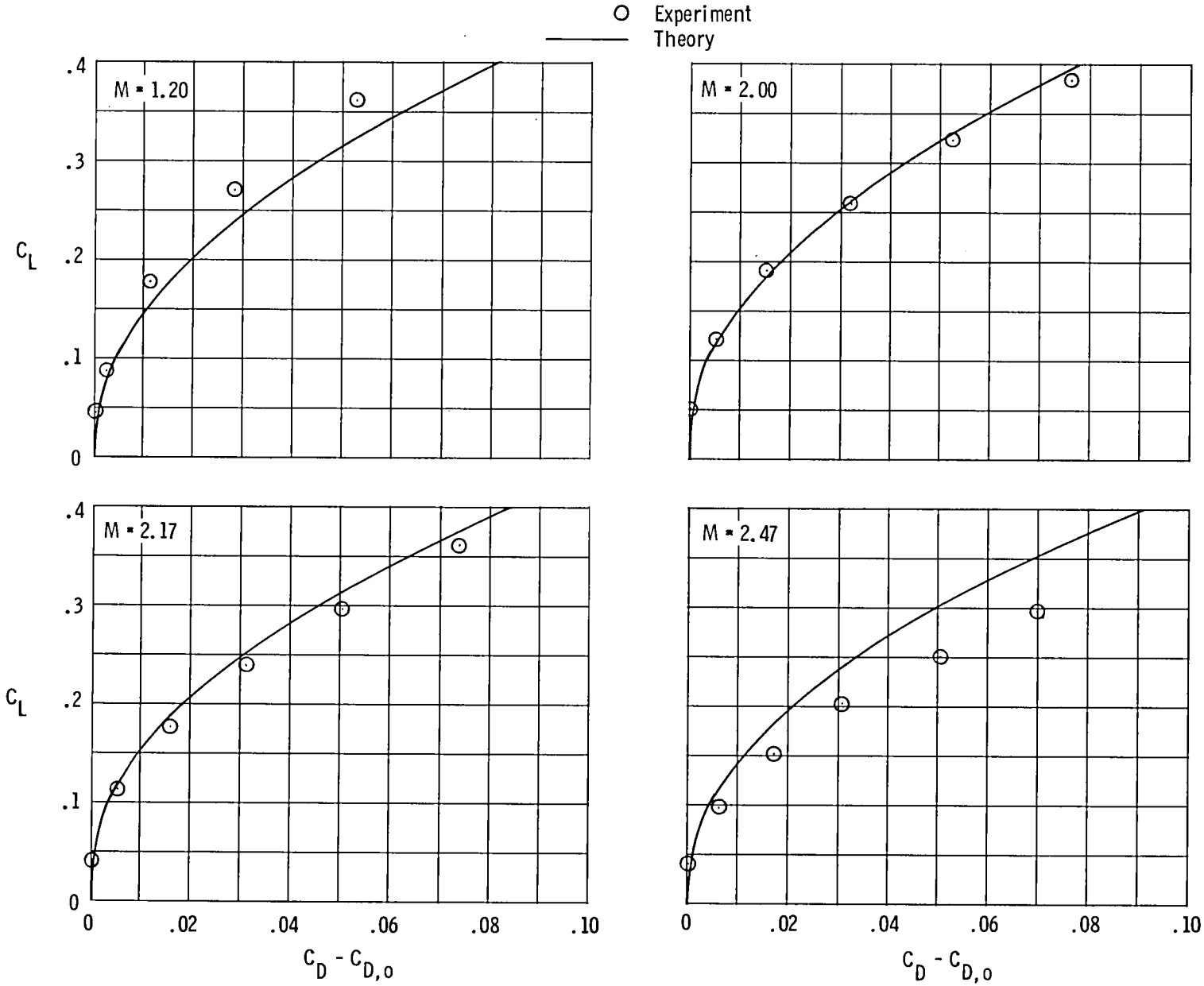

(f) WBCN; $\delta_c = 0°$; $A_\infty/A_c = 1.0$.

Figure 24.- Concluded.

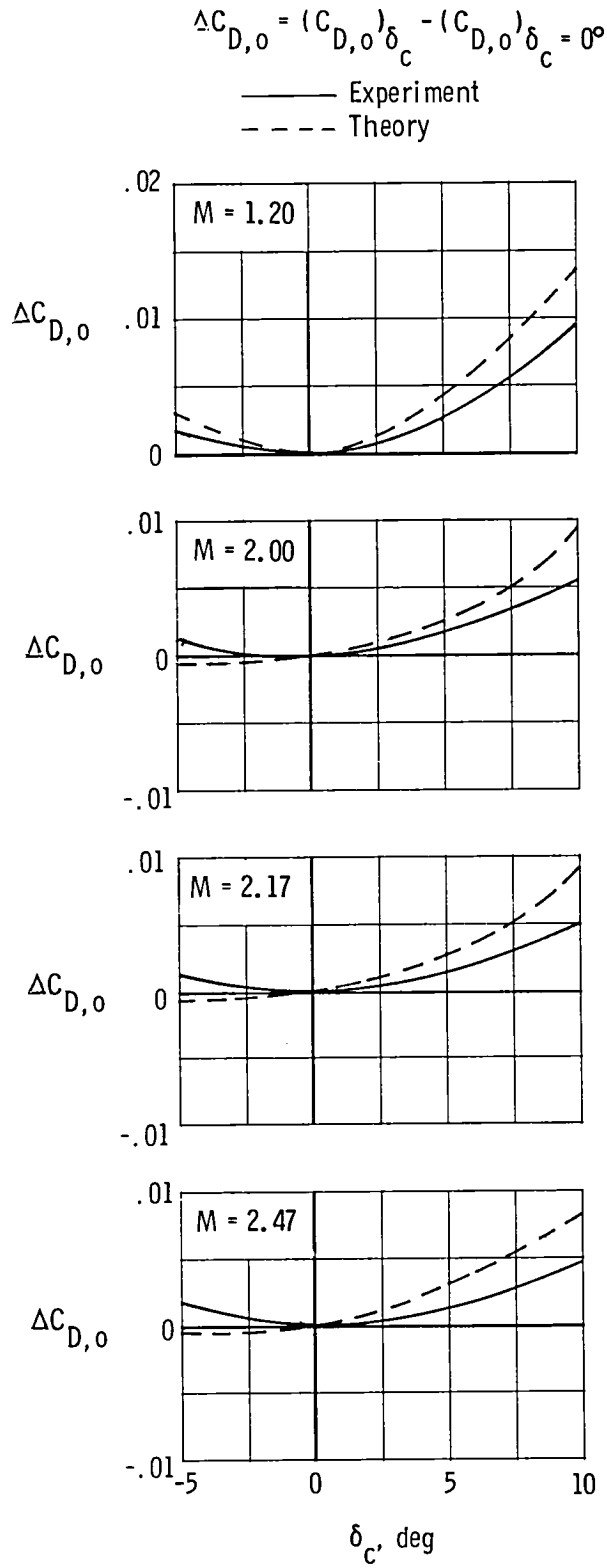

Figure 25.- Comparison of experimental and theoretical incremental drag due to canard deflection.

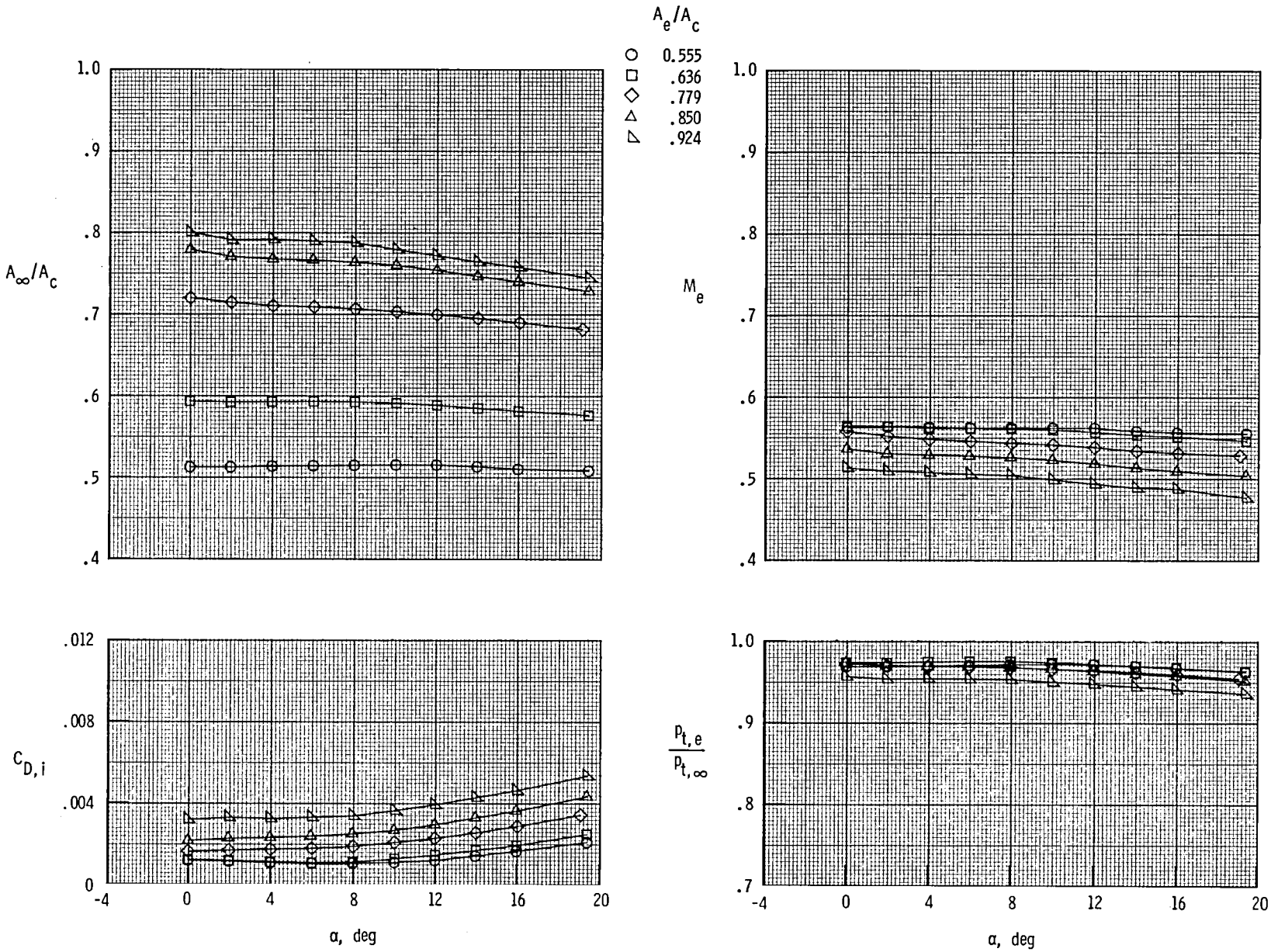

(a) M = 0.60.

Figure 26.- Flow-through nacelle internal flow characteristics for inlet spike designed for $M_{in} < 1.50$.

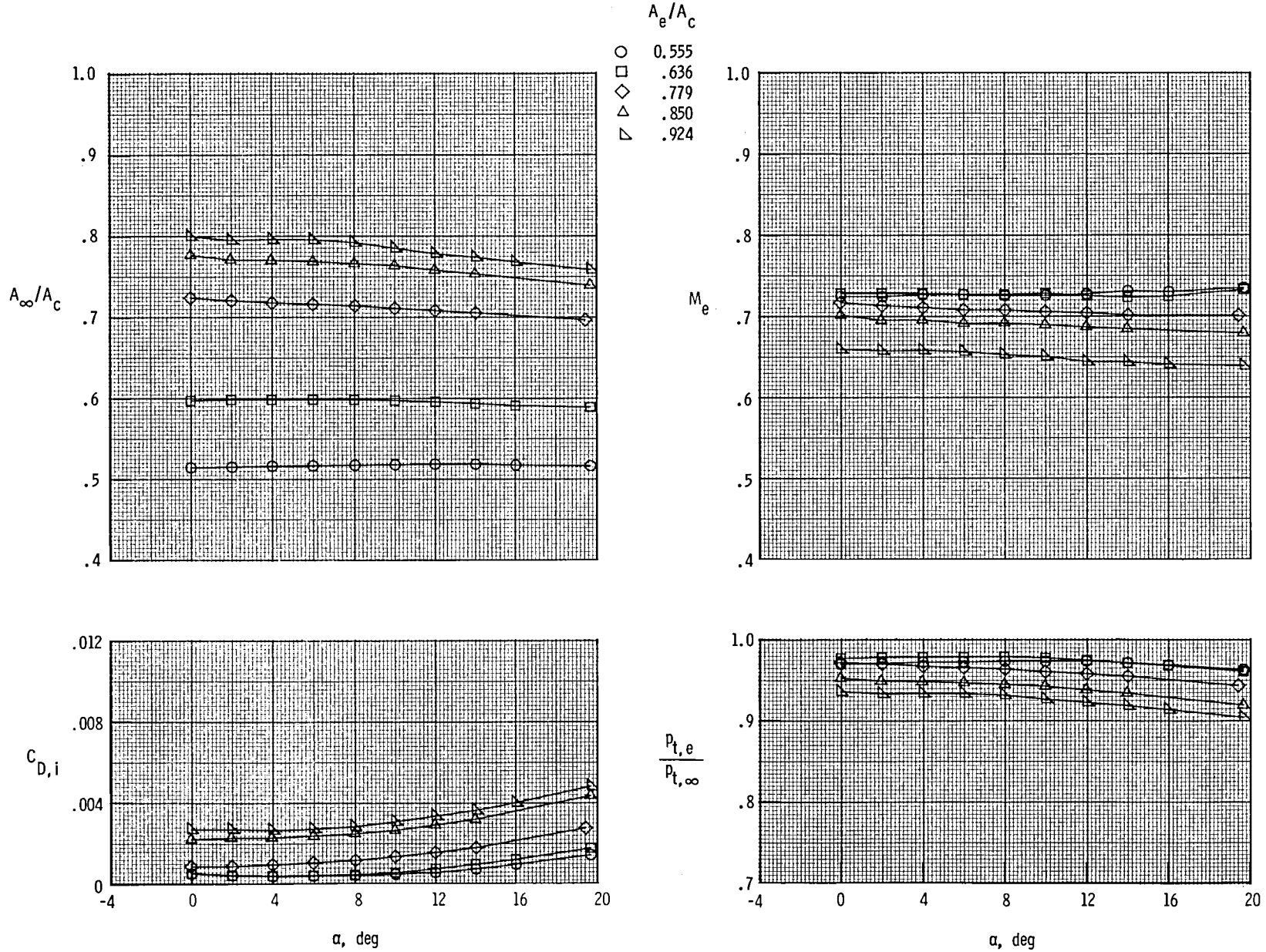

(b) M = 0.80.

Figure 26.- Continued.

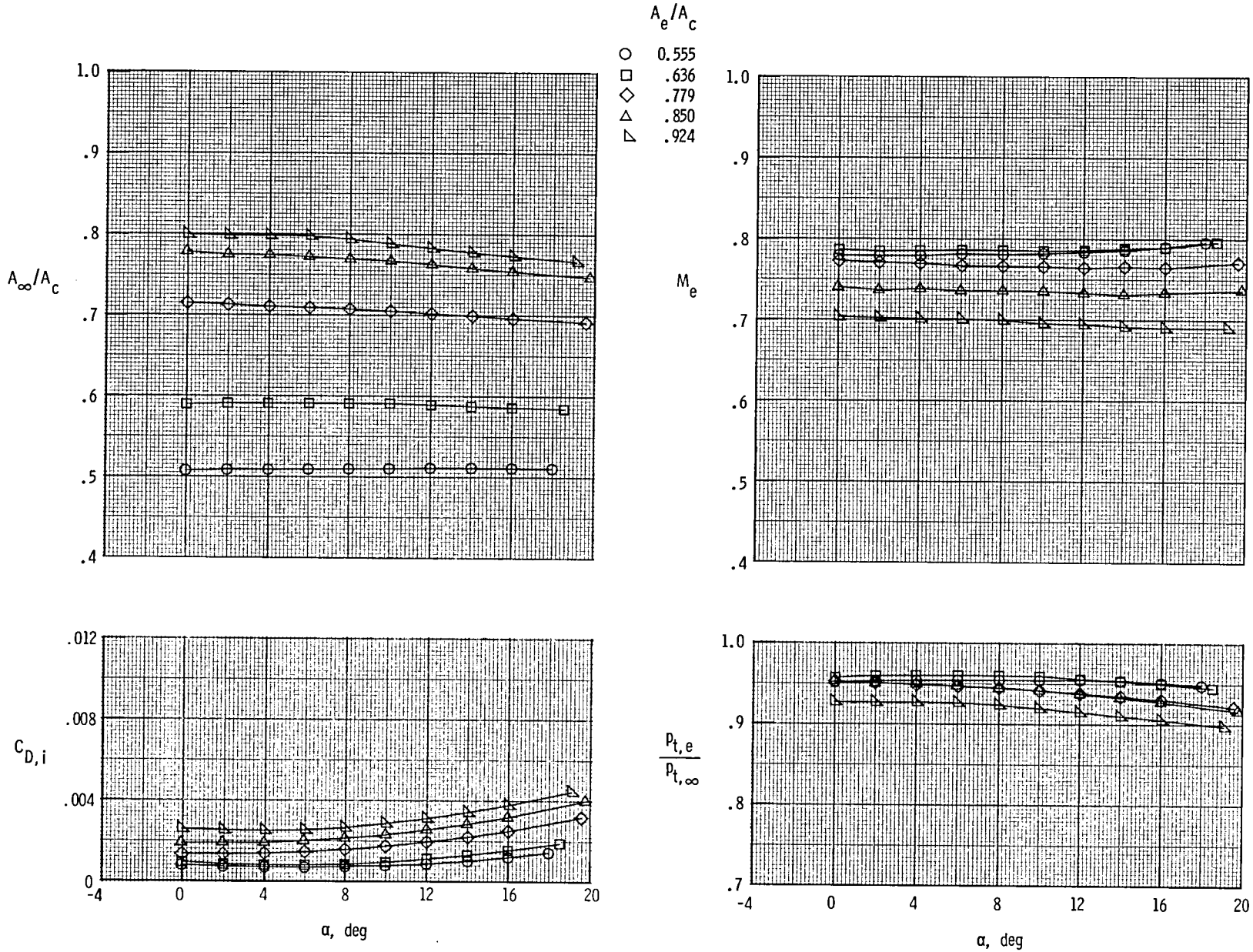

(c) M = 0.87.

Figure 26.- Continued.

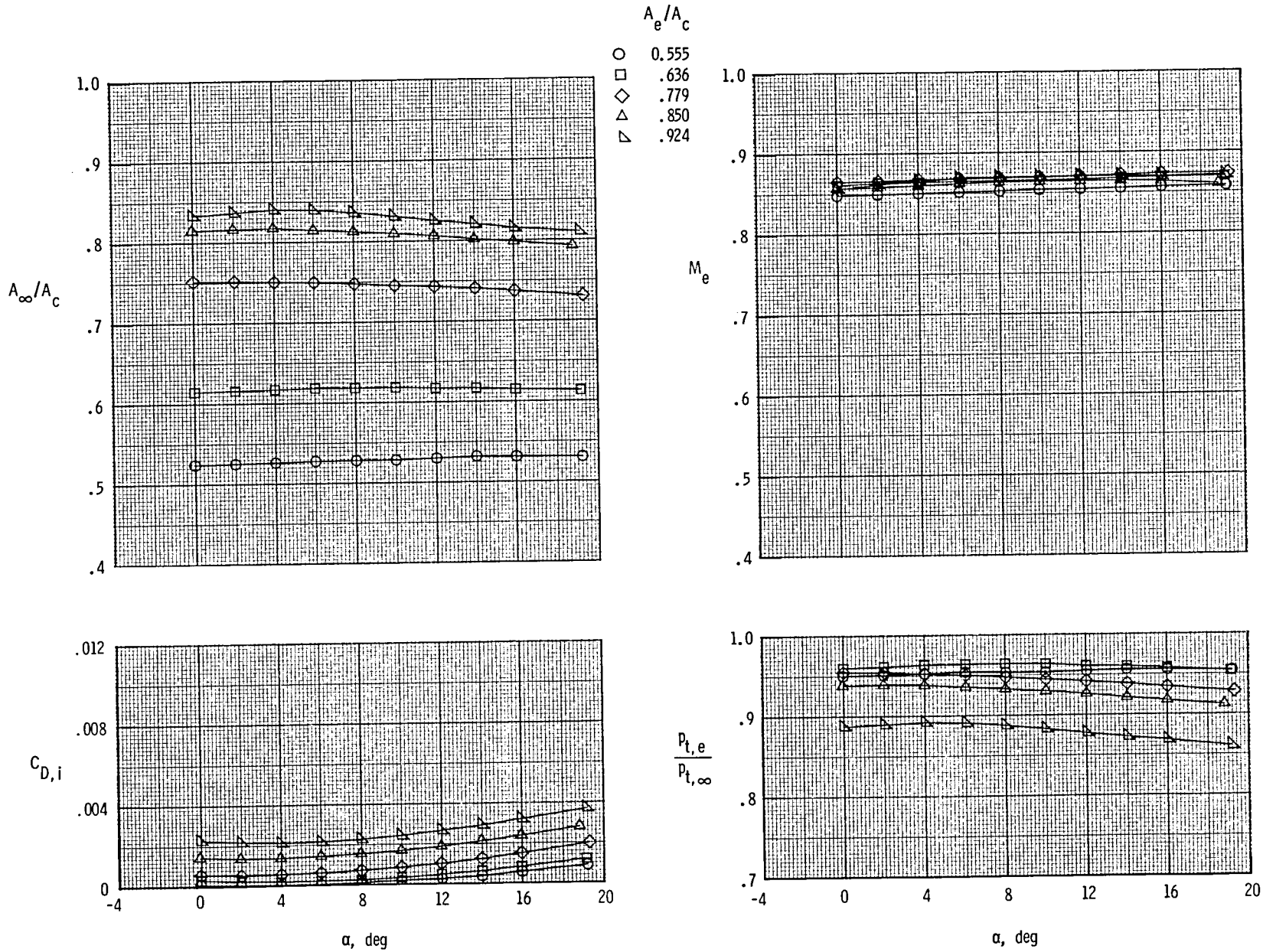

(d) M = 1.20.

Figure 26.- Concluded.

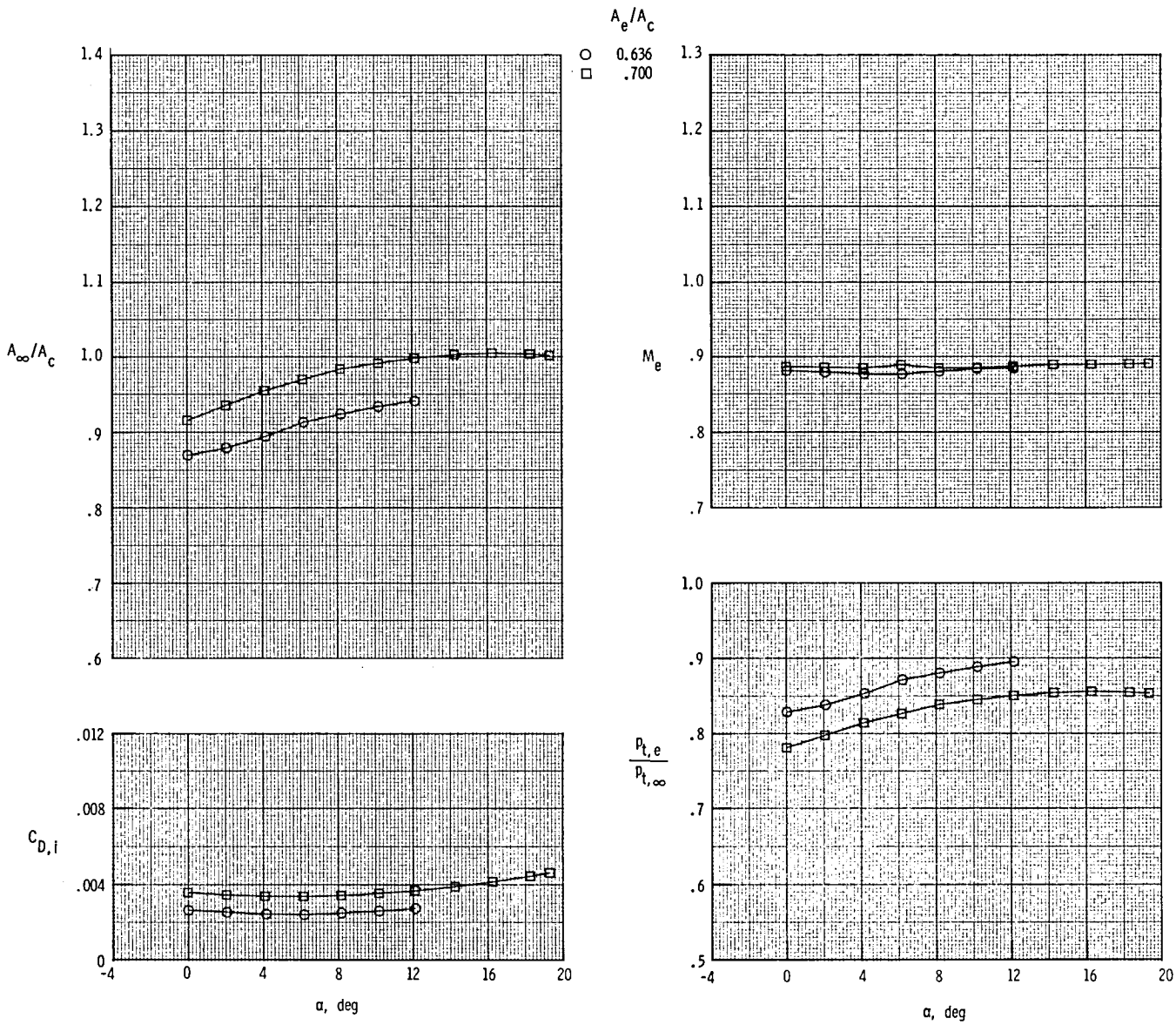

(a) M = 2.00.

Figure 27.- Flow-through nacelle internal flow characteristics for inlet spike designed for M_{in} = 1.75.

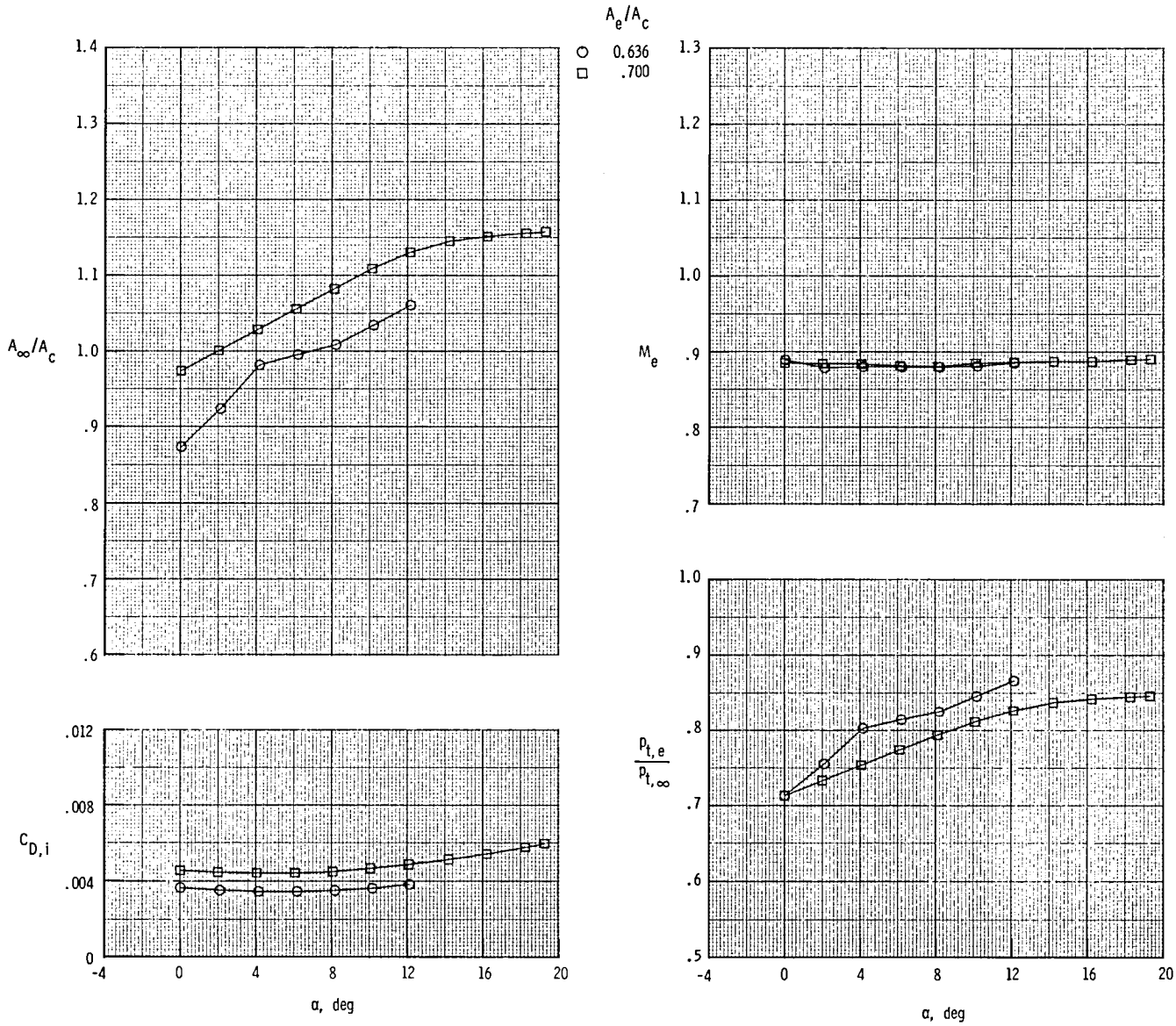

(b) M = 2.17.

Figure 27.- Continued.

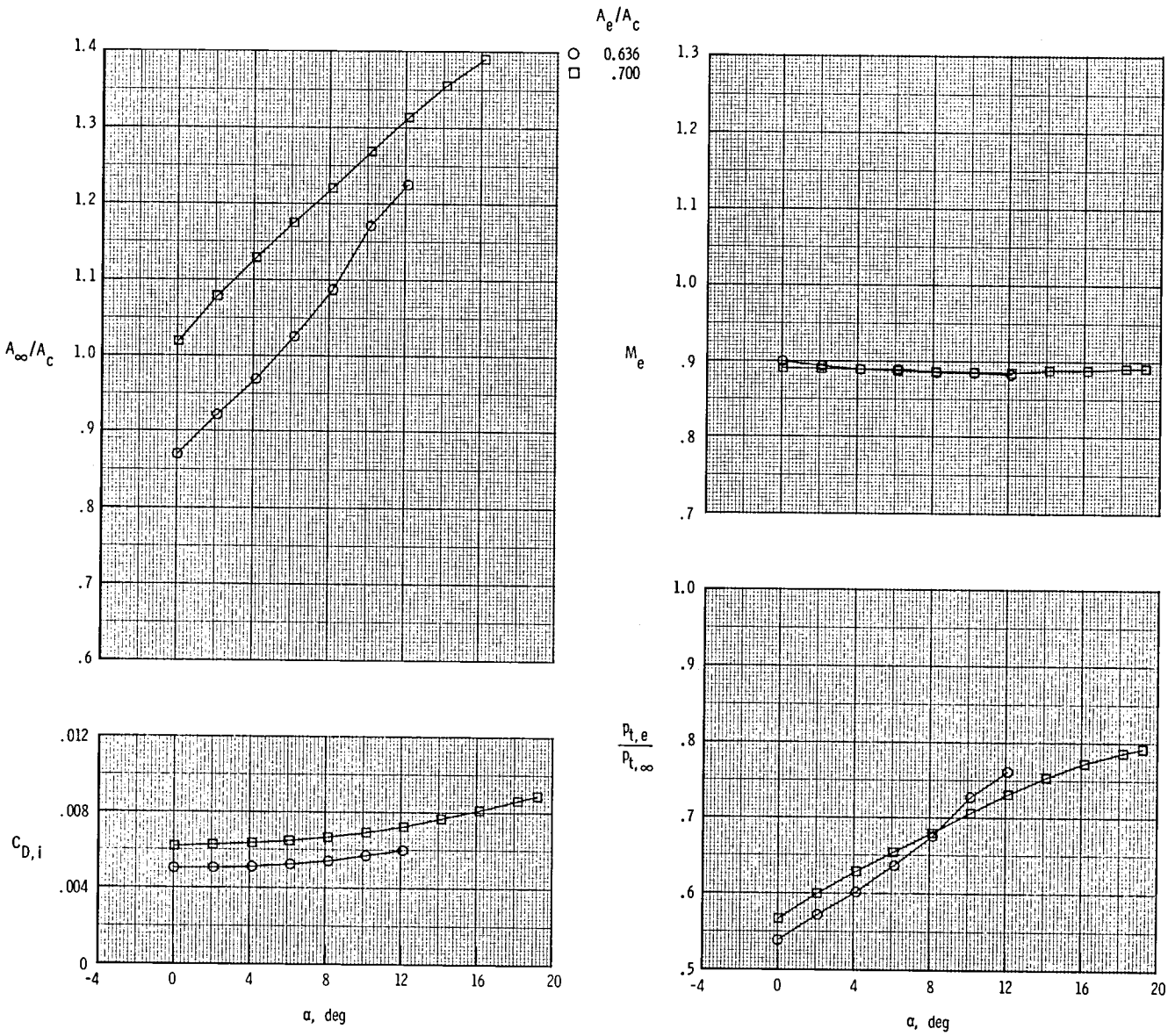

(c) M = 2.47.

Figure 27.- Concluded.

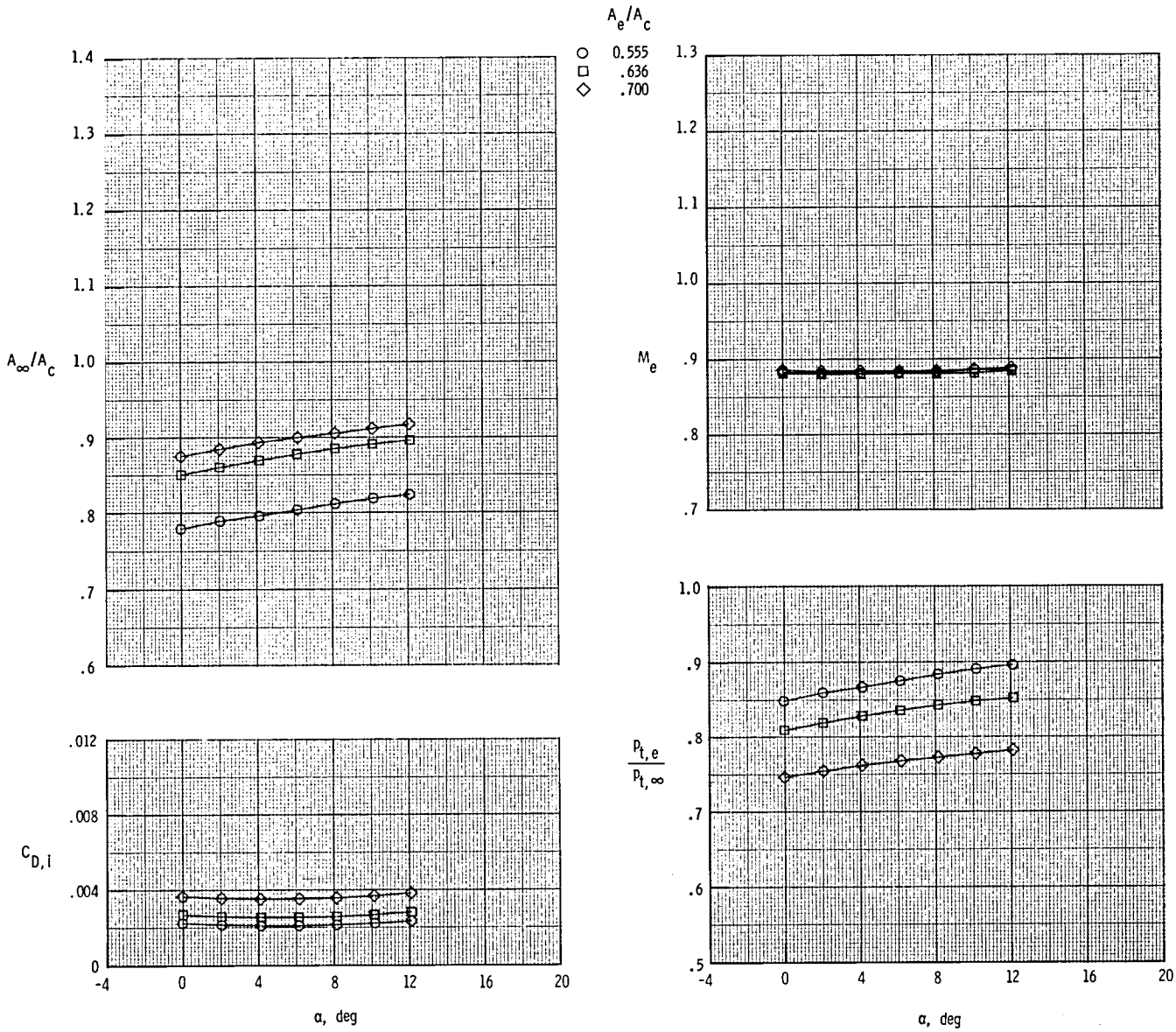

(a) M = 2.00.

Figure 28.- Flow-through nacelle internal flow characteristics for inlet spike designed for M_{in} = 2.00.

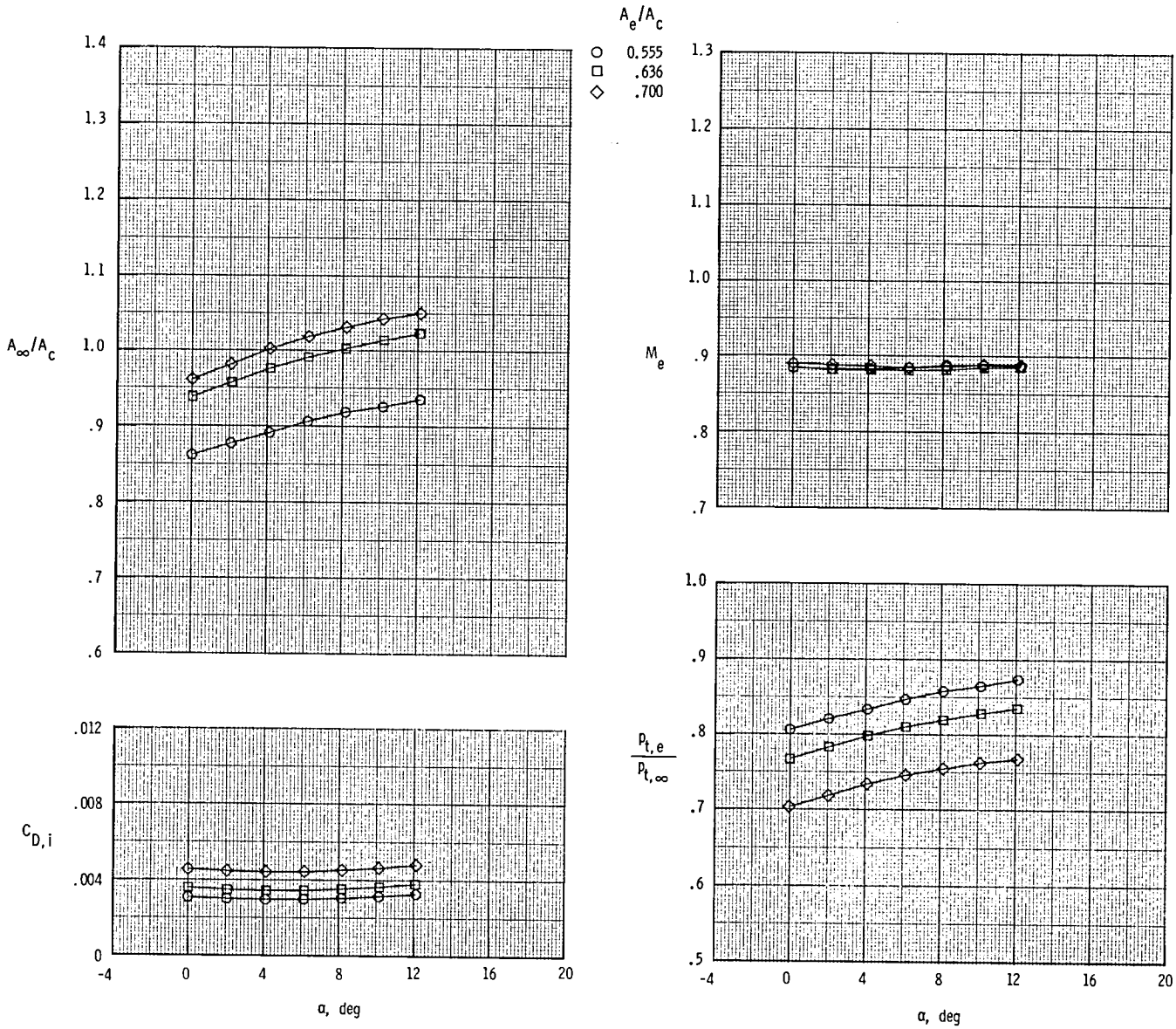

(b) M = 2.17.

Figure 28.- Continued.

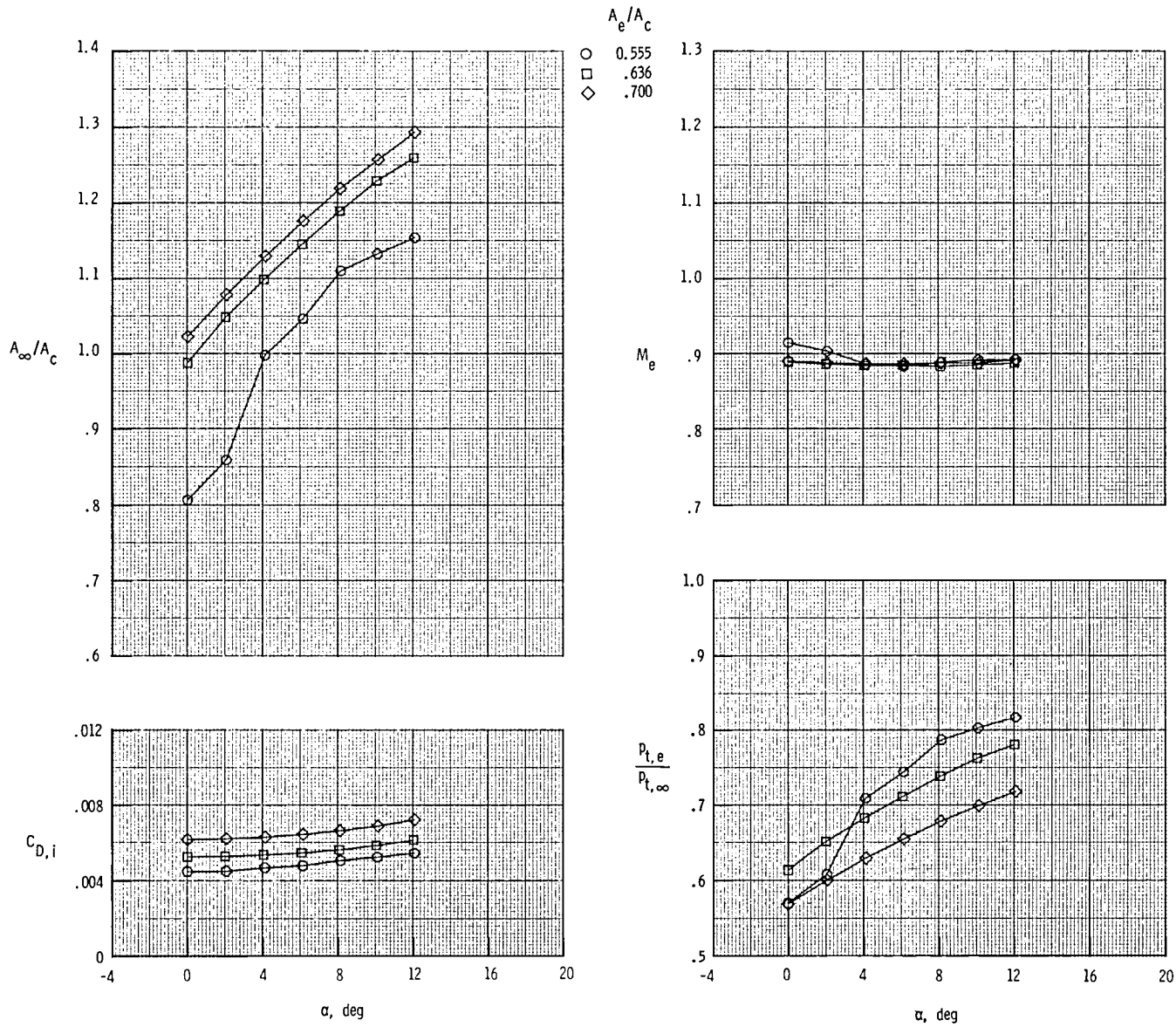

(c) M = 2.47.

Figure 28.- Concluded.

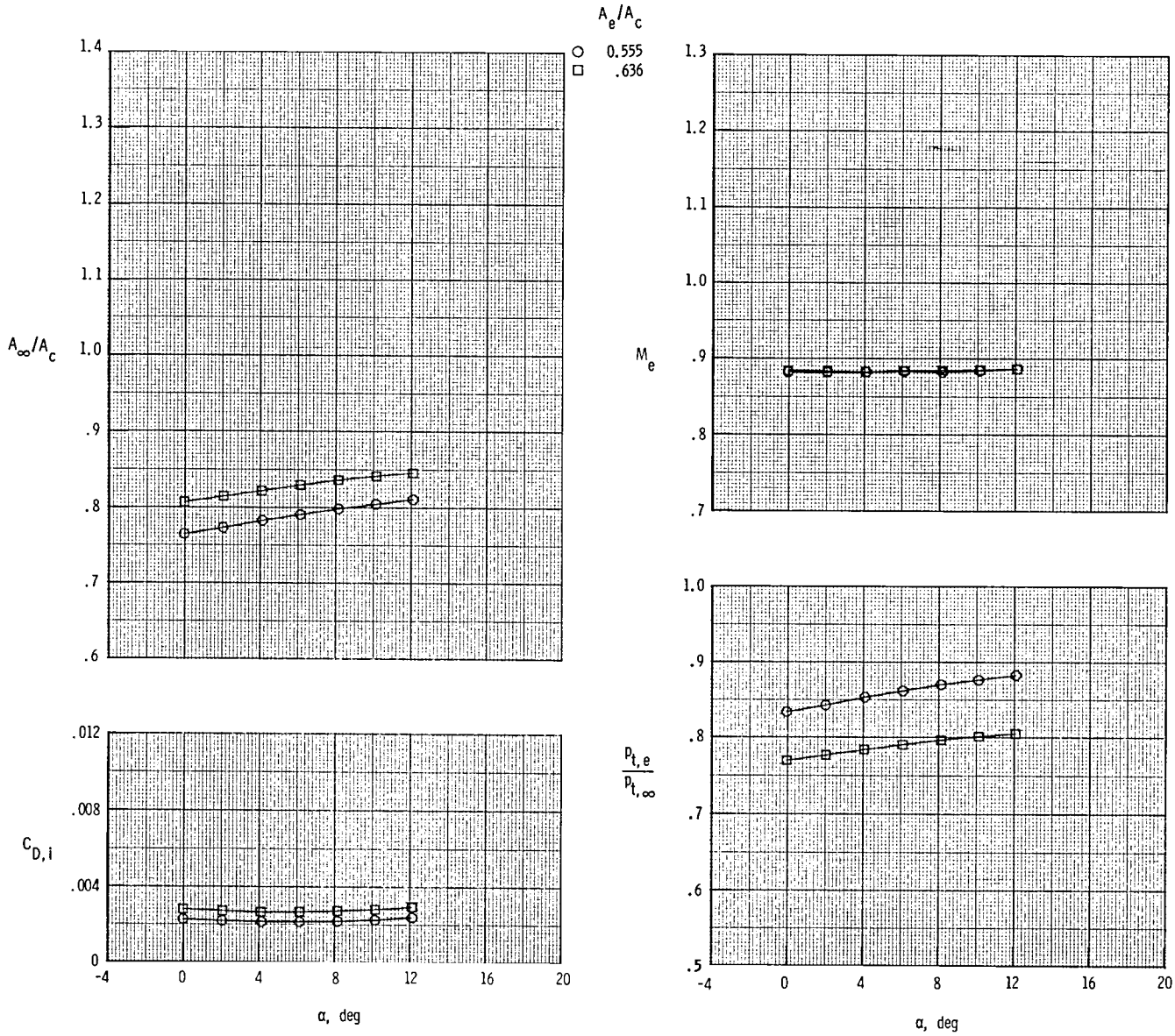

(a) M = 2.00.

Figure 29.- Flow-through nacelle internal flow characteristics for inlet spike designed for M_{in} = 2.20.

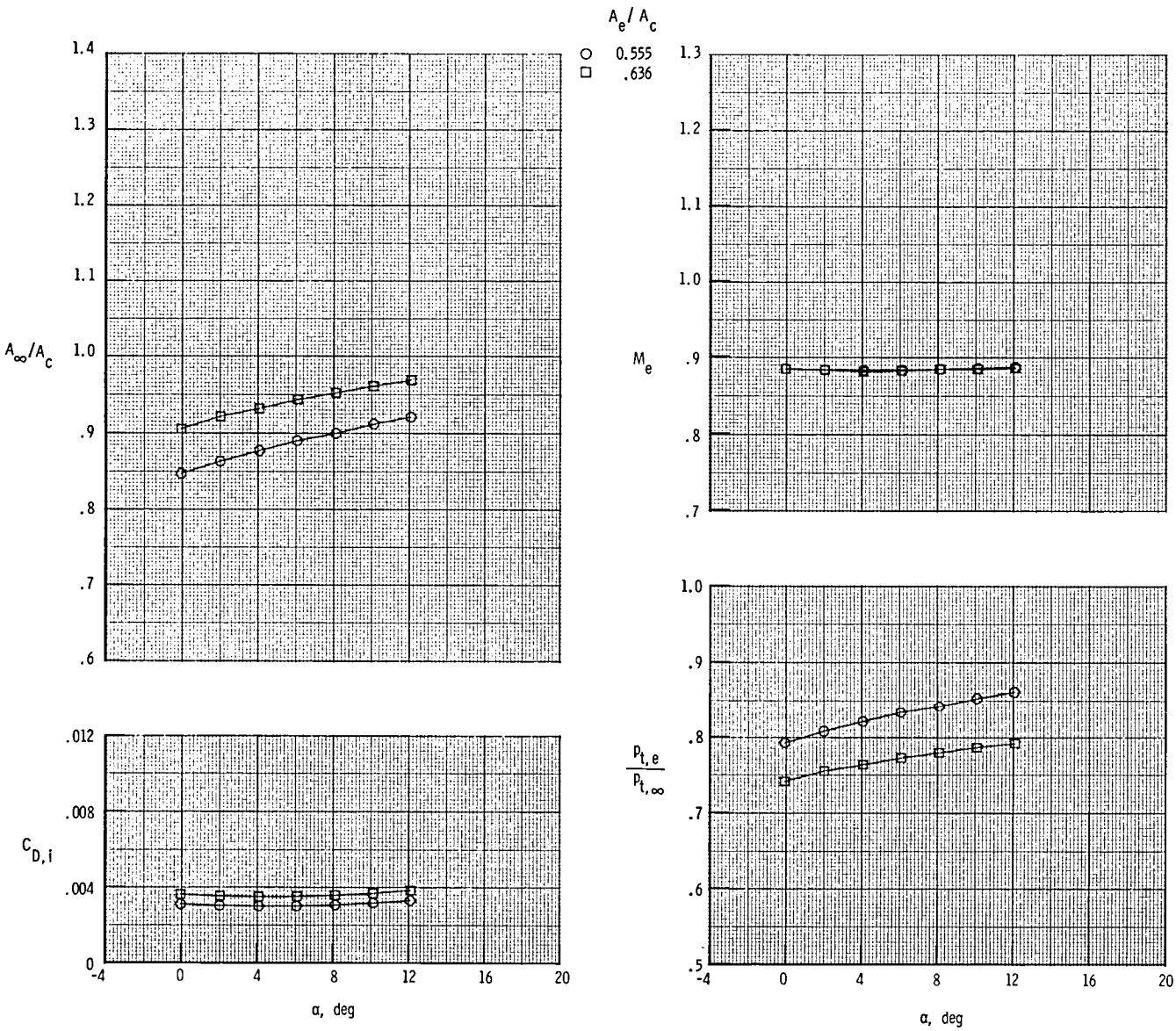

(b) M = 2.17.

Figure 29.- Continued.

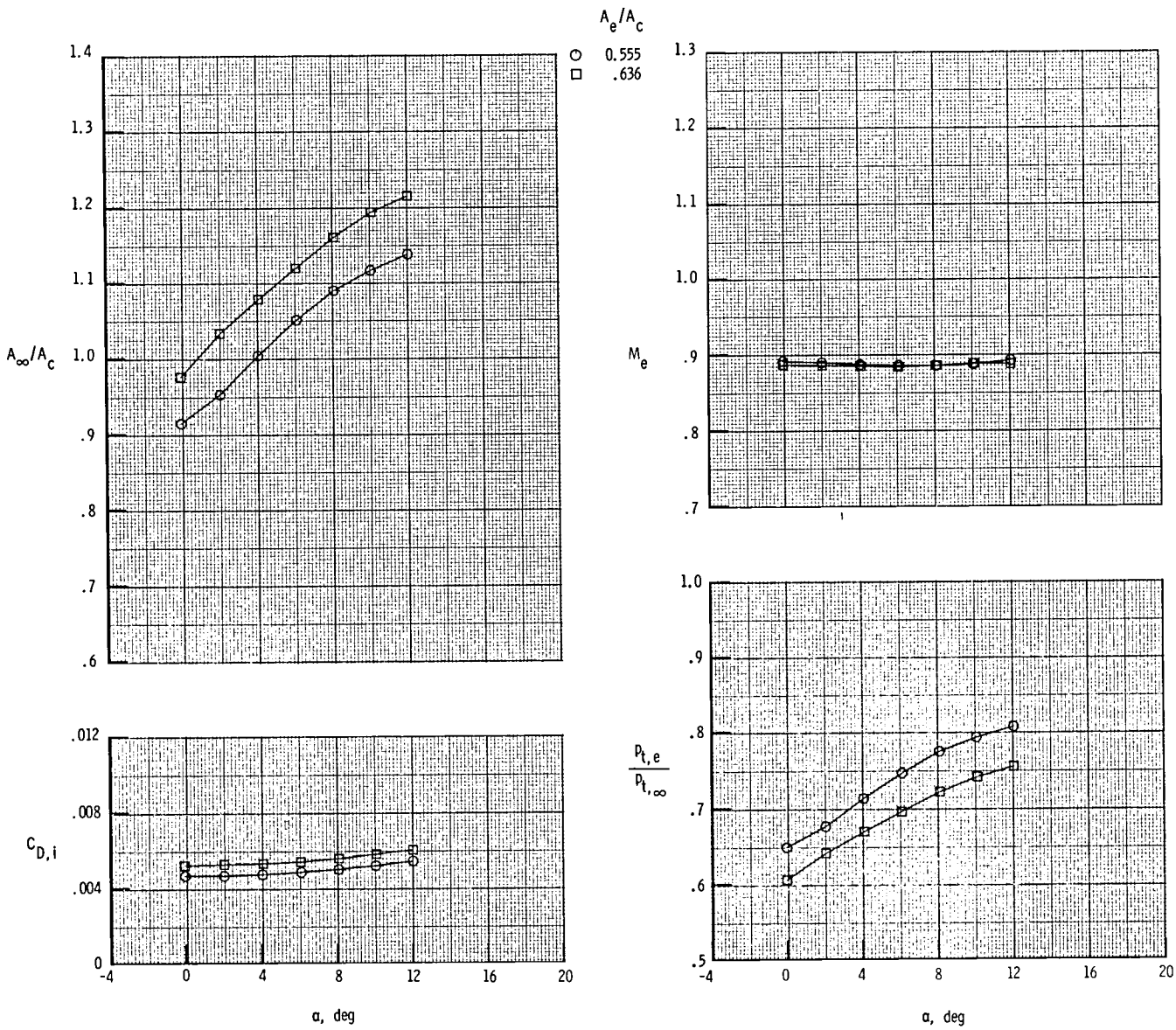

(c) M = 2.47.

Figure 29.- Concluded.

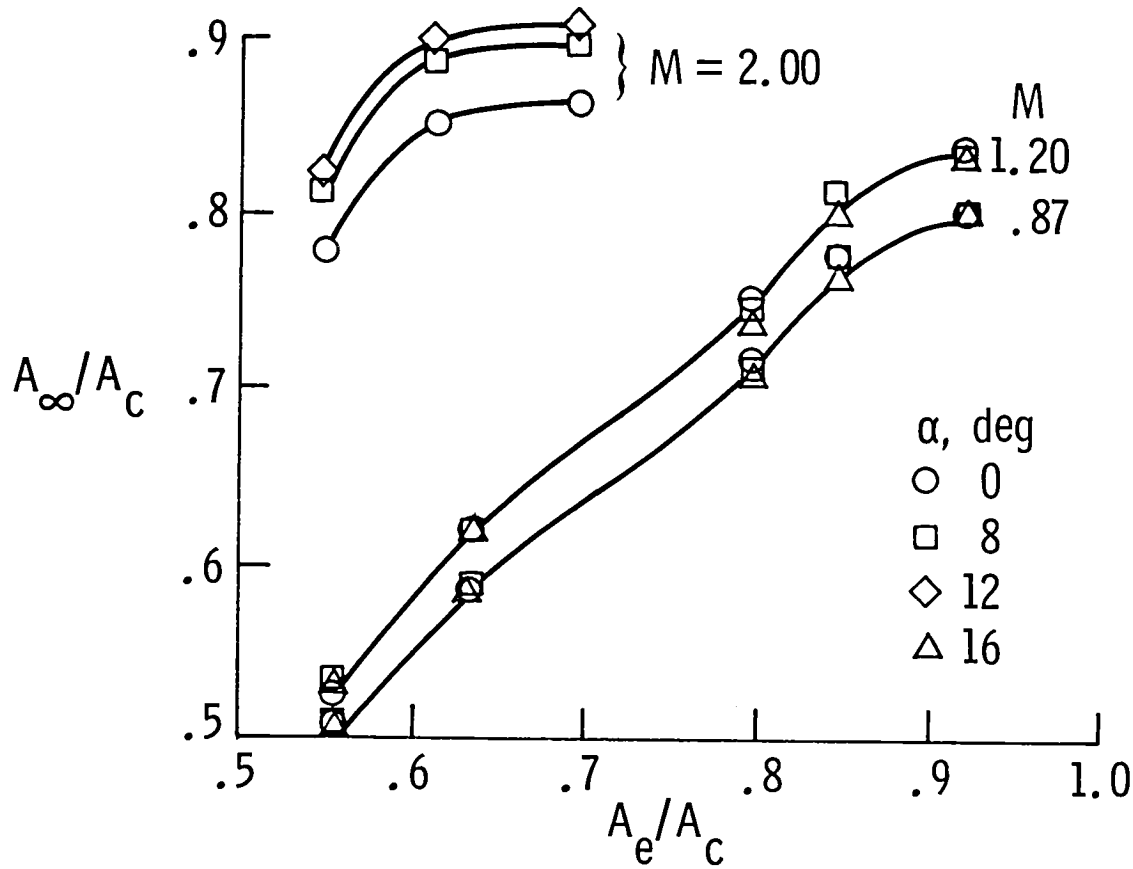

Figure 30.- Typical inlet capture ratio characteristics.

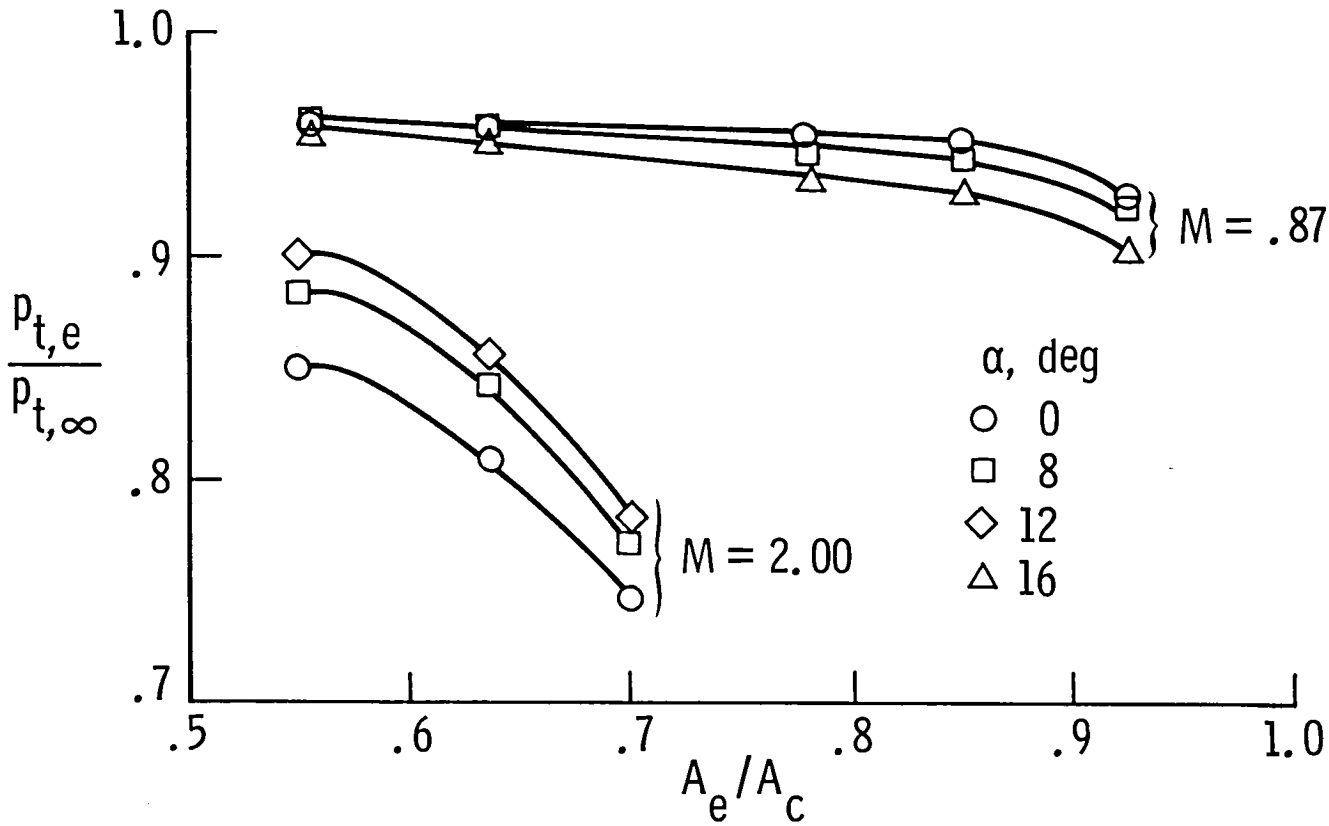

Figure 31.- Typical inlet total-pressure recovery characteristics.

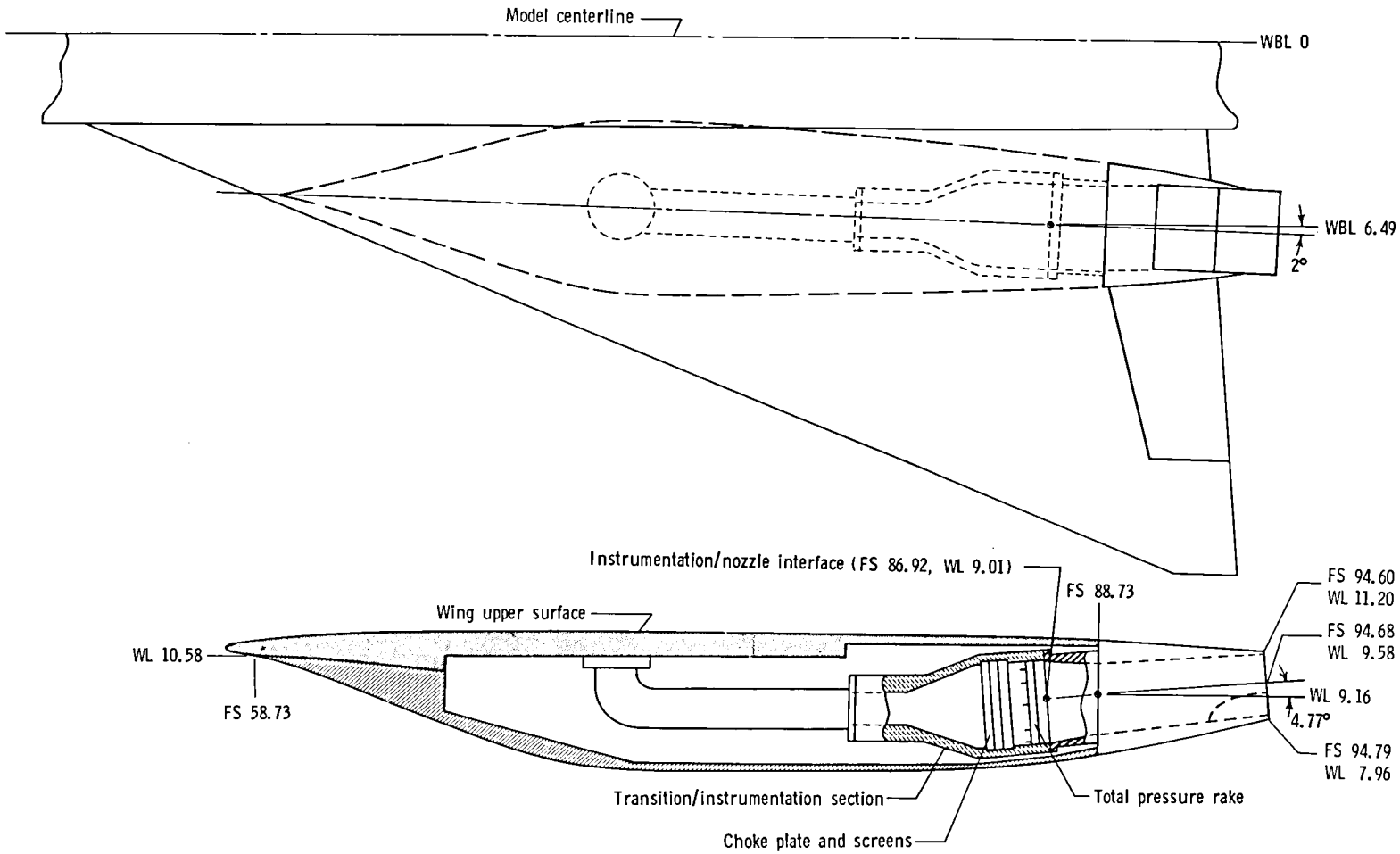

Note: Centerline of instrumentation section 4.17° with respect to water line plane

Figure 32.- Nacelle/nozzle installation. Faired inlet; reference nozzle; A_e/A_c = 0.636; all linear dimensions in inches.

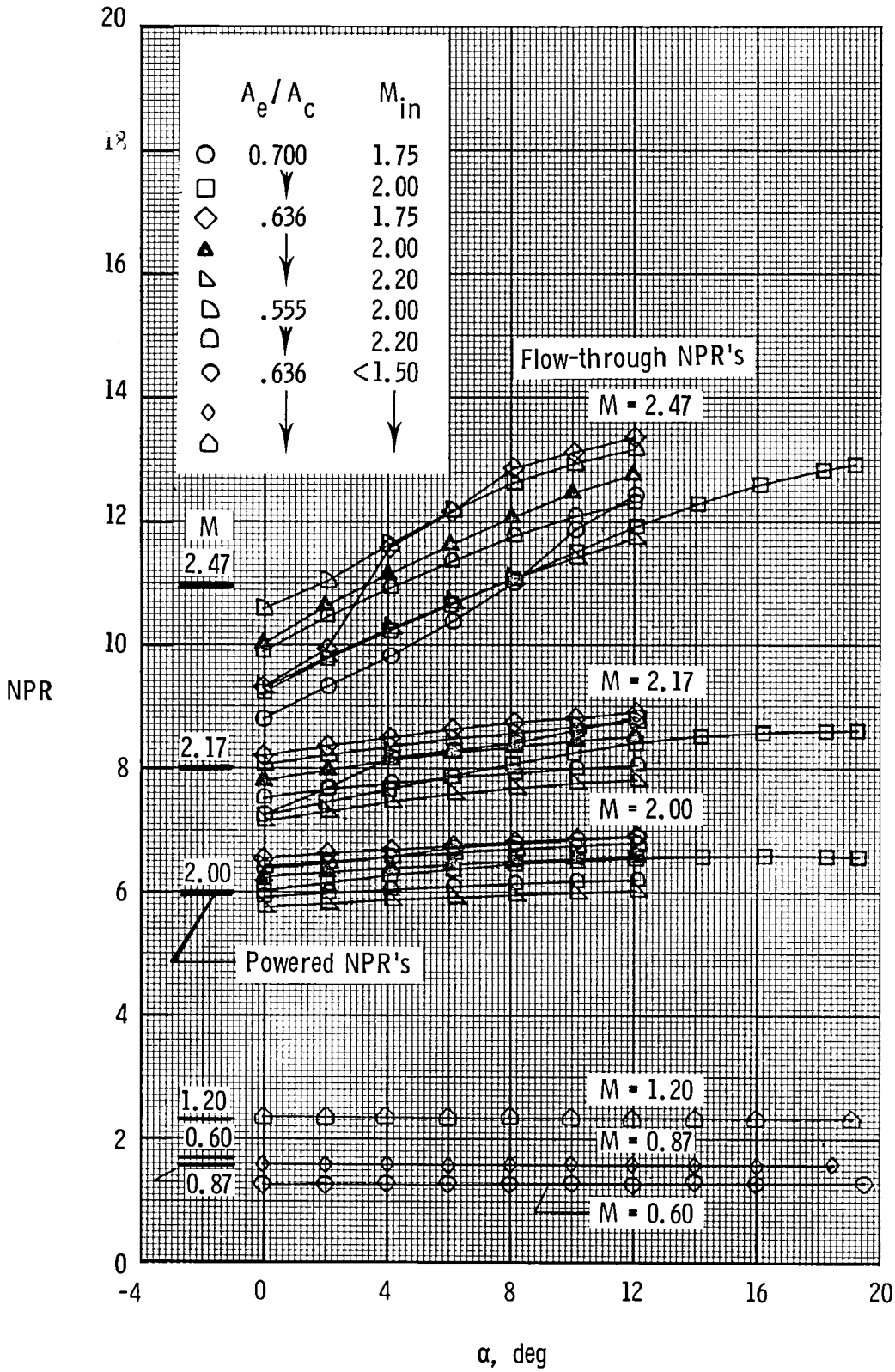

Figure 33.- Comparison between ram (flow-through) and powered nozzle pressure ratio.

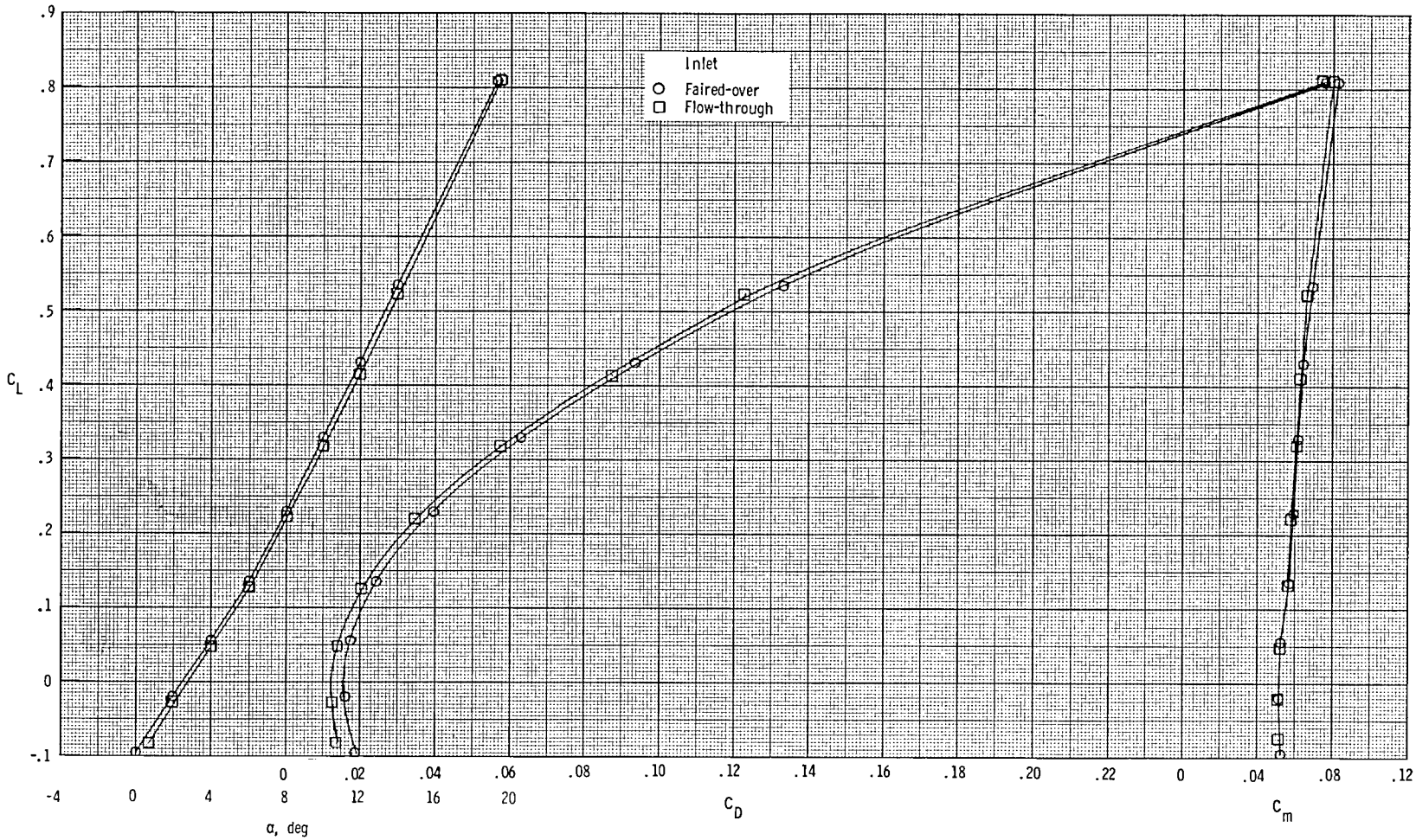

(a) M = 0.60.

Figure 34.- Effect of faired-over inlet on longitudinal aerodynamic characteristics.

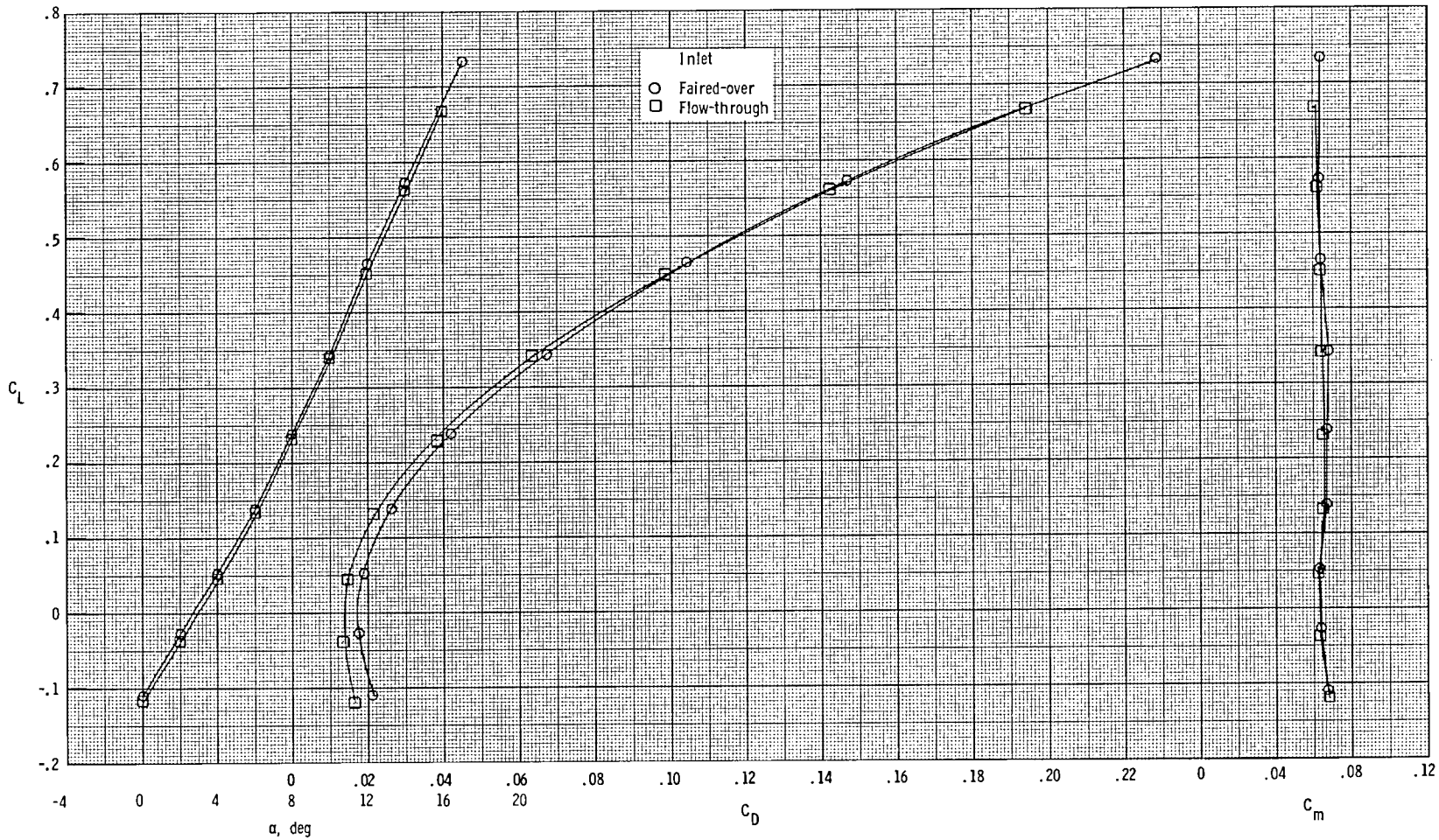

(b) M = 0.87.

Figure 34.- Continued.

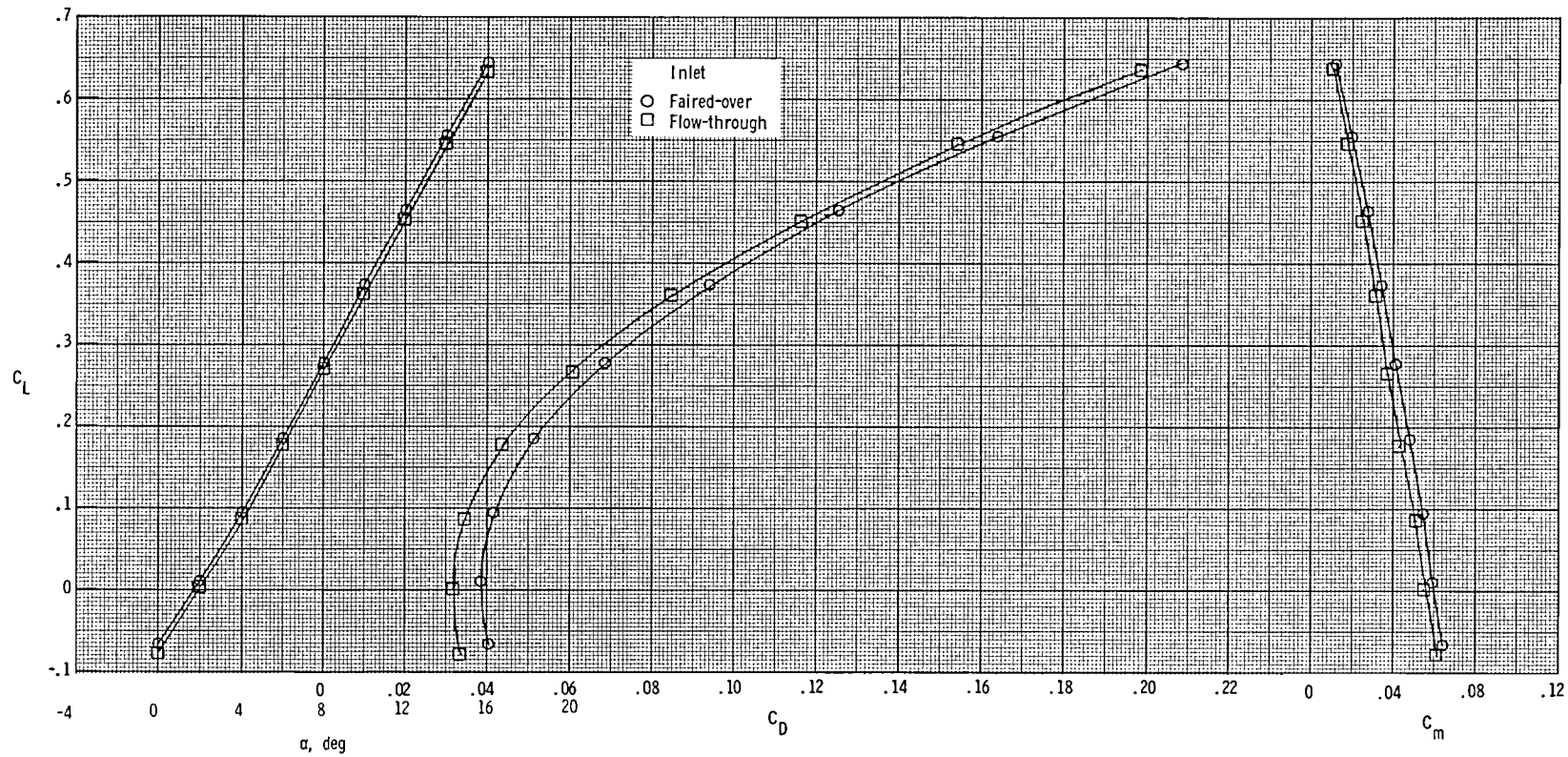

(c) M = 1.20.

Figure 34.- Continued.

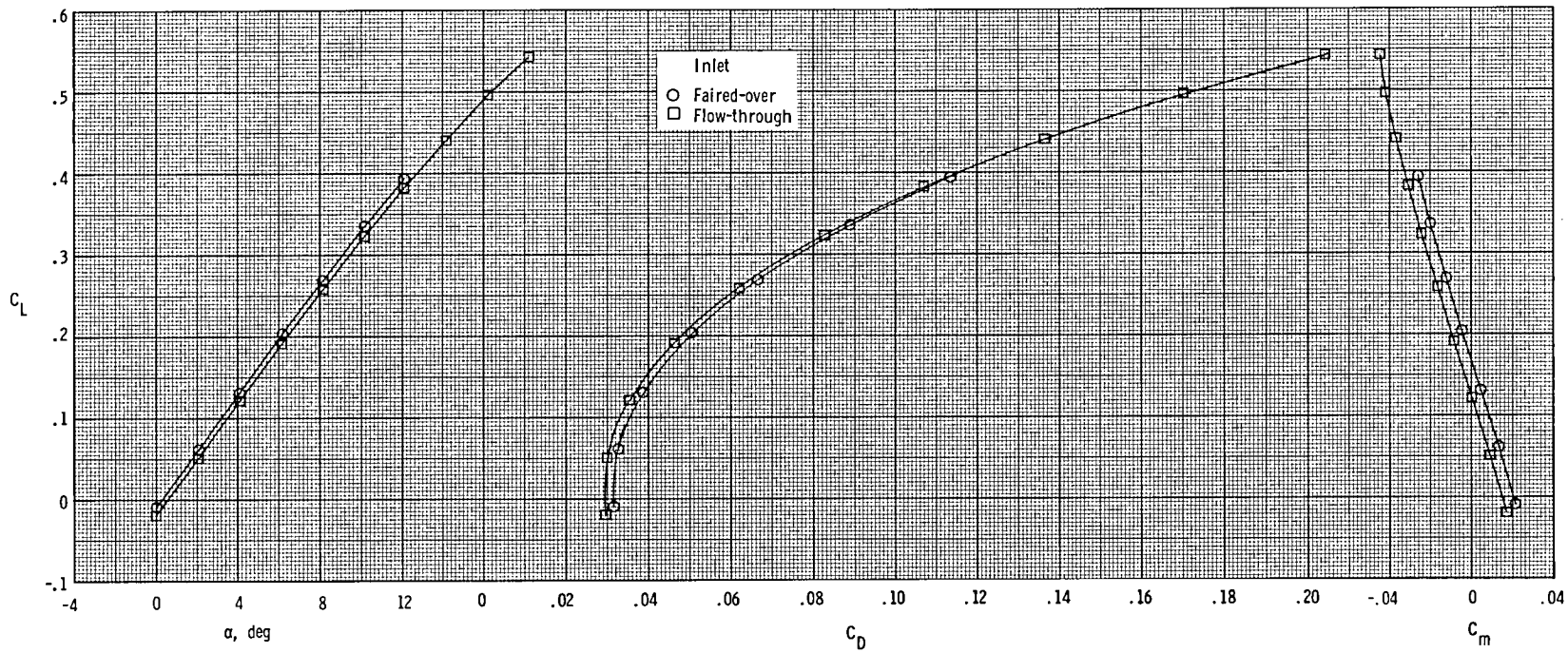

(d) M = 2.00.

Figure 34.- Continued.

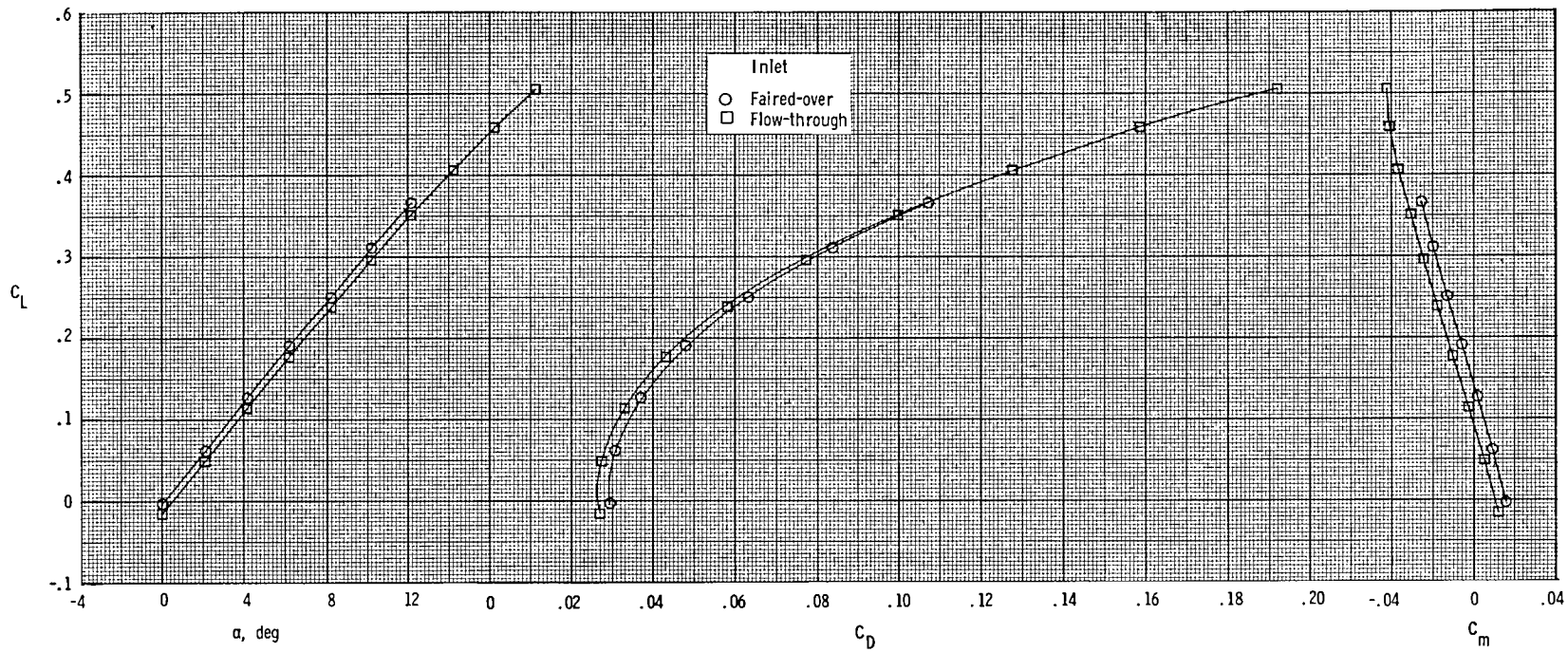

(e) M = 2.17.

Figure 34.- Continued.

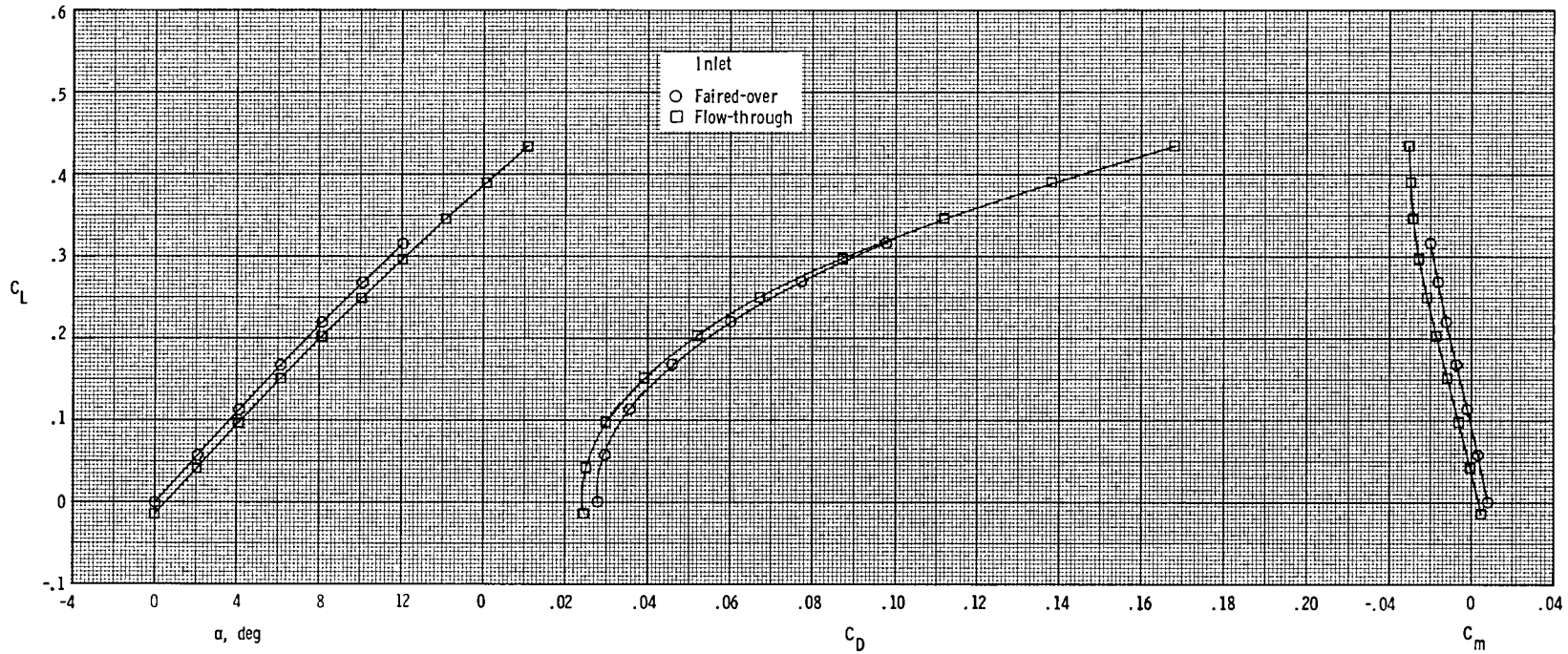

(f) M = 2.47.

Figure 34.- Concluded.

$\Delta C = (C)_{\text{faired inlet}} - (C)_{\text{flow-through inlet}}$

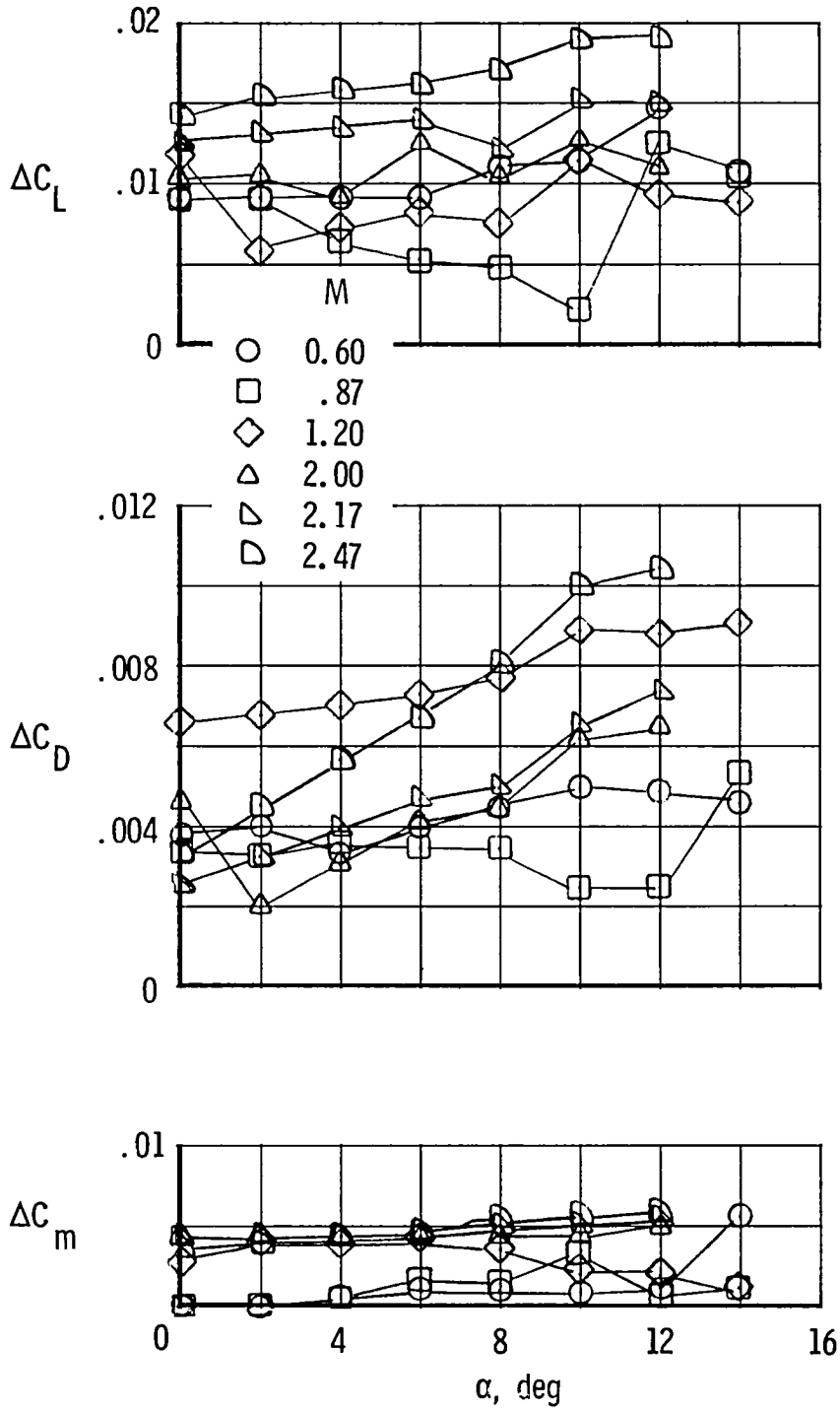

Figure 35.- Effect of faired inlet on incremental aerodynamic characteristics.

1. Report No.	2. Government Accession No.	3. Recipient's Catalog No.
NASA TP-2580		

4. Title and Subtitle	5. Report Date
Aerodynamic Characteristics of a Supersonic Fighter Aircraft Model at Mach 0.40 to 2.47	April 1986
	6. Performing Organization Code 505-43-90-07
7. Author(s)	8. Performing Organization Report No.
Francis J. Capone, E. Ann Bare, and Dorothy Arbiter	L-16017
	10. Work Unit No.
9. Performing Organization Name and Address	
NASA Langley Research Center Hampton, VA 23665-5225	11. Contract or Grant No.
	13. Type of Report and Period Covered
12. Sponsoring Agency Name and Address	Technical Paper
National Aeronautics and Space Administration Washington, DC 20546-0001	14. Sponsoring Agency Code

15. Supplementary Notes

Francis J. Capone and E. Ann Bare: Langley Research Center, Hampton, Virginia.
Dorothy Arbiter: The George Washington University, Joint Institute for Advancement of Flight Sciences, Langley Research Center, Hampton, Virginia.

16. Abstract

The aerodynamic characteristics of an advanced twin-engine fighter aircraft designed for supersonic cruise have been studied in the Langley 16-Foot Transonic Tunnel and the Lewis 10- by 10-Foot Supersonic Tunnel. The objective of this investigation was to establish an aerodynamic data base for the configuration with flow-through nacelles and representative inlets. The use of a canard for trim and the effects of fairing over the inlets were assessed. Comparisons between experimental and theoretical results were also made. The theoretical results were determined by using a potential vortex lift code for subsonic speeds and a linear aerodynamic code for supersonic speeds. This investigation was conducted at Mach numbers from 0.40 to 2.47, at angles of attack from 0° to about 20°, and at inlet capture ratios of about 0.5 to 1.4.

17. Key Words (Suggested by Author(s))	18. Distribution Statement
Fighter aircraft Supersonic cruise Canard Linear theory	Unclassified - Unlimited Subject Category 02

19. Security Classif. (of this report)	20. Security Classif. (of this page)	21. No. of Pages	22. Price
Unclassified	Unclassified	103	A06

For sale by the National Technical Information Service, Springfield, Virginia 22161